Master Thesis

Investigation of high-frequency pressure fluctuations in water and liquid nitrogen during pressure surges with cavitation

Timo Gonschior
Matriculation number 369696

German Aerospace Center (DLR)[1]
Institute of Space Propulsion
Department of Rocket Propulsion Systems

Technische Universität Berlin[2]
Institute of Fluid Mechanics and Technical Acoustics
Chair of Fluid System Dynamics

Examiner: Prof. Dr.-Ing. Paul Uwe Thamsen[2]
Supervisor: Sebastian Klein, M. Sc.[1]
Supervisor: Dr.-Ing. Julija Peter[2]

Lampoldshausen 2022

Eidesstattliche Erklärung

Hiermit erkläre ich, dass ich die vorliegende Arbeit selbstständig und eigenhändig sowie ohne unerlaubte fremde Hilfe und ausschließlich unter Verwendung der aufgeführten Quellen und Hilfsmittel angefertigt habe.

Berlin, den 06.02.2023

.....

Timo Gonschior

Zusammenfassung

Druckstöße sind ein verbreitetes Phänomen in strömungstechnischen Systemen. Sie können zum Beispiel durch das plötzliche Abbremsen einer Flüssigkeit beim schnellen Schließen eines Ventils hervorgerufen werden und können zu potentiell zerstörerisch hohen Drücken führen. In der Folge kann die Verdünnungswelle niedrige Drücke hervorrufen, was dazu führen kann, dass die Flüssigkeit kavitiert. Diese Kavitation hat einen großen Einfluss auf das Verhalten der Druckschwingungen.

Druckstöße in Wasser wurden in der Vergangenheit ausführlich untersucht. Im Vergleich dazu gibt es wenig Forschung mit kryogenen Medien als Testflüssigkeit. Kryogene Medien sind allerdings besonders relevant im Bereich der Raumfahrtantriebe. Um die Übertragbarkeit der Erkenntnisse von Wasser auf kryogene Medien bewerten zu können, müssen die Unterschiede im Kavitationsverhalten zwischen diesen Medien und die daraus resultierenden Auswirkungen auf das Druckstoß-Verhalten bekannt sein. Dazu trägt die vorliegende Arbeit bei, indem sie bestimmte Aspekte der hochfrequenten Druckschwankungen während der Kavitation und deren Unterschiede zwischen Wasser und flüssigem Stickstoff untersucht.

Die Messdaten wurden anhand charakteristischer Merkmale in den Drucksignalen geclustert, um eine aussagekräftigere statistische Auswertung zu ermöglichen. Das Verhalten der Intensität des Rauschens über die Zeit wurde innerhalb mehrerer aufeinanderfolgender Kavitationstäler ausgewertet. Es hat sich gezeigt, dass sich das Rauschen in dem Bereich des Rohres, in dem Kavitation vorliegt, in Wasser unabhängig von dem Rauschen in der Flüssigkeitssäule verhält, während in flüssigem Stickstoff eine starke Kopplung ersichtlich war.

In Wasser wurde die Ausbreitung von Druckpeaks untersucht, mit dem Ziel, Aussagen über den Ursprung dieser Peaks zu treffen. Diese Untersuchung ergab, dass eine auffällig große Zahl an Peaks aus einem Bereich nahe des Ventils stammt. Es wurde daher angenommen, dass diese Peaks vom Kollaps von Kavitationsblasen stammen.

In flüssigem Stickstoff wurde ein charakteristischer Peak auf dessen zeitliches Auftreten und seine Breite hin untersucht. Die Ergebnisse legen eine Übereinstimmung mit der Druckwelle nahe, die laut der Theorie zu erwarten ist. Die Abweichungen von der Theorie könnten zu einer verringerten Schallgeschwindigkeit auf Grund der Kavitation und einem Abriss der Flüssigkeitssäule am Ventil passen. Einhergehend mit diesen Peaks, wurde ein hochfrequentes Rauschen mit einer diskreten Frequenz von 25 kHz beobachtet. Es wurde eine Methode entwickelt, um die Position der Quelle dieses Rauschens zu ermitteln. Die Ergebnisse zeigen einen Zusammenhang zwischen Ort der Quelle und der Zugspannung, die auf Grund der Verdünnungswelle auf die Flüssigkeit wirkt. Demnach geht eine höhere Zugspannung damit einher, dass der Ursprung des Rauschens näher am Tank liegt.

Abstract

Pressure surges are a common phenomenon in fluid dynamic systems. They can, for example, occur when stopping a fluid by closing a valve rapidly and may lead to destructively high pressures. Subsequently, the resulting rarefaction wave can lead to low pressures, potentially causing the liquid to cavitate. The presence of cavitation has a drastic impact on the overall pressure oscillations.

While water as a test fluid has been studied extensively in the past, comparably little attention has been paid to cryogenic media. However, cryogenic media are of particular importance for space propulsion systems. In order to assess the transferability of findings from water to cryogenic media, the differences in the cavitation behavior between those types of fluids and the resulting consequences for the pressure surge behavior need to be known. This thesis contributes to that by investigating certain aspects of the high-frequency pressure fluctuations during cavitation and their differences between water and liquid nitrogen.

The measurements were clustered according to characteristic features of the pressure readings in order to allow for a more informative statistical evaluation. The behavior of the noise intensity over time was evaluated within multiple subsequent cavitation valleys. It was found that in water the noise in the cavitation region of the pipe behaves independently from the noise in the liquid column, while a strong coupling was apparent in liquid nitrogen.

In water the propagation of pressure peaks was investigated in order to draw conclusions on the origin of those peaks. It was found that a dominant number of peaks originated from a region close to the valve. These peaks were therefore attributed to bubble collapse.

In liquid nitrogen a characteristic peak was investigated in terms of timing and duration. The results suggested agreement with the main pressure wave predicted by theory. Deviations from the theory could fit to a reduced speed of sound due to cavitation and a column separation at the valve. High-frequency noise with a discrete frequency of 25 kHz was observed during these peaks. A method for tracking the point of origin of this noise was proposed. The results showed a correlation between the source location and the tension caused by the rarefaction wave. A higher tension goes along with a point of origin closer to the tank.

Table of Contents

List of Figures

List of Tables

Abbreviations

ATV Automated Transfer Vehicle

DGCM Discrete Gas Cavity Model

DLR German Aerospace Center (Deutsches Zentrum für Luft- und Raumfahrt)

DVCM Discrete Vapor Cavity Model

LN_2 Liquid Nitrogen

FFT Fast Fourier Transform

FTTF Fluid Transient Test Facility

H_2O Water

IQR Interquartile Range

RMS Root Mean Square

SoS Sum of Squares

SSE Sum of Squared Error

Symbols

Symbol	Description	Unit
A	amplitude	dB
$A_i, \quad i \in (1,2)$	cluster parameters: area between curves in first or second half of cavitation valley	
a	speed of sound / wave propagation speed	m/s
$\mathcal{C}_{23}$	set of S2-S3-combinations	
C_{123}	combination of S1- and S2- and S3-peak	
C_{23}	combination of S2- and S3-peak	
c_{p_L}	specific heat capacity of the liquid	J/(kg·K)
$\mathcal{D}_{13}$	delay matrix for S1-S3-combinations	
$\mathcal{D}_{23}$	delay matrix for S2-S3-combinations	
D	inner pipe diameter	m
d	difference between fit and sample (section 4.2.1)	
d	difference between peak and moving standard deviation (section 5.2.1)	bar
d_0	parameter of logistic error function	
d_i	inner pipe diameter (chapter 3 ff.)	m
d_{max}	reference difference between peak and moving standard deviation for uniqueness scaling function	bar

Symbol	Description	Unit
d_r, d_f	deviation of edge detection between two different thresholds	
d_s	distance between two peaks in samples	
E	Youngs's modulus	N/m^2
e	wall thickness	m
e	error: result of logistic error function (section 4.2.1)	
e	envelope of moving RMS (section 5.2.2)	bar
f	Darcy-Weißbach friction factor	
f_s	sampling frequency	Hz
f_{io}	frequency of initial oscillation	Hz
g	gravitational acceleration	m/s^2
g_{var}	gradient of cluster parameter with respect to k and d_0	m/s^2
H	hydraulic head	m
h	counter index for S2-S3-combinations (section 5.2.1)	
i	counter index for peaks in S1 (section 5.2.1)	
i_r, i_f	sample of rising / falling edge (LN_2-peak)	
J	nucleation rate	1/s
j	counter index for peaks in S2 (section 5.2.1)	
K	bulk modulus of elasticity	N/m^2
k	parameter of logistic error function (section 4.2.1)	
k	number of clusters (section 4.2.2)	
k	counter index for peaks in S3 (section 5.2.1)	
k_B	Boltzmann constant	$m^2 \cdot kg \cdot s^{-2} \cdot K^{-1}$
k_p	polytropic exponent	
L	pipe length (chapter 2.1)	m
L_{vap}	latent heat of evaporation (chapter 2.2)	J
l	pipe length (chapter 3 ff.)	m
l_1, l_2, l_3	distance between noise source and sensors	m
l_{io}	length of initial oscillation in samples	
l_v	cluster parameter: valley length	
N, N', N_{avg}, N_σ	window size / filter width in samples	
N_{S1}	range around S1-peaks during peak detection	
n, n', n_A	number of samples	
P_{ref}	reference for conversion in decibels	
P^2	FFT output	
p_0	initial pressure	bar
$p_{0_{hp}}$	initial pressure in high pressure tank	bar
$p_{0_{lp}}$	initial pressure in low pressure tank	bar
p_1	pressure at first maximum of pressure oscillation	bar
p_a	ambient pressure	bar
p_{avg}	moving average of pressure reading	bar
p_B	pressure inside bubble	bar
p_{G_0}	partial pressure of contaminant gas	bar
p_{hp}	pressure in high pressure tank	bar
p_P	pulse pressure after bubble collapse	bar
p_{ref}	reference pressure of cavitation valley	bar
p_{S1}	pressure at position S1 (from dynamic pressure sensor)	bar
p_t	tank pressure	bar
p_v	vapor pressure	bar
p_∞	pressure infinitely far away from bubble	bar
$\tilde{p}$	normalized pressure	
$\tilde{p}_{th}$	threshold pressure for peak detection in LN_2	
$\hat{p}$	RMS of pressure	bar
$\hat{p}'$	RMS of pressure shifted by calculated delay	bar

Symbol	Description	Unit
R	bubble radius	m
R_C	critical bubble radius	m
R_E	bubble radius at equilibrium	m
r	radial distance	m
S	surface tension	N/m
s	cluster parameter: spread (chapter 4)	
s	scaling of envelope (chapter 5.2)	
s_c	silhouette coefficient	
T	temperature	K
T_B	temperature inside bubble	K
T_c	life time of first cavity	s
T_∞	temperature infinitely far away from bubble	K
t	time / timestamp	s
t_{c1}	critical time bubble growth	s
t_{c4}	critical time bubble collapse	s
t_{exp}	expected time	
t_{no}	cluster parameter: relative time of noise onset	
t'_{no}	absolute time of noise onset	s
t_{ref}	reference time according to equation (4.1)	s
t_s	timestamp of sample	s
t_{TC}	bubble collapse time	s
t_v	valve closure time	s
u	uniqueness	
V_v	vapor volume	m^3
V_m	mixture volume	m^3
v	flow velocity	m/s
v_0	initial flow velocity	m/s
v_1	flow velocity after reflection of rarefaction wave at the valve	m/s
var	placeholder for any cluster parameter	
$\mathcal{W}_{123}$	weight matrix for S1-S2-S3-combinations	
w_j	peak width in samples	
w_l	weight for combination - coupling included	
w_s	weight for combination - coupling not considered	
x	axial coordinate along pipe	m
α_L	thermal diffusivity	m^2/s
α_v	volumetric vapor ratio	
ε	scaling of moving standard deviation	
Δf	frequency resolution	Hz
Δp	initial amplitude of pressure oscillation according to Joukowsky equation	bar
Δp_C	tensile strength of a liquid	N/m^2
Δp_{tot}	pressure loss	bar
Δt	peak duration (LN_2)	s
$\Delta t_{01}, \Delta t_{02}, \Delta t_{03}$	travel time of noise onset from origin to sensors	s
Δt_{12}	delay between noise onset (chapter 5.2.2) in S1 and S3	s
Δt_{13}	delay between peak (chapter 5.2.1) / noise onset (chapter 5.2.2) in S1 and S3	s
Δt_{23}	delay between peak (chapter 5.2.1) / noise onset (chapter 5.2.2) in S2 and S3	s
Δv	deceleration of the liquid (flowing towards the valve) due to valve closure	m/s

Symbol	Description	Unit
Δv_i	deceleration of the liquid (flowing towards the tank) in the presence of cavitation	m/s
δ_T	thickness of thermal boundary layer	m
δ	peak prominence	bar
δ_{th}	peak prominence threshold	bar
Δx_{12}	distance between S1 and S2	m
Δx_{13}	distance between S1 and S3	m
Δx_{23}	distance between S2 and S3	m
η^+, η^-	tolerances for speed of sound	
θ	pipe slope	$^\circ$
ν	Poisson's ratio	
Λ	Peak	
ν_L	kinematic viscosity of liquid	m^2/s
π	Archimedes' constant	
ρ	density	kg/m^3
Σ	thermodynamic parameter in bubble dynamics	$m/s^{3/2}$
σ	standard deviation of pressure readings	bar
$\varphi_i \quad i \in (1,2)$	cluster parameters: slope of fit in first or second half of cavitation valley	
ω_p	angular frequency with maximum response of bubble	1/s

1 Introduction

Pressure surges are rapid changes in pressure that propagate through the system as pressure waves. They have the potential to cause devastating damage to such systems if they are not accounted for. Pressure surges are generally caused by sudden changes in flow velocity, as they occur for example when a valve is closed quickly. When designing any kind of fluid dynamic system the occurrence of pressure surges must be considered.

In the propellant feed system of space propulsion systems pressure surges can be created in various ways: From priming of evacuated feed lines to the valve closure at the end of chill-down or at engine shutdown. The extent of potential damage caused by such pressure surges can be seen from the fourth launch attempt of the soviet N-1 rocket, which was part of the manned lunar program N1-L3. The shutdown of the central engines of the first stage during flight caused pressure surges which led to the destruction of one of the oxygen pumps. The resulting fire caused the destruction of the launcher [1]. During development of the European Automated Transfer Vehicle (ATV) pressure surges with peak pressures above 220 bar were observed and required changes in the design [2].

Naturally, pressure surges occur in various other fields as well. An especially prominent example is civil engineering. Several accidents due to pressure surges were recorded in pipelines and hydropower stations, in some cases with tragic consequences. Some of them were attributed to pressure surges, where the rarefaction wave led to cavitation up to the rupture of the liquid column ("column separation") [3].

While the basic phenomenon of pressure surges is well understood and can be predicted accurately, the influence of cavitation is still hard to predict precisely by calculations. Most research so far was conducted with water as the test fluid since water is easy to handle and a fluid with many applications. However, in the field of liquid-propellant rocket engines, cryogenic fluids are commonly used. The cavitation behavior of cryogenic liquids is known to differ strongly from water. In order to assess the transferability of findings from water experiments to cryogenic liquids, it is therefore important to understand how these differences affect the pressure surge behavior.

This thesis is intended to contribute to this open field of research. Pressure surge experiments were previously conducted with both, water and liquid nitrogen (LN_2) at DLR Lampoldshausen.

The pressure surges were generated by rapidly closing a valve in a pipeline with initially steadily flowing liquid. The pressure was recorded at different locations along the pipe. During these tests pressure fluctuation exceeding the standard fluid hammer theory were observed during cavitation.

In this thesis certain aspects of these fluctuations will be investigated in detail and compared between water and LN_2. The focus will lie on the behavior of the noise intensity over time during the presence of cavitation, and on the interaction and relationship between pressure fluctuations in the cavitation region with fluctuations in the liquid column with the goal to establish hypotheses on the cause of those fluctuations.

2

Theoretical background

As a preparation for the evaluation, the important theoretical foundations will be discussed in the following. Focus will lie on the fluid hammer theory and the bubble dynamics of cavitation.

2.1 Pressure surges in pipelines

Pressure surges in general are rapid changes in pressure due to a change in flow velocity that propagate through liquid conveying pipelines away from their point of origin. While this work concentrates on pressure surges induced on the upstream side of a rapidly closed valve, it should be mentioned here that the valve closure also leads to a low-pressure wave travelling downstream. In space propulsion systems pressure surges can also occur during the priming process of evacuated feed lines [4]. Pressure surges can as well be induced by harsh shutdown and start of pumps [5, 6].

Classical pressure surge theory

The classical pressure surge theory will be explained on a simple system as depicted in Fig. 2.1. This system only consists of a tank, a pipeline and a fast closing valve. The tank is pressurized with p_0 and kept at this constant pressure. The ambient pressure behind the valve is p_a and the pipeline has the length L. A sequence where the fluid flows steadily into the environment at t_0 and the valve is closed at t_1 with an indefinitely small closure time shall be considered. The fluid at the valve is stopped abruptly and the pressure rises accordingly. The change in pressure and velocity propagates towards the tank with the speed of sound of the liquid a. This compression wave is reflected at the tank after L/a (t_2 in Fig. 2.2) which acts as an open boundary condition, meaning that the pressure needs to remain constant. Therefore a wave inducing a flow velocity towards the tank propagates towards the closed valve, where it is reflected after $2L/a$ at a closed boundary condition, which requires zero velocity. This leads to a low pressure wave traveling upstream which stops the flow. This wave is again reflected at the tank after $3L/a$ as a compensation pressure wave which goes along with a positive flow velocity (directed towards the valve). When this wave reaches the valve at t_3 or $4L/a$, the

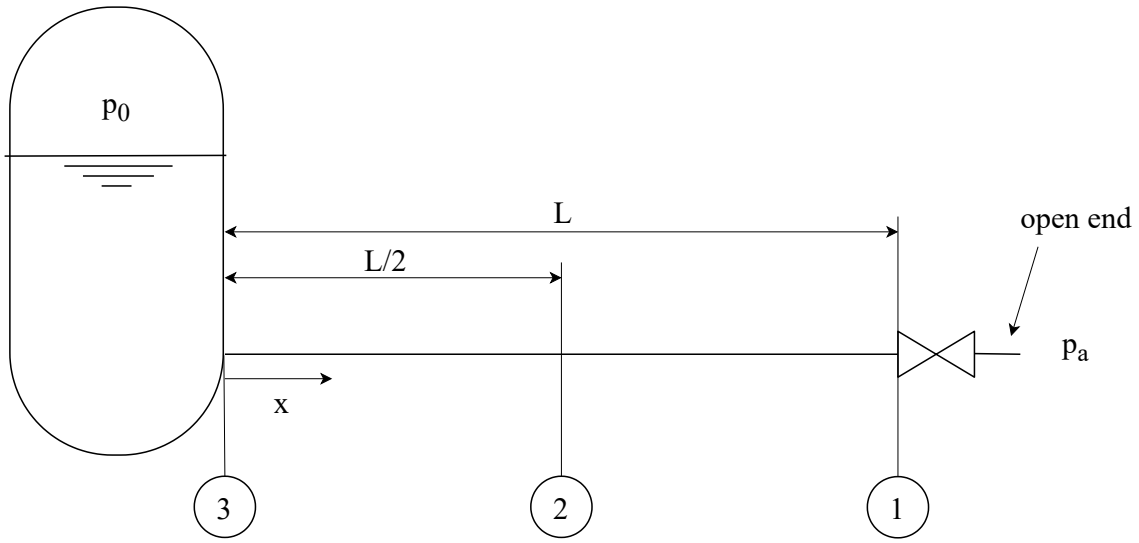

Figure 2.1: Exemplary system for fluid hammer consideration

initial conditions are restored (p_0 and v_0) which leads to a repetition of the cycle [5]. This idealized sequence is depicted in Fig. 2.2 with the pressure on the left and the velocity on the right.

Since the wave travels through the pipe four times during one cycle it becomes clear, that the duration of one cycle equals $4L/a$ and consequently the frequency of this main pressure oscillation equals $(4L/a)^{-1}$.

The initial pressure rise $\Delta p = p_1 - p_0$ depends on the change in momentum of the fluid. It can be determined by Joukowsky's equation [7]

$$\Delta p = \rho \cdot a \cdot \Delta v, \tag{2.1}$$

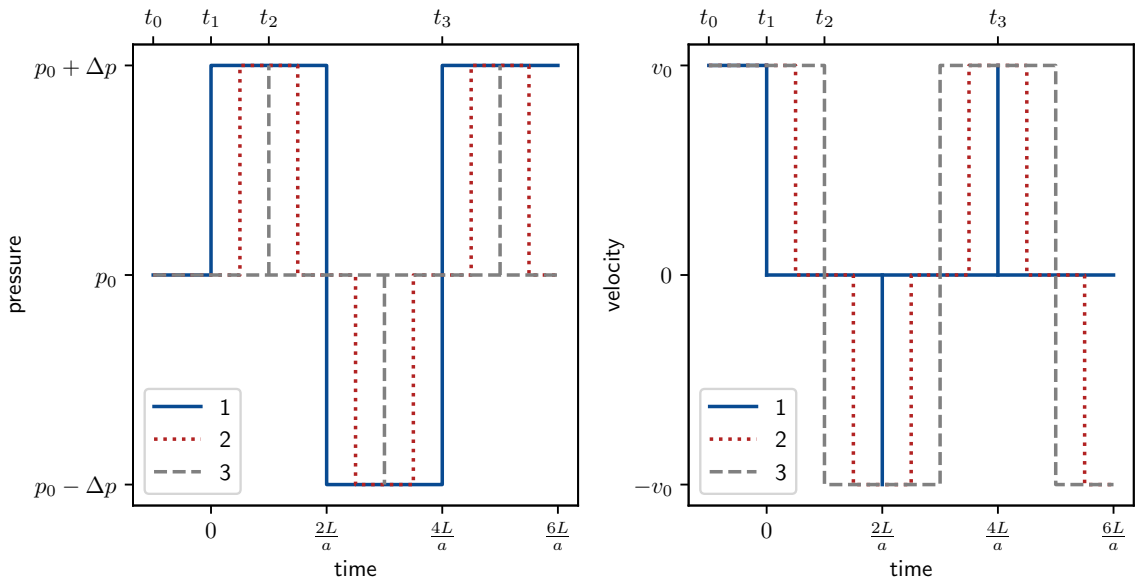

Figure 2.2: Idealized fluid hammer theory

with the fluid's density ρ, the speed of sound a and the change in velocity Δv. In the case of the complete closure of a valve the fluid is stopped to zero velocity, therefore Δv corresponds to the initial velocity v_0. In this case the maximum pressure rise Δp is reached if the valve closure time t_v is smaller than half a period of the cycle described above. This condition can be formulated as [3]

$$t_v < 2 \cdot \frac{L}{a}. \tag{2.2}$$

When neglecting friction (and if no cavitation is present), the pressure drop during the rarefaction wave has the same Δp as the initial pressure rise.

The speed of sound is an influential parameter in those considerations. In pipelines as considered in this thesis the speed of sound is not simply a fluid property but also depends on the elasticity of the pipe. This was already described by Korteweg in 1878 [8]. The speed of sound is therefore calculated as

$$a = \sqrt{\frac{K/\rho}{1 + [(K/E)\,(D/e)]\,c_1}}, \tag{2.3}$$

with the fluids bulk modulus of elasticity K and density ρ and the pipes Young's modulus E, diameter D and wall thickness e. The parameter c_1 is obtained from the Poisson's ratio ν by

$$c_1 = \frac{2e}{D}\,(1 + \nu) + \frac{D\,(1 - \nu^2)}{D + e} \tag{2.4}$$

for thick-walled pipes as used in this thesis. [9]

The oscillation of pressure and velocity along the pipe can be calculated with the fundamental 1D water-hammer equations [10]

$$\frac{\partial H}{\partial t} + v\frac{\partial H}{\partial x} - v\sin\theta + \frac{a^2}{g}\frac{\partial v}{\partial x} = 0, \tag{2.5}$$

$$\frac{\partial v}{\partial t} + g\frac{\partial H}{\partial x} + v\frac{\partial v}{\partial x} + \frac{fv \cdot |v|}{2D} = 0, \tag{2.6}$$

with the head $H = p/(\rho g)$, the pipe slope θ, the gravitational acceleration g, the Darcy-Weißbach friction factor f and the pipe diameter D. These water-hammer equations can be solved using the method of characteristics. Besides the one-dimensionality, this model is based on a few other assumptions: The wave speed is assumed to be constant. The effect of undissolved gas is therefore neglected. The pressure must not fall below the fluid's vapor pressure, so cavitation does not occur. And the pipe needs to be completely filled with liquid at any point in time. Additionally, fluid-structure interactions are assumed to be neglectable and linear elasticity is assumed for pipe wall and fluid. Lastly, the friction is approximated as quasi-steady [10].

In this work, the influence of cavitation on the pressure surge behaviour is of particular importance and shall be described in the following.

Pressure surges with cavitation

If the theoretical pressure change Δp would cause the pressure to drop below the vapor pressure of the liquid p_v the liquid is put under tension and cavitation can occur if nuclei are present.

Cavitation can develop in the form of distributed cavitation, that is, in the form of many separate vapor bubbles. Under severe conditions, single cavities can develop, which occupy almost the whole cross section of the pipe. This is known as column separation. The two types can be qualitatively distinguished via the volumetric ratio of vapor (V_v) and total mixture (V_m)

$$\alpha_v = \frac{V_v}{V_m}. \tag{2.7}$$

For local column separation the mixture consists almost entirely of vapor ($\alpha_v \approx 1$), where for distributed cavitation the liquid phase is dominant ($\alpha_v \approx 0$) [3]. Both types are sometimes referred to as *vaporous cavitation*, while the term *gaseous cavitation* is used to describe release of previously dissolved gas due to the pressure drop. In this case the bubbles don't collapse with rising pressure. Instead the gas re-dissolves only slowly (water: order of minutes) compared to the gas release (water: order of seconds) [3]. The gas bubbles can therefore effect the behavior even well after the pressure has risen above the vapor pressure again. Gas bubbles in a liquid effect the speed of sound c. From equation (2.1) it can be seen that this effects the pressure rise. In this work, however, the term *cavitation* is used only as defined in section 2.2.1 in the context of evaporation.

The development of cavitation corresponds to an increase in volume. Therefore the flow velocity towards the tank is not completely stopped but only reduced. The initial deceleration of the liquid can be determined by the actually possible pressure drop [3]:

$$\Delta v_i = \frac{1}{\rho a} \cdot (p_0 - p_v). \tag{2.8}$$

Here it is assumed, that the liquid actually cavitates at p_v so there is no retardation in boiling. The fluid keeps moving towards the reservoir with $v_1 = v_o - \Delta v_i$. The deceleration along with the pressure drop propagates towards the reservoir, which functions as an open end. The reflected wave causes the fluid to decelerate again by Δv_i. It is again reflected at the cavity which is serving as a open end (constant pressure) boundary condition. Here the velocity is again decreased by Δv_i. Thus during every time interval $2L/a$ the negative velocity decreases by $2\Delta v_i$. In this model-like consideration, the time between two main fluid hammer peaks is an integer multiple of $2L/a$. In this consideration the length of the cavity is neglected, therefore the location of reflection is at the valve. Otherwise L could not be viewed as constant and the frequency of the pressure fluctuations in the valleys would increase. This theory is visualized in a wave travel diagram in Fig. 2.3.

An approximation of the lifetime T_c of the first cavity is therefore given by [3]

$$T_c = \frac{\Delta p}{p_0 - p_v} \frac{2L}{a}. \tag{2.9}$$

The collapse of the cavity does not necessarily occur simultaneously with the arrival of the pressure wave. This collapse causes a rise in pressure lower than the Joukowsky pressure. But when the main pressure wave arrives, positive interference can cause the pressure to rise well above the Joukowsky pressure.

The spacial length of the cavity can be estimated by integrating the velocity of the liquid column. A slightly different approach is the rigid column theory. The elasticity of the liquid

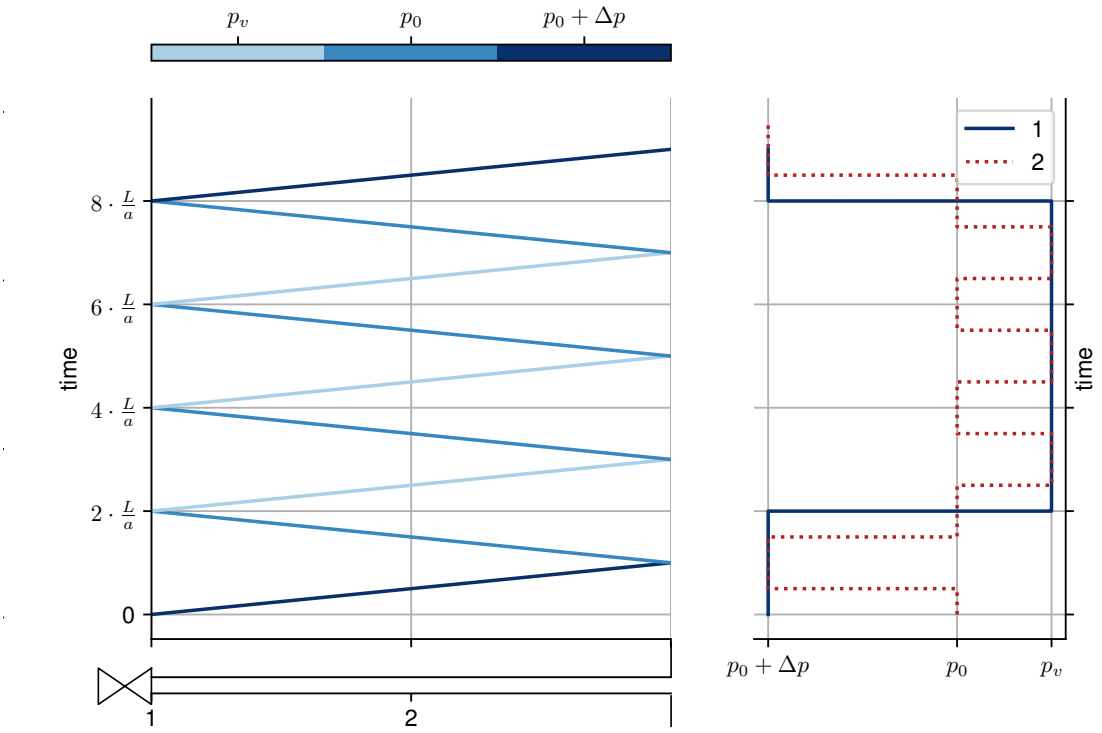

Figure 2.3: Simplified wave travel diagram for primary wave during cavitation

(thus the propagation of pressure waves) is neglected. The liquid is treated as a rigid cylinder of length L, on which the vapor pressure p_v acts on the side of the valve and the tank pressure p_t on the other side. This cylinder moves towards the tank with v_0. Now a simple differential equation for the motion of this cylinder can be used, based on the conservation of momentum:

$$\rho_l \cdot L \cdot \frac{dv}{dt} = p_v - p_t - \Delta p_{tot}, \tag{2.10}$$

with the liquid's density ρ_l and the combined pressure loss Δp_{tot} of pipe friction, losses in fittings and hydrostatic pressure difference if applicable [11].

Even though the first model considers spatial differences in pressure and velocity within the liquid column both methods provide the same insight: The velocity changes approximately linearly, therefore the length of the cavity has a parabolic course over time [3, 11].

More sophisticated one dimensional models have been developed to handle multiple vapor cavities (DVCM - *Discrete Vapor Cavity Model*) [9] and to handle the release of a second component gas (DGCM - *Discrete Gas Cavity Model*) [12].

Pressure surges in the context of space propulsion

There are various possibilities for pressure surges to occur in the propellant feed systems of rocket or satellite propulsion systems. When using cryogenic propellants, the piping needs to be cooled down prior to ignition (*chilldown*). One possible chilldown method is to vent the propellant into the environment [13]. Chilldown is stopped by closing the bypass valve, which can introduce pressure surges into the system. See Fig. 2.4 (left) for a simplified schematic

of such a feed system. The valve closure at engine shutdown is another potential source of pressure surges [14].

In satellites and spacecrafts in general an isolation valve separates the tanks from the engine during launch. Often pyrovalves are used due to their high reliability, but they come with the disadvantage of very fast operating times. When the valve is opened the propellant rushes into an evacuated line (priming) and hits against the still closed latch valve. This can cause intense pressure surges [15, 16]. Figure 2.4 (right) depicts a very simple feed system of a satellite propulsion system.

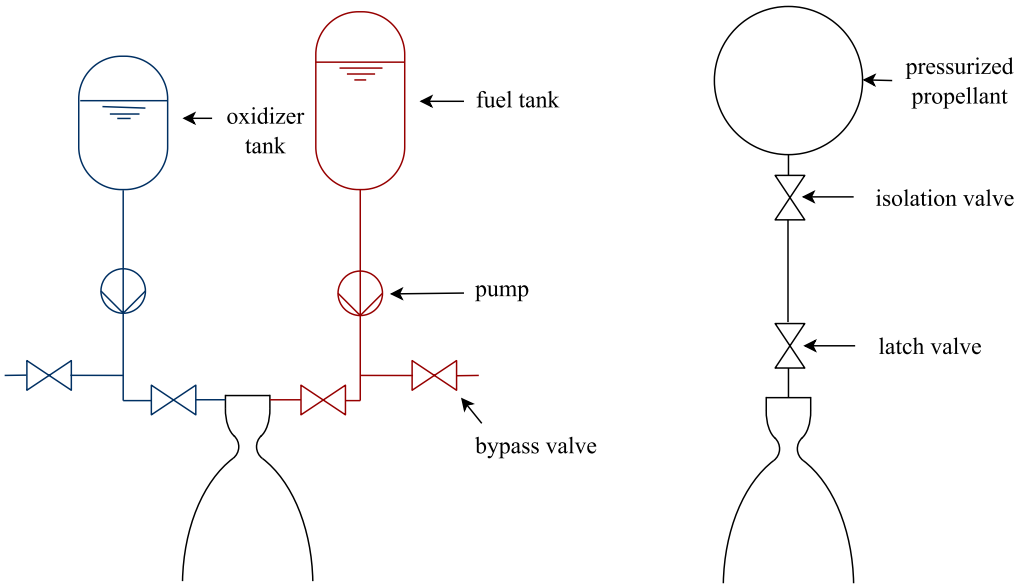

Figure 2.4: Simplified schematics of feed systems. Left: liquid rocket engine, right: satellite propulsion system

2.2 Cavitation

Cavitation is understood to be the abrupt vaporization and subsequent condensation of liquid due to local changes in pressure that reach below the vapor pressure. In the following, the basics of nucleation, bubble dynamics and bubble collapse will be discussed.

2.2.1 Nucleation

The formation of vapor bubbles is not trivial and does not necessarily occur as soon as the vapor pressure is undershot. It relies on the presence of boundary layers between a liquid and a gaseous phase [17]. Therefore either microbubbles or even microscopic vacancies in the liquid or gas entrapped in pores of solids (e.g. pipe wall or contaminating particles) are required. These are summarized under the term *nuclei*. In the absence of nuclei, a liquid can withstand tension without "breaking". Therefore pressures below the vapor pressure are possible without the occurrence of cavitation [18].

Generally, two types of nucleation can be distinguished: Homogeneous and heterogeneous nucleation. Homogeneous nucleation describes the occurrence of microscopic voids in the liquid due to the thermal motion of the molecules. This random type of nucleation does not require

contamination of free gas or solid particles. In contrast, heterogeneous nucleation is based on the presence of contaminant gas, either as microbubbles or as gas filled pores in wetted surfaces of solids [19].

For the homogeneous nucleation theory a nucleation rate J can be defined, describing the number of nucleation events per volume and time. This rate corresponds to a specific tensile strength Δp_C via [19]

$$\Delta p_C = \left[\frac{16\pi S^3}{3 k_B T \ln\left(J_0/J\right)} \right]^{\frac{1}{2}}, \tag{2.11}$$

with the surface tension S, Boltzmann's constant k_B, the temperature T and a factor of proportionality J_0, for which there are different possible formulations, but which is typically dependent on the molecular number density, the molecular mass and the surface tension.

It can be seen that for a specific tensile strength the nucleation rate has a strong dependence on the surface tension. The tensile strength is defined as

$$\Delta p_C = \frac{2S}{R_C}, \tag{2.12}$$

where R_C denotes the radius of the largest vacancy present. It can be understood as the pressure difference $p_v - p$ at which a bubble with radius R_C is in equilibrium. A further decrease in pressure p will lead to an unstable growth of the bubble. From this it can be seen that the pressure in the liquid surrounding the bubble needs to be slightly below the vapor pressure p_v to achieve equilibrium conditions [19].

2.2.2 Dynamics of spherical bubbles

The bubble dynamics can be examined on a single spherical bubble with radius $R(t)$ surrounded by an infinite domain of liquid with pressure p_∞ and temperature T_∞, where the pressure is considered to be a function of time while the temperature is assumed to be constant. Furthermore, the liquid's density ρ_L and dynamic viscosity μ_L are assumed to be constant.

The motion of the liquid around the bubble will be considered in radial direction. Based on the Navier Stokes momentum equation the Rayleigh-Plesset equation can be derived. Here it is assumed that no mass transfer occurs over the boundary of the bubble. If the vapor density is much smaller than the liquid density this approximation is valid even with evaporation or condensation occurring at the boundary. In its simple formulation the Rayleigh-Plesset equation is [19]

$$\frac{p_B(t) - p_\infty(t)}{\rho_L} = R\frac{d^2R}{dt^2} + \frac{3}{2}\left(\frac{dR}{dt}\right)^2 + \frac{4\nu_L}{R}\frac{dR}{dt} + \frac{2S}{\rho_L R}, \tag{2.13}$$

with the pressure inside the bubble p_B and the kinematic viscosity of the liquid ν_L. If the pressure inside the bubble is known, this function provides the bubble radius $R(t)$ as a reaction on a change in pressure $p_\infty(t)$. However, since the bubble can contain non-condensable gas and the temperature inside the bubble T_B can differ from the liquids temperature, the left

side of the equation can be expanded as follows [19]:

$$\frac{p_B(t) - p_\infty(t)}{\rho_L} = \frac{p_v(T_\infty) - p_\infty(t)}{\rho_L} + \underbrace{\frac{p_v(T_B) - p_v(T_\infty)}{\rho_L}}_{(1)} + \frac{p_{G_0}}{\rho_L}\left(\frac{T_B}{T_\infty}\right)\left(\frac{R_0}{R}\right)^3. \tag{2.14}$$

Here p_{G_0} denotes the partial pressure of the contaminant gas at the reference state (R_0, T_∞).

The term annotated with (1) in equation (2.14) is called thermal term. It can have major influence on the bubble dynamics but there are many cases where it is appropriate to neglect this term. If this term is neglected for a moment and it is assumed that $T_\infty \approx T_B$,it can be shown that the response of a bubble on a sudden drop in pressure from p_∞ to p_∞^* is an initially accelerated growth that turns into a linear increase of the bubble radius, which corresponds to a volumetric growth of the bubble like t^3.

The impact of the thermal term depends on thermal properties of the fluid: From the structure of the term it is obvious that the sensitivity of the vapor pressure regarding changes in temperature is very important. Assuming $\rho_L \gg \rho_V$, the Clausius-Clapeyron equation yields [19, 20]

$$\left(\frac{dp_v}{dT}\right)_{T_\infty} \approx \frac{\rho_v(T_\infty) L_{vap}(T_\infty)}{T_\infty}, \tag{2.15}$$

with the latent energy of evaporation L_{vap}. Linearization of the thermal term for modest temperature differences $T_B - T_\infty$ therefore leads to [19]

$$\frac{p_v(T_B) - p_v(T_\infty)}{\rho_L} \approx \frac{\rho_v(T_\infty) L_{vap}(T_\infty)}{\rho_L T_\infty}(T_B - T_\infty). \tag{2.16}$$

Besides the dependence on L_{vap} it becomes clear, that the ratio of vapor and liquid density plays a decisive role. For the temperature difference the heat diffusion in the liquid as well as the evaporation mass rate have to be considered. An approximation for small thermal boundary layers $\delta_T \ll R$ shows the proportionality [19]

$$T_\infty - T_B(t) \propto \frac{L_{vap}\rho_v}{\rho_L c_{p_L} \alpha_L^{\frac{1}{2}}}. \tag{2.17}$$

The same influences as in (2.16) can be observed. In addition the specific heat capacitance c_{p_L} and the thermal diffusivity α_L of the liquid have an effect. Those influences can be summarized in the thermodynamic parameter Σ [19]

$$\Sigma(T_\infty) = \frac{L_{vap}^2 \rho_v^2}{\rho_L^2 c_{p_L} T_\infty \alpha_L^{\frac{1}{2}}}, \tag{2.18}$$

which directly, proportionally effects the thermal term. It is important to note that the thermal term in its simplified form is proportional to $t^{n-\frac{1}{2}}$ with $0 < n < 1$ for bubble growth and $n = 1$ for the constant, asymptotic growth. The thermal term therefore gains importance during the bubble growth. For the previously mentioned case of a step-function-like drop in pressure to p_∞^* a critical time t_{c1} can be defined as [19]

$$t_{c1} = \frac{p_v - p_\infty^*}{\rho_L} \cdot \frac{1}{\Sigma^2}, \tag{2.19}$$

after which the order of magnitude of the thermal term is comparable to that of the other terms in the Rayleigh-Plesset equation. The growth is then considered to be thermally controlled in contrast to the inertially controlled first phase. The greater the thermodynamic parameter Σ the earlier the thermally controlled growth sets in.

Earlier it was mentioned that the bubble radius grows linearly with t in its asymptotic growth phase if the thermal term is neglected. Now it can be shown, that in the thermally controlled case the asymptotic growth rate is proportional to $\sqrt{t}$ [19]. The growth is therefore strongly slowed down.

In an oscillating pressure field, a bubble will respond with an oscillating radius. The frequency with the maximum response is defined as [19]

$$\omega_p = \left[\frac{3k_p \left(\bar{p}_\infty - p_v\right)}{\rho_L R_E^2} + \frac{2\left(3k_p - 1\right) S}{\rho_L R_E^3} - \frac{8\nu_L^2}{R_E^4} \right]^{\frac{1}{2}}, \tag{2.20}$$

with k_p being the polytropic exponent ($k_p = 1$ if the gas inside the bubble behaves isothermally), the mean pressure in the distant liquid $\bar{p}_\infty$, the bubble radius R_E at equilibrium at $\bar{p}_\infty$ and the kinematic viscosity of the liquid ν_L.

2.2.3 Bubble collapse

If a bubble with R_0 is exposed to increasing pressure it begins to shrink. This process can get quite violent. After some minimum bubble size R_{min} is reached, the bubble will grow again, leading to an oscillation about a reduced radius. The minimum size is affected by the amount of contaminant gas in the bubble. If the gas content was zero, the bubble would collapse completely to $R_{min} = 0$ and the collapse velocity at the end of the collapse would be infinitely large. For this hypothetical case the duration of collapse can be estimated, based on the Rayleigh-Plesset equation as [21]

$$t_{TC} = 0.915 \left(\frac{\rho_L R_0^2}{p_\infty^* - p_v} \right)^{\frac{1}{2}}, \tag{2.21}$$

also called the Rayleigh time, with the new, increased ambient pressure p_∞^*. The violence of the collapse may violate the assumption of incompressibility in the liquid. A collapsing bubble usually does not remain spherical, violating another assumption of the Rayleigh-Plesset equation. Nonetheless those assumptions allow for a conservative estimation of the collapse, since in reality the actual collapse will be less severe [19].

The collapse of a bubble produces a pressure pulse that gets radiated into the surrounding liquid. The pressure of this pulse p_P as a function of distance to the bubble r can be estimated as

$$p_P \approx \frac{100 R_0 p_\infty}{r}, \tag{2.22}$$

as a function of the maximum bubble radius before collapse R_0. This demonstrates the severity of bubble collapse and demonstrates that cavitation can produce noise and vibration as well as damage nearby solid surfaces. As for the bubble growth, the thermal effect can influence

the bubble collapse significantly after a critical time [19]

$$t_{c4} = \left(\frac{R_0}{\Sigma}\right)^{\frac{2}{3}}. \tag{2.23}$$

2.3 Previous related research

Various studies dealt with the characteristics of cavitation in cryogenic fluids. In general it is found that the thermodynamic effect plays a dominant role in cryogenics during bubble growth [22, 23]. Since the operating conditions for cryogenics are usually closer to the critical point than for water [24], the ratio of vapor and liquid density ρ_v/ρ_L is much higher than for example in water at atmospheric conditions. The definition of the thermodynamic parameter (2.18), stresses the importance of this ratio. The thermal conductivity of the liquid phase is small, which benefits the development of temperature gradients close to the cavitation bubbles and therefore a lower temperature inside the bubbles [22]. The influence of the thermal effect leads to a large number of bubbles while the bubble sizes are very small. In water at room temperature in contrast, usually few but large bubbles form. This was observed in various visual studies that compared the cavitation behavior of liquid nitrogen with water [23–25]. In the context of fluid hammer, visual investigations performed by Traudt et. al. [26] showed the formation of large cavitation bubbles in water. Various other fluids were studied visually (e.g. ethanol [27], acetaldehyde [27] and oil [28], but published visual investigations of cavitation during cryogenic fluid hammer is not known to the author.

It was reported, that the erosive damage from cavitation was found to be less severe in cryogenics than in water [24]. This fits well to the theoretical consideration, since larger bubbles produce higher pressure spikes upon collapse and the thermal effect also slows down the collapse.

Fluid hammer experiments have been conducted with cryogenic fluids mainly in the context of priming of propellant feedlines. The focus of those studies was the validation and improvement of numerical methods to simulate multi-phase fluid hammer with the goal of representing the timing and amplitude of the main pressure peaks correctly [27, 29, 30].

High-frequency pressure fluctuations during the cavitation phase of pressure surge cycles were investigated previously at DLR Lampoldshausen. Tests in water showed strong pressure peaks during cavitation [26]. It was assumed that those peaks were the pressure wave traveling between cavity and tank. Klein et al. [31] found that dominant frequencies in the liquid phase in water correspond to the natural frequencies of open/open resonators and concluded that cavitation acts as an open acoustic boundary condition. The noise intensity for consecutive cavitation valleys in water and liquid nitrogen was investigated in [14]. Noise was defined here as pressure fluctuations above 250 Hz. It was found that the intensity is greater in water by one order of magnitude. While the noise intensity seems to decay linearly in LN_2 between consecutive cavitation valleys, it seemed to remain constant for water and only started to decay when no cavitation occurred anymore.

3

Test bench

The data for this work comes from the **F**luid **T**ransient **T**est **F**acility (FTTF) at DLR Lampoldshausen [14, 26]. This test bench was set up in two different configurations to allow experiments with different test fluids. The configuration FTTF-1 was used to perform tests with water at room temperature, the cryogenic configuration FTTF-2 was used with liquid nitrogen.

The basic setup is the same for both configurations: A high pressure tank is connected to a low pressure tank via the test section. This test section is designed as a coil with 1.5 turns to reduce the space occupied in the lab. The pipe is therefore slightly inclined towards the valve with a slope of 0.62°. The tanks and the pipes are made out of stainless steel of grade 1.4541. A fast closing valve (Axius 1400 S) is installed close to the low pressure tank. The valve closing time is about 22 ms [26]. A coriolis flow meter (Emerson CMF50M) is placed between the valve and the low pressure tank.

In both configurations pressurization of the tanks is done with gaseous nitrogen. The FTTF-2 configuration needs additional peripherals in terms of insulation. The tanks are double-walled tanks whose outer shell is filled with liquid nitrogen which is kept at a pressure just above ambient pressure by a check valve with an opening pressure < 0.3 mbar. The liquid nitrogen in the inner tank can be pressurized and therefore kept well below boiling point. The test section is insulated by a vacuum jacket and the fast closing valve as well as the flow meter are encased by insulating foam.

In the test section sensors are positioned at three locations S1, S2, S3 along the pipe. The exact locations can be taken from Tab. 3.1. It is important to point out that the middle sensor position S2 deviates strongly between the two configurations. While FTTF-1 has its S2 position close to S3 near the high pressure tank, FTTF-2 has a much more evenly distributed sensor positioning. The overall setup and the sensor positioning is depicted in Fig. 3.1. As shown in this figure, the test section does not lead directly into the tank. However, at the specified start of the test section the piping has a drastic change in diameter, which decouples the test section from the section before it.

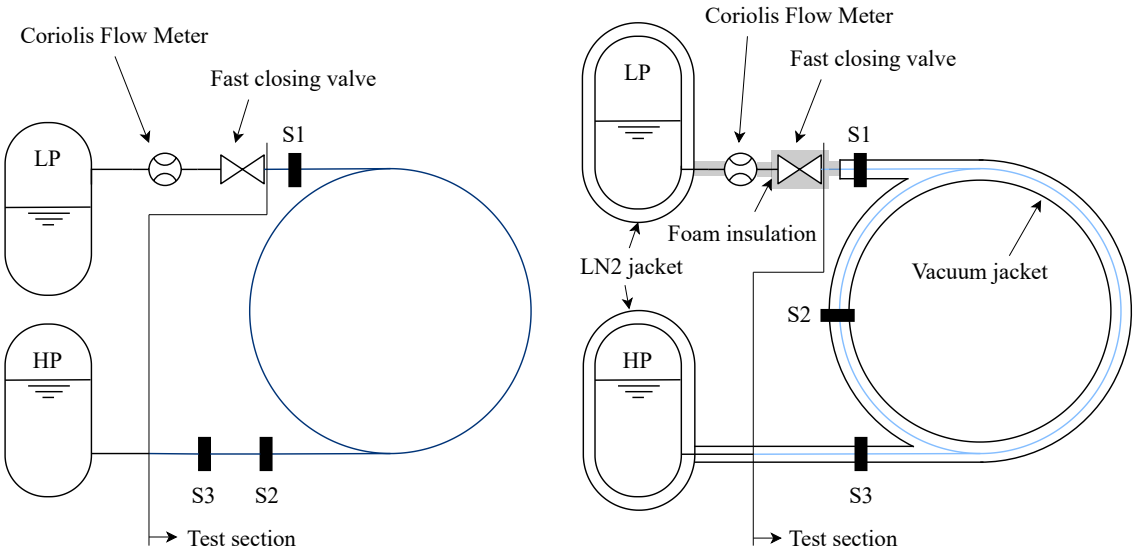

Figure 3.1: Test bench setup: FTTF-1 (left), FTTF-2 (right)

Table 3.1: Test section dimensions

Parameter		**FTTF-1**	**FTTF-2**
Length	l	7.671 m	9.294 m
Inner diameter	d_i	19 mm	19 mm
Wall thickness	e	1.5 mm	1.5 mm
Sensor position S1	x_1/l	3.9 %	6.5 %
Sensor position S2	x_2/l	88.6 %	47.3 %
Sensor position S3	x_3/l	97.8 %	88.2 %

Each location contains a dynamic pressure sensor (p_{dyn}) (Kistler 601), a static pressure sensor (p) (FTTF-1: Kistler 4043A-100, FTTF-2: Kulite CTL-190S-2000A) and a temperature sensor (T) (type K thermocouple). The sampling rates as well as the cut-off frequency of the anti aliasing filters are listed in Tab. 3.2 for those sensor types. The pressure sensors have a measurement error of ± 0.552 bar. The temperature sensors have a measurement error of ± 3.7 K (FTTF-2) and ± 2.7 K (FTTF-1).

In preparation for the tests at the FTTF-1, the water is stored over night in order to reduce the amount of dissolved gas. The FTTF-2 needs to be cooled down prior to the tests.

Table 3.2: Sampling rate and anti aliasing frequency for sensor types

Sensor type	**Sampling rate** (kS/s)	**Anti aliasing frequency** (kHz)
Dynamic pressure	150	30
Static pressure	10	2
Temperature	1	0.2

Therefore, before each test the LN_2 is pumped between the low and high pressure tank to ensure a properly chilled down test section.

A test run is then started by letting the fluid flow from the high to the low pressure tank until steady conditions are reached. In FTTF-2, the LN_2 is let to flow longer than in FTTF-1 to compensate for possible heat input into the fluid in the test section before the test start. After that the valve is closed and the resulting pressure oscillations are recorded.

4

Test data overview

This work is based on the data produced in a previously conducted test campaign. In the following an overview over the available data will be given. As a preparation for the later evaluation, the data is clustered according to characteristic features of the pressure readings.

4.1 Test campaign

The test campaign generated 164 valid tests in water during which cavitation occurred. The pressure levels in the high and low pressure tanks represent the decisive boundary conditions and were changed between the tests. This results in different initial flow velocities. An overview over the tests used in the later analysis is given in Fig. 4.1. Since there was no additional flow regulating device installed, the flow velocity results directly from the pressure differences. Therefore only the initial velocity v_0 and the initial pressure in the high pressure tank $p_{0_{hp}}$ is shown. The ranges for those boundary conditions can be taken from Tab. 4.1.

109 valid tests with cavitation were generated using liquid nitrogen. Those tests can be seen in Fig. 4.1 as well. Refer to Tab. 4.1 for the boundary condition ranges. 16 tests showed invalid data from the dynamic pressure sensor at S3. Those tests can be used for analysis which only require the data from S1 and/or S2, but have to be excluded if sensor S3 needs to be considered as well. Those tests are referred to as *partial* in Fig. 4.1. Figure 4.2 shows the pressure reading at S1 for an exemplary test in water.

Table 4.1: Ranges of boundary conditions

Boundary condition	**H_2O**		**LN_2**	
	min	max	min	max
$p_{0_{hp}}$ (bar)	1.44	32.38	1.84	28.08
$p_{0_{Lp}}$ (bar)	0.98	31.15	0.30	19.53
v_0 (m/s)	1.26	6.29	3.31	242.85

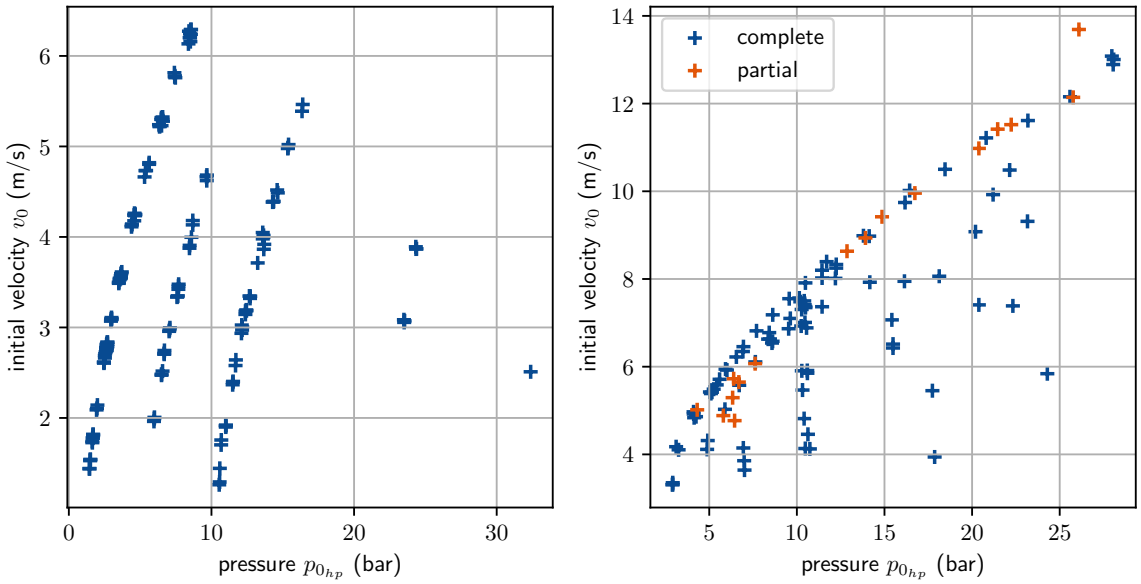

Figure 4.1: Overview over the boundary conditions of the tests. Left: H_2O, right: LN_2

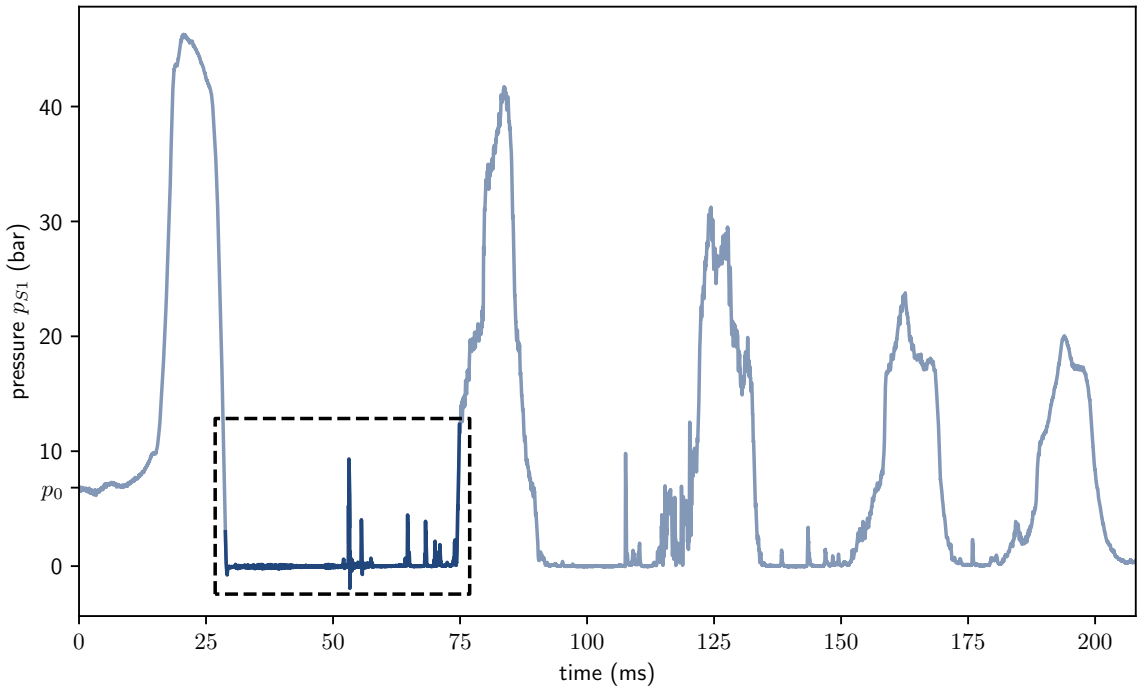

Figure 4.2: Exemplary pressure reading (S1) from a test with cavitation in water

4.2 Clustering

In the later analysis the focus lies on the *cavitation valleys*, one of which is highlighted in Fig. 4.2. From a first inspection of the test data it is apparent that those valleys differ very strongly for different boundary conditions and are sometimes hardly comparable. Not only the length of the valleys varies greatly but also the general shape and various features like high frequency noise onset and short duration peaks have very different characteristics. Some examples of the pressure readings at position S1 are shown for water and LN_2 in Fig. 4.3 to

demonstrate the wide range of cavitation valleys. The definition of start and end points of those valleys are described further below. For those readings the time scales are normalized by the expected wave travel time through the pipe t_{ref} with length l at a wave propagation speed a, which is calculated via the Korteweg equation (which takes into account the elasticity of the pipe) [32] for the initial conditions just before valve closure :

$$t_{\text{ref}} = l/a \tag{4.1}$$

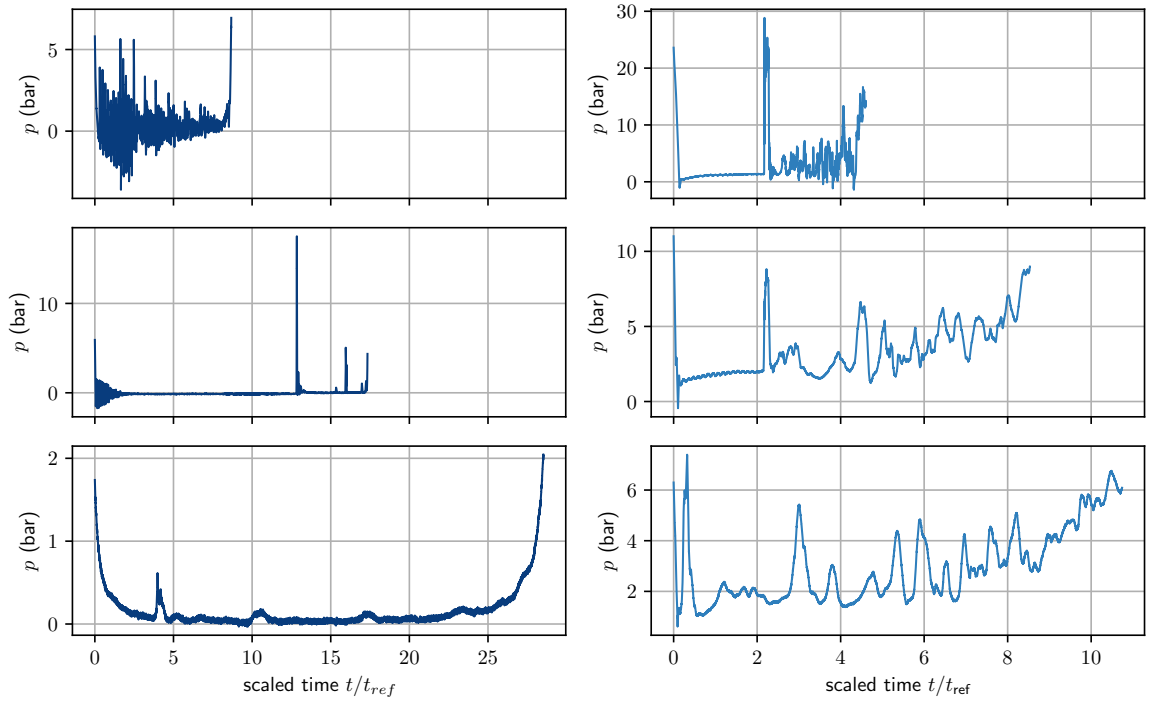

Figure 4.3: Examples of different cavitation valleys measured at S1. Left: water, right: LN_2

It becomes clear that applying evaluation routines on all tests per fluid may not provide particularly informative results. Recurring patterns may only become visible in groups of similar tests. Therefore it is advisable to cluster the tests before proceeding with the analysis. The tests will be clustered based on characteristics in their pressure readings at S1 during the first cavitation valley.

The start and endpoints of those valleys are defined via the crossing points of the p_{S1} reading with the high pressure tank reading p_{hp}. Since the tank pressure slowly rises after valve closure, using the initial values as a constant reference would not be accurate. Here, the static pressure sensors are used, to exclude intermediate pressure spikes that occur in the dynamic pressure readings in the cavitation valley. Empirical conditions have to be defined to exclude crossing points that occur due to higher frequency fluctuations instead of the actual pressure surge waves. Therefore pairs of consecutive crossings are discarded if the time difference is smaller than Δt_{min} with $(\Delta t_{min})_{\text{H}_2\text{O}} = 7$ ms and $(\Delta t_{min})_{\text{LN}_2} = 20$ ms. The difference between the two fluids comes from the vastly different speeds of sound.

4.2.1 Cluster parameters

The characteristics of those valleys are described by various parameters that will be defined in the following. They describe the valleys shape and noise characteristics.

Shape characteristics

A set of parameters is defined to describe the general shape of the valley by comparing it to a reference square wave, which would be the idealized theoretical shape. The lower limit of this square wave p_{ref} is defined by the median of the pressure readings in the first halt of the valley

$$p_{\mathrm{ref}} = \mathrm{median}\left[\left(\underline{\boldsymbol{p}}_{\boldsymbol{S1}}\right)_{0\leq\tilde{t}<0.5}\right], \tag{4.2}$$

with the time $\tilde{t}$ being normalized to go from 0 to 1 in each valley. The set of pressure samples is denoted as $\underline{\boldsymbol{p}}_{\boldsymbol{S1}}$. For valleys with a pronounced horizontal part, this reference pressure usually coincides well with the pressure in this part. The pressure is now normalized using the initial tank pressure in the high pressure tank $p_{0_{hp}}$ and p_{ref} so that the interval $[0, 1]$ corresponds to $[p_{\mathrm{ref}}, p_{0_{hp}}]$:

$$\tilde{p} = \frac{p_{S1} - p_{\mathrm{ref}}}{p_{0_{hp}} - p_{\mathrm{ref}}}. \tag{4.3}$$

To describe the shape with only a few single parameters, a linear function $f_i(\tilde{t})$ is fitted per half of the valley. The error function that is used for fitting is extremely important. The common least squares fitting would be very susceptible to short peaks. It is important here that only the low frequency trend is expressed in the fits. For that it proved to be beneficial to use a logistic function of the form

$$e(d) = \frac{1}{1 + e^{-k(d-d_0)}}, \tag{4.4}$$

with the error e and the absolute difference between fit and sample d. The parameters k and d_0 can be chosen to influence the shape of the function. A parameter study for those parameters will be conducted later in this section. In general this function weights very small differences only weakly. But the penalization is increasing quickly with larger deviations. At some point large deviations are treated equally, reducing the impact of short but high peaks. The procedure described so far is visualized in Fig. 4.4.

Now the parameters used for clustering are:

- $\mathbf{A}_1$, $\mathbf{A}_2$: The areas between the linear fits and $\tilde{p} = 0$ calculated as

$$A_i = \frac{1}{\tilde{t}_{\mathrm{max},i} - \tilde{t}_{\mathrm{min},i}} \sum_{\tilde{t}_j \in \underline{\tilde{\boldsymbol{t}}}_{\boldsymbol{i}}} f_i\left(\tilde{t}_j\right) \Delta\tilde{t}, \quad i \in \{1, 2\}, \tag{4.5}$$

  with the set of sample times per half $\underline{\tilde{\boldsymbol{t}}}_{\boldsymbol{i}}$, the spacing between the normalized time samples $\Delta\tilde{t}$ and the minimum and maximum normalized times per half $\tilde{t}_{\mathrm{min},i} = \min\left(\underline{\tilde{\boldsymbol{t}}}_{\boldsymbol{i}}\right)$, $\tilde{t}_{\mathrm{max},i} = \max\left(\underline{\tilde{\boldsymbol{t}}}_{\boldsymbol{i}}\right)$.

- $\boldsymbol{\varphi_1}$, $\boldsymbol{\varphi_2}$: The slopes of the linear fits, calculated as

$$\varphi_i = \frac{f_i\left(\tilde{t}_{\mathrm{max},i}\right) - f_i\left(\tilde{t}_{\mathrm{min},i}\right)}{\tilde{t}_{\mathrm{max},i} - \tilde{t}_{\mathrm{min},i}}, \quad i \in \{1, 2\}. \tag{4.6}$$

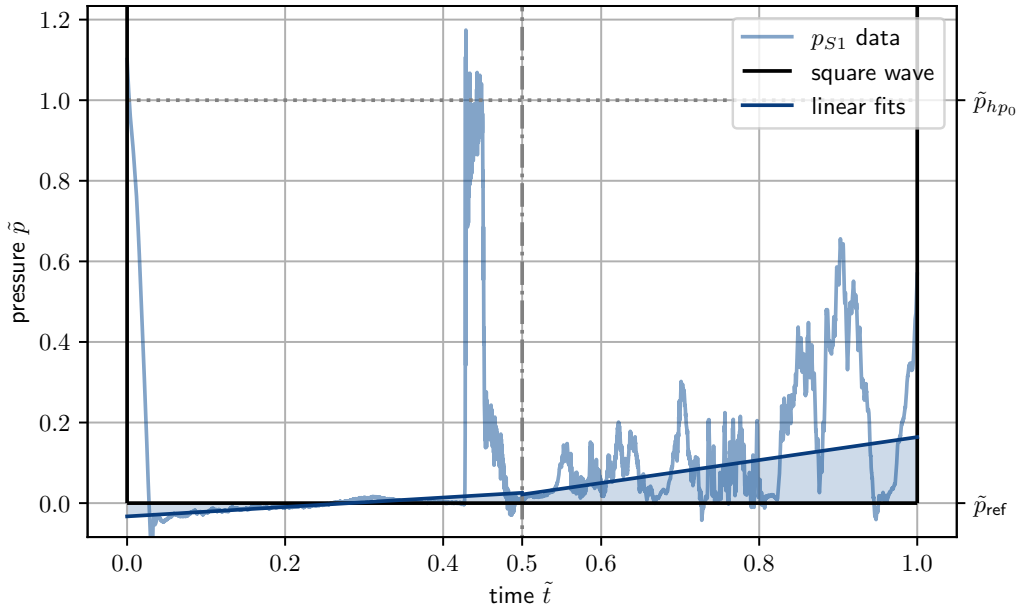

Figure 4.4: Demonstration of linear fits on exemplary cavitation valley (LN_2)

Spread

Another parameter is supposed to characterize the deviation of the pressure signal from the *"expected"* value, which is represented by the reference p_{ref} from above. The same scaling as above is applied, so the pressure is again referred to by $\tilde{p}$. For this purpose short but large deviations are allowed to have a great effect on the parameter, allowing for a simple definition like

$$s = \text{mean}\left[\text{abs}\left(\underline{\tilde{\boldsymbol{p}}}\right)\right]. \tag{4.7}$$

Since the reference pressure p_{ref} equals $\tilde{p} = 0$ after scaling, this formulation represents the mean deviation of the signal from the reference pressure.

However, the start and end transients are not representative since the selection of the start and end points leads to large inherent differences between the tests. For some tests the transient is not included in the valley and for others with only a slightly smaller gradient almost the whole transient from $p_{0_{hp}}$ to p_{ref} is included. This would cause inconsistencies in the spread. Therefore the linear fits described above are utilized again. The valley is cropped between the first crossing of signal and linear fit in the first valley t_{x1} and the last crossing in the second half t_{x2}. This is visualized in Fig. 4.5. The definition of the spread s is now

$$s = \text{mean}\left[\text{abs}\left(\left(\underline{\tilde{\boldsymbol{p}}}\right)_{t_{x1}\leq t\leq t_{x2}}\right)\right]. \tag{4.8}$$

Parameter study for error function

Since the parameters k and d_0 in (4.4) have to be chosen somewhat arbitrarily, a parameter study will be performed in order to make a well-grounded choice. The parameter d_0 shifts the position of the infection point in d-direction, k determines the maximum steepness. Reasonable

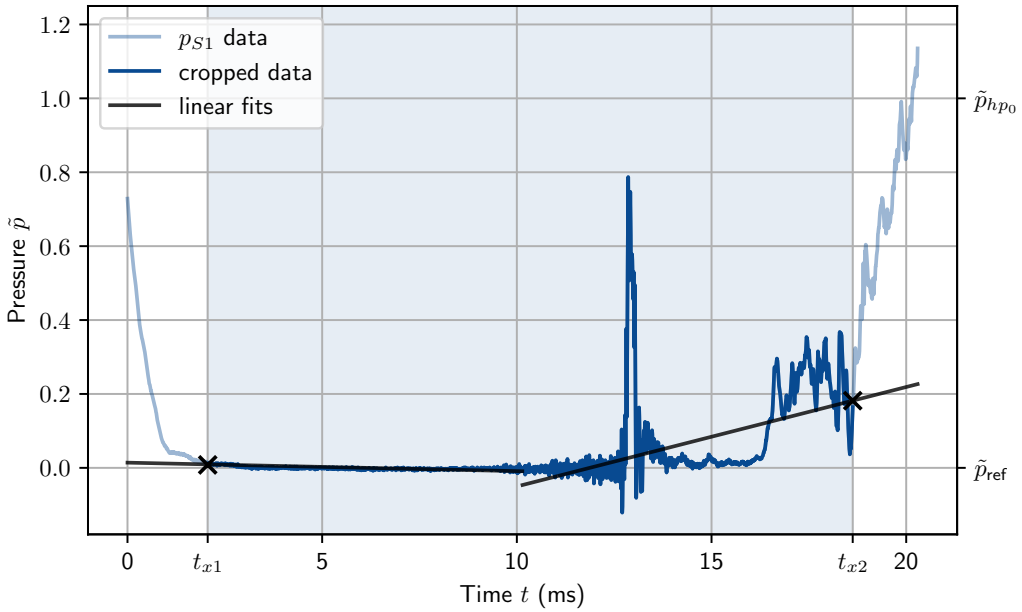

Figure 4.5: Visualization of cropping

ranges for those parameters were found to be $d_0 \in [0, 0.5]$ and $k \in [10, 100]$, considering that the majority of the values for d are expected to lie between 0 and 1. Per parameter 20 different values within those ranges were considered.

Since there is no way to define *the right* combination, a parameter combination is desired for which small deviations in those parameters don't effect the results in a significant way. The procedure of this study is as follows:

- For each test in the data set do the following:
  - Calculate all dependent clustering parameters (A_1, A_2, φ_1, φ_2 and s) for the total of 400 parameter combinations
  - Scale the results of each parameter according to $[\min(var), \max(var)] \rightarrow [0, 1]$ with $var \in \{A_1, A_2, \varphi_1, \varphi_2, s\}$
- Calculate the mean value for each cluster parameter for each parameter combination over all tests
- Calculate the euclidean norm of the gradient of $var(k, d_0)$ for every cluster parameter var at every parameter combination (k, d_0)

$$g_{var} = \|\nabla var(k, d_0)\|_2 = \left\| \begin{matrix} \frac{\partial var}{\partial k} \\ \frac{\partial var}{\partial d_0} \end{matrix} \right\|_2 \tag{4.9}$$

  The results of this step are shown in Fig. A.1 in the appendix.
- Scale this gradient according to $[\min(g_{var}), \max(g_{var})] \rightarrow [0, 1]$ per cluster parameter.
- Calculate the mean scaled gradient for each parameter combination over all cluster parameters.

This mean scaled gradient is shown in Fig. 4.6. As previously stated, a parameter combination with a small gradient is desired. Since the distribution shows a clear region with particularly small gradients, one can simply take the combination with the minimum gradient. This combination is marked in Fig. 4.6. The chosen parameters are consequently $k = 15$ and $d_0 = 0.1$. The resulting error function is plotted in Fig. A.2.

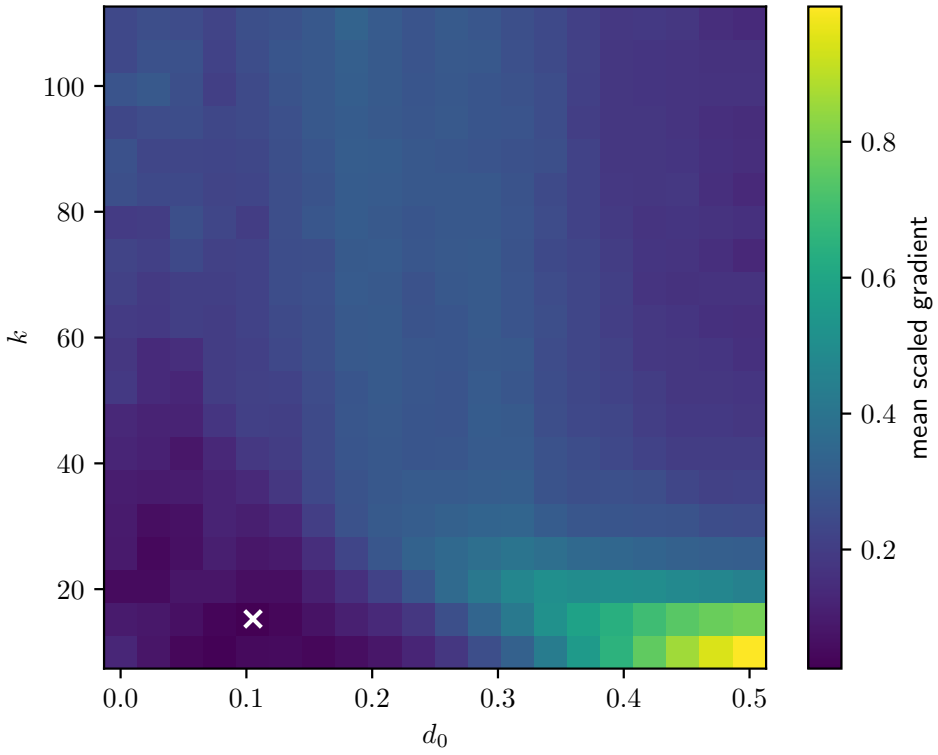

Figure 4.6: Mean gradient over parameter combinations

Noise onset

There are various ways of defining noise and its onset. Here the low-amplitude, high-frequency noise is not of interest. Instead the cluster parameter derived in this section is supposed to describe the point at which the signal starts to deviate from the flat horizontal part that is expected by theory. Since this transition usually comes with pressure fluctuations, it can be determined via peaks in the pressure readings. However, in water there are many test cases in which a strong oscillation occurs directly following the initial pressure drop. This oscillation is not the phenomenon that should be covered by the noise onset parameter. It is often decaying quickly and is then followed by a flat region. The peaks during this oscillation therefore must not be confused with the noise onset, which requires a method for excluding those peaks.

As a first step the signal is smoothed via a moving average with window size $N = 2 \cdot \lfloor \frac{N'}{2} \rfloor - 1$, where $N' = \frac{\mathrm{n}}{100}$ with the number of samples n. This step excludes the high-frequency noise, which is necessary for reliably separating the initial oscillation.

Then the initial drop in pressure is cut from the signal, since it may distort the frequency analysis, which will be performed in a later step. This is simply done by only considering the signal after the first local minimum. The number of samples is therefore reduced to n'. The greyed-out area in Fig. 4.7 shows the discarded initial transient.

Now, a peak detection is performed on the signal. The peak detection condition is that its prominence is greater than 0.1 for water and 0.15 for liquid nitrogen. Those values were determined empirically. A sensitivity study for this parameter might be appropriate for the future, but the chosen values already produced satisfactory clustering results that could be used for further analysis. The prominence is defined as the difference between the peaks maximum and the highest base. The bases are the minimum values between the peak and the next higher peak to either side.

Next, a Fast Fourier Transform (FFT) is performed on the first fifth of the remaining valley, which is approximately where the initial oscillation is prominent. This range is denoted as A from now on with $n_A = \lfloor n'/5 \rfloor$ samples. From the resulting frequency spectrum the frequency with the highest amplitude is assumed to be the main frequency of the initial oscillation f_{io} under the condition that the frequency is larger than $\left(\frac{n_A}{2 \cdot f_s}\right)^{-1}$, with the sampling frequency f_s. In other words, at least two periods of the oscillation must fit within the first fifth of the cropped valley. A single peak is thus not considered as the initial oscillation. Based on this frequency it can be evaluated which peaks can be part of this oscillation. With the frequency resolution of the FFT result Δf, which can be obtained via $\Delta f = \frac{f_s}{n_A}$, the expected distances d_s in samples between two consecutive peaks lie within the range $[d_{s_{min}}, d_{s_{max}}]$, with

$$\begin{aligned} d_{s_{min}} &= \left\lfloor \frac{f_s}{f_{io} + \Delta f/2} \right\rfloor, \\ d_{s_{max}} &= \left\lfloor \frac{f_s}{f_{io} - \Delta f/2} \right\rfloor. \end{aligned} \tag{4.10}$$

The first peak within range A is used as a starting point and is therefore included by default. From there it is checked for all consecutive peaks (Λ_i, Λ_j) if the neighboring peak is within the expected range via the condition

$$(\Lambda_j + w_j - \Lambda_i \geq d_{s_{min}}) \wedge (\Lambda_j - w_j - \Lambda_i \leq d_{s_{max}}). \tag{4.11}$$

The peaks width w_j is evaluated at half of the peaks prominence height. It is visualized by the thin light blue stripes in Fig. 4.7. If the gap between two peaks is too large or too small, the first of the two is considered the end of the initial oscillation and the second is considered to be the noise onset. Here it is again checked, if the oscillation consists of at least two peaks. So far, the noise onset was expressed as the index of the sample at which the specific peak was detected minus half the peak width w. With the timestamp of the resulting sample $t_{s,no}$ and the timestamp of the first sample of the valley $t_{s,0}$ the noise onset can be expressed in terms of elapsed time $t'_{no} = t_{s,no} - t_{s,0}$. The cluster parameter is this time, normalized by the reference time (4.1):

$$t_{no} = \frac{t'_{no}}{t_{\text{ref}}}. \tag{4.12}$$

If no peaks were detected at all, the noise onset is set to the last sample of the valley.

The length of the oscillation l_{io} will be needed later in this work and can simply be defined as

$$l_{io} = \Lambda_{io,end}, \tag{4.13}$$

where $\Lambda_{io,end}$ denotes the index of the last peak, that is part of the initial oscillation.

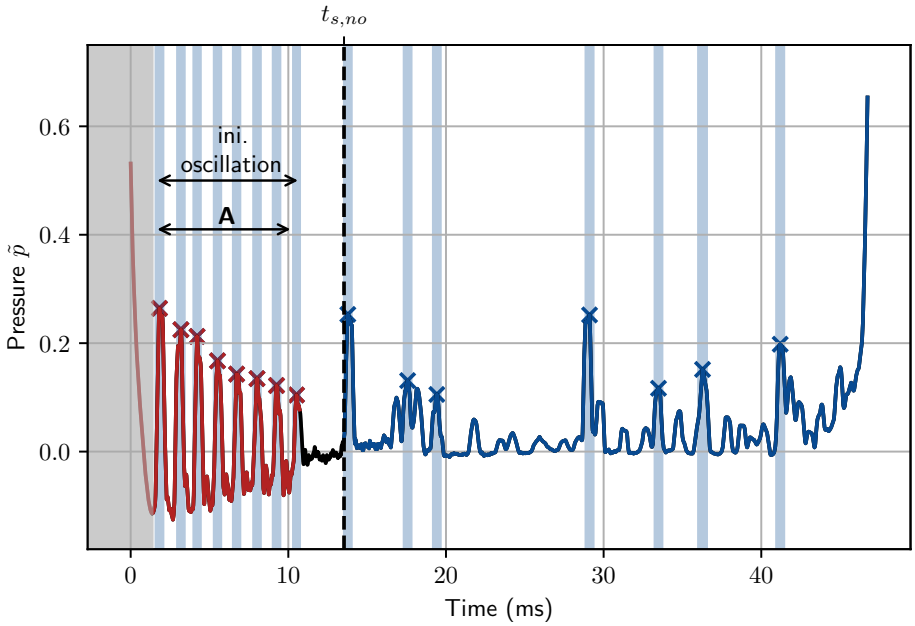

Figure 4.7: Definition of noise onset

Valley length

Lastly the valley length is used as an additional cluster parameter. It is simply defined as the valley duration relative to twice the reference time:

$$l_v = \frac{t_{s,end} - t_{s,0}}{2 \cdot t_{\text{ref}}}. \tag{4.14}$$

The theoretical valley length for cases without cavitation would consequently be $l_v = 1$.

4.2.2 K-Means Clustering

K-Means Clustering is a simple unsupervised learning algorithm. It clusters a data set by finding cluster centers iteratively. Each iteration consists of (1) assigning the data points to their nearest center and (2) updating the position of the centers as the mean of all previously assigned data points. This procedure is repeated until there is either no significant change in assignments or a maximum number or iterations is reached. [33]

With such clustering algorithms the problem of choosing *"the right"* number of clusters arises. A very simple approach is to calculate the sum of squared distances (Sum of Squared Errors, SSE) of the samples to their corresponding cluster center for various different number of clusters k. If at a certain k the change in SSE decreases significantly, that k can be a good choice ("elbow method"). A more advanced approach is the silhouette method. A silhouette coefficient s_c can be calculated for each sample which evaluates how well the sample is clustered. A value of +1 indicates very good clustering, while -1 indicates misclassification. The mean s_c over all samples can be used as an indicator for the performance of the overall clustering. So a k with a high mean s_c is favored. [34]

The data is clustered by considering the parameters defined in section 4.2.1. The tests are consequently points in a 7-dimensional space $(A_1, A_2, \varphi_1, \varphi_2, s, t_{no}, l_v)$.

For each fluid the data set is scaled as a first step. Here, the mean is set to zero and the variance to one. This scaling is applied for each feature independently. This ensures that no feature dominates over the others just due to its order of magnitude.

The number of clusters k is chosen to be $k_{H_2O} = 4$ for water and $k_{LN_2} = 7$ for LN_2. The SSE does not show a single abrupt change in slope for any of the fluids (see Fig. 4.8 on the left). It would, however, suggest to use either 4 or 7 clusters in water and 7 or 9 clusters in LN_2. For clarification the silhouette method is used (see Fig. 4.8 on the right). Inspection of the different valley types reveals that choosing $k = 2$ is not sufficient for the purpose of targeted evaluation. In LN_2 $k = 7$ and $k = 8$ have almost the same s_c. In this case it was seen that choosing $k = 8$ just leads to an additional almost empty class compared to $k = 7$.

The clustering results are visualized in Fig. 4.9 for water and Fig. 4.10 for LN_2. The tests are plotted according to their Joukowsky pressure and the difference between system and vapor pressure. It can be seen that the clusters, which were revealed only with information gathered from the first cavitation valley, also correspond to clusters considering the boundary conditions. In liquid nitrogen this is even more obvious than in water.

The cluster sizes can be taken from Fig. A.3 in the appendix. The focus of this work will be on the largest two clusters (0,1). Refer to the spider web representations in Fig. A.5 (water) and Fig. A.4 (LN_2) for insight into the cluster centers.

The most prominent clusters in water are:

- **Class 0:** Characterized by a short initial oscillation and a relatively early noise onset. This class is spread over all branches and is not confined to a specific Δp-range. But it tends towards higher $(p_0 - p_v)$.
- **Class 1:** Mainly differentiated from class 0 by a late noise onset. Those test lie on the first branch which corresponds to the lowest pressure $p_{0,lp}$. Within this branch they are widely spread.

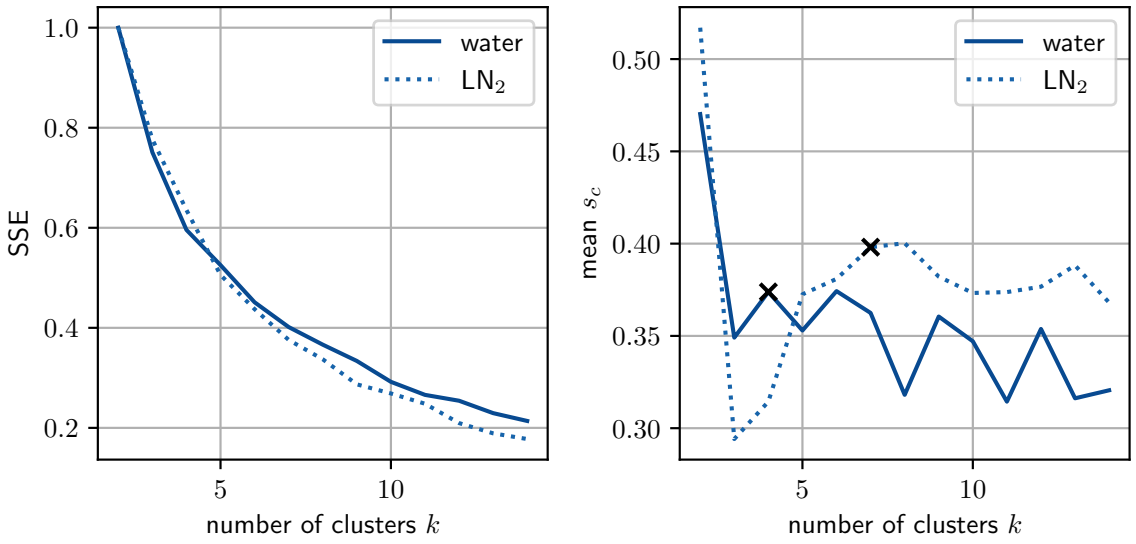

Figure 4.8: Effect of different numbers of clusters k. Left: "elbow" method, right: silhouette method

- **Class 2:** Characterized by a pronounced initial oscillation and early noise onset. The valleys are considerably shorter. Those tests are mainly located on the third branch with a few outliers. Within this branch no clear preference for a Δp-range is apparent.

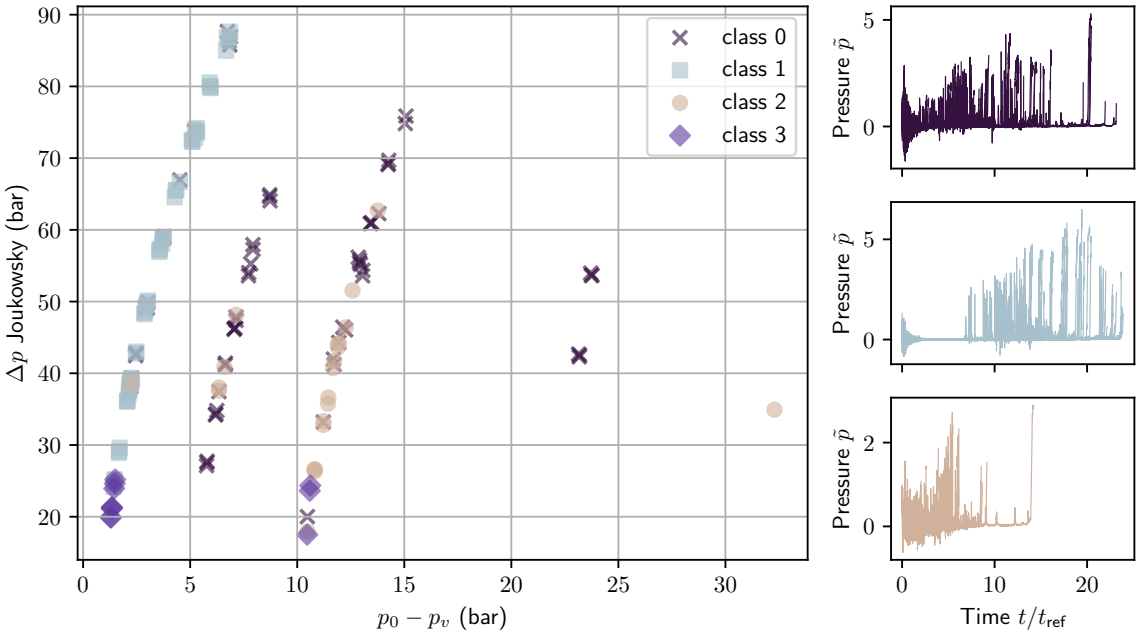

Figure 4.9: Clustered H_2O-tests and their boundary conditions

In LN_2 the most important clusters are:

- **Class 0:** Characterized by a strong peak at around $t/t_{\text{ref}} \approx 2$ and a long slowly rising part afterwards. This class can be associated with relatively small system pressures and medium Joukowsky pressures. It has a principal component in the Δp-$(p_0 - p_v)$-plane for which the variance is comparably small.

- **Class 1:** Characterized by the same peak around $t/t_{\text{ref}} \approx 2$, but with a much shorter overall valley length. Those tests correspond to high initial system pressures but are widely spread regarding the Joukowsky pressure.

- **Class 2:** Characterized by an early noise onset. The strong peak is absent for a large portion of the tests. This class is located at relatively small system pressures and small Joukowsky pressures.

The small figures in Fig. 4.9 and 4.10 are overlays of the first cavitation valley of all tests from the particular cluster.

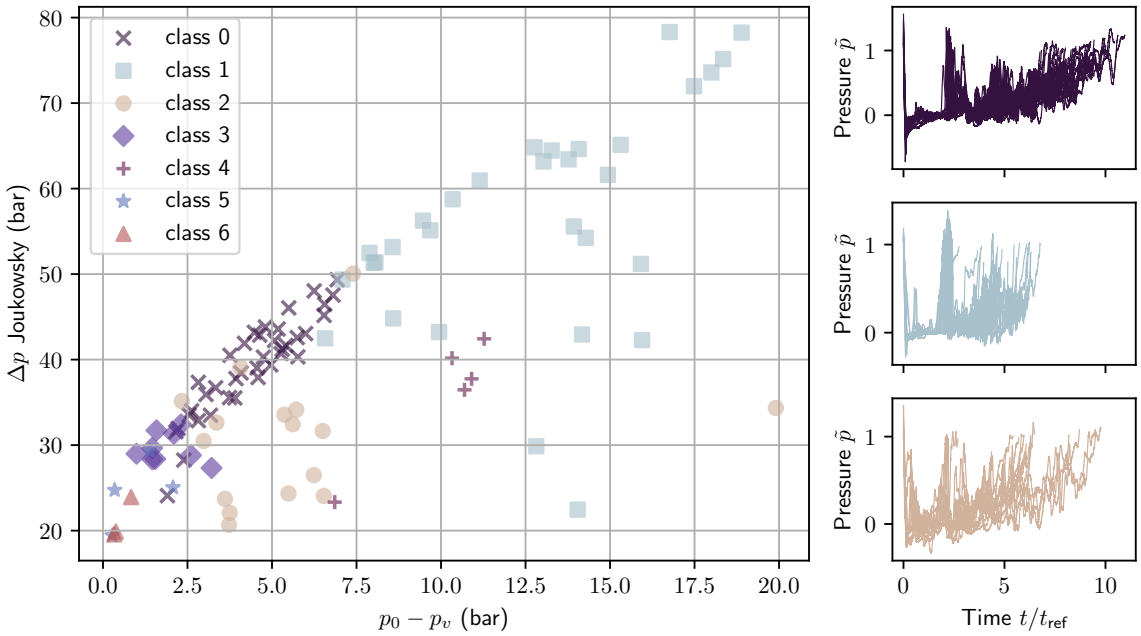

Figure 4.10: Clustered LN_2-tests and their boundary conditions

5 Analysis

In the following, the statistical evaluation of the noise behavior over time will be conducted, based on the previously obtained clusters. Subsequently, certain distinctive features in the pressure readings will be investigated in detail.

5.1 Noise Over Time

The development of the noise intensity over consecutive cavitation valleys was investigated in [14]. It might provide additional insight to consider the development of noise intensity over time within the individual cavitation valleys.

First, it must be defined, what exactly is considered as noise here. In general all pressure fluctuations that are not directly linked to the main fluid hammer wave, can be considered as noise. This distinction can be made by frequency considerations, assigning all fluctuations with a frequency above a threshold to the noise. Various harmonic frequencies of the main wave frequency were found during the cavitation valleys, therefore it was chosen to allow for a large margin between the expected wave frequencies and the lowest noise frequency. The chosen frequency band for the noise is 1-30 kHz. The upper bound originates from the use of the anti-aliasing filter with a cutoff frequency of 30 kHz. A common measure of intensity of oscillations is the root mean square (RMS). For the examination of the intensity over time, a moving RMS will therefore be used.

5.1.1 RMS over time

The following analysis is performed separately for each cluster, defined in chapter 4.2. For each individual cavitation valley the signal is bandpass filtered according to the chosen frequency band (1-30 kHz in this case). The moving RMS is calculated on this filtered signal. The filter width N is chosen to cover one period of the lowest frequency in the specified range f_{min}:

$$N = \left\lfloor \frac{1}{f_{min}} \cdot f_s \right\rfloor, \tag{5.1}$$

with the sampling rate f_s.

The goal is to evaluate the course over time for all corresponding cavitation valleys from all tests within the specific cluster. For that the time needs to be discretized in order to compare the RMS-course at the same points in time between different tests. To make the time comparable, it is first normalized by t_{ref}. The discretization in time is now chosen according to the smallest resolution in time from the set of cavitation valleys that will be compared to one another. The signals from tests with higher resolution will therefore be downsampled. This is done by calculating the mean of the samples falling into the same time-bin.

Afterwards common statistics such as mean, median and interquartile-range (IQR) can be determined at each point in time. Those are plotted in Fig. 5.1 for example. Those plots can be viewed as a series of boxplots over time, with the additional mean. Since not all valleys within the cluster have the exact same lengths, it must be kept in mind that the statistics are based on less data with progressing time. Therefore the number of tests contributing to the statistics are plotted as well.

Observations: LN_2

The results for clusters 0 and 1 in LN_2 are shown in Fig. 5.1 and Fig. 5.2 for the first two cavitation valleys. In general it can be seen, that the IQR can get very large temporarily, indicating a wide spread distribution. Still the mean value sometimes exceeds the IQR-boundaries. This shows that the mean is influenced strongly by outliers in many cases. The median should therefore be considered as the more reliable measure. In the first cavitation valley, at position S1 a flat region with very little noise can be seen after the initial transient. As mentioned briefly in chapter 4.2, the clusters 0 and 1 in liquid nitrogen are characterized by a strong peak in the raw pressure readings of S1 at a normalized time around 2. It can be seen that the noise increases strongly at this point as well. As the IQR is especially large at that point, it is apparent that, even though the peak is a common feature in those clusters, the intensity of the noise differs greatly. Cluster 1 shows a second peak in noise intensity around $t/t_{\text{ref}} = 4$. In cluster 0 this peak is replaced by two consecutive peaks, one shortly before and one shortly after $t/t_{\text{ref}} = 4$. Around $t/t_{\text{ref}} = 5$ the noise increases again and decays afterwards.

At position S2 the noise increase from the initial transient comes slightly later at around $t/t_{\text{ref}} = 0.3$. Similar to S1 the noise intensity afterwards is small followed by the increase around $t/t_{\text{ref}} = 2$. The peak in noise intensity is shifted towards $t/t_{\text{ref}} = 2.5$. Afterwards the median in cluster 1 has another maximum shortly before $t/t_{\text{ref}} = 4$. In cluster 0 in contrast, this increase is only visible in the IQR. The median has a short drop at that time.

At S3, the noise intensity is first very small. The rise that can be assigned to the initial transient takes place at around $t/t_{\text{ref}} = 0.6$ in cluster 0 and around $t/t_{\text{ref}} = 0.75$ in cluster 1. Subsequently the noise decreases but stays at a higher level than in S1 and S2. The following peak takes place at around $t/t_{\text{ref}} = 3$ in both sensor positions. A second rise is apparent around shortly after $t/t_{\text{ref}} = 4$ in cluster 0 and around $t/t_{\text{ref}} = 5$ in cluster 1.

The delays of the first peak fit to the expected delay for a propagation from S1 to S3 with the calculated speed of sound. However, the peaks are much broader in S2 and S3. The delays of the rising edges of those peak therefore only fit to a propagation from S2 to S3, since

the rising edge in S1 comes later. The second peak is less consistent. Here, no substantive statement can be made about a possible propagation between the sensors.

In the second valley (right column in the figures) the initial transients in S1 and S2 seem to be less sharp. In cluster 1 the subsequent phase of low noise intensity is still present, just like the increase around $t/t_{\text{ref}} = 2$. However, compared to the first valley, here the peak takes place slightly earlier. Interestingly, in S2 this rise appears to be split in two separate peaks, which are positioned in time almost symmetrically around the peak in S1. In cluster 0 there is a short drop after the initial transient but followed by an early rise well before $t/t_{\text{ref}} = 2$. Note

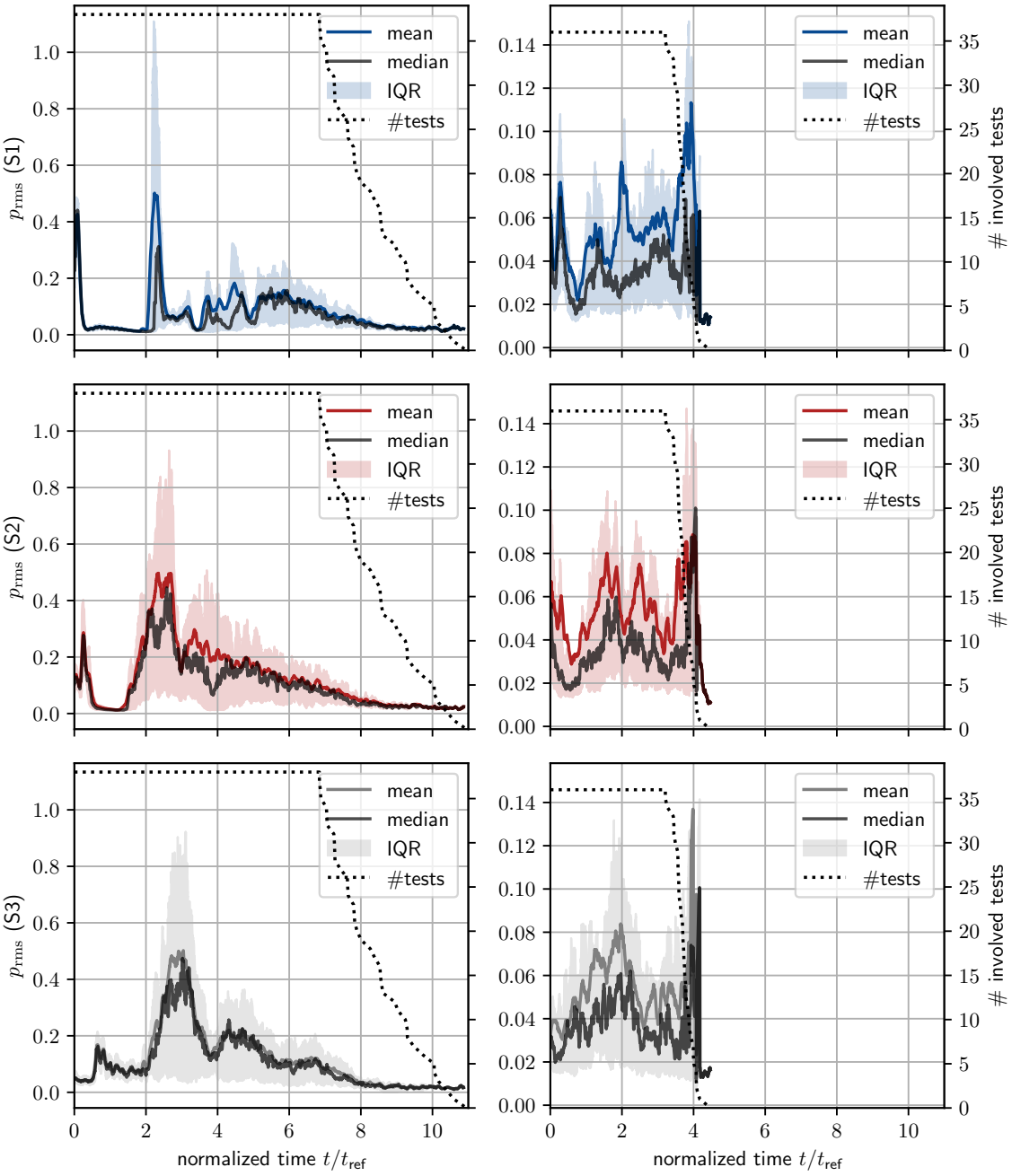

Figure 5.1: LN_2, cluster 0: Noise over time for the first (left column) and second (right column) cavitation valley, at sensors S1 (top), S2 (middle), S3 (bottom)

that the order of magnitude of the noise is much smaller here compared to the first valley and also compared to cluster 1.

S3 shows an increase around $t/t_{\text{ref}} = 2$ in cluster 0 but no significant movement in cluster 1, considering the mean. Note that the strong increase at $t/t_{\text{ref}} = 4$ is not very conclusive since the data set only consists of two tests at this point.

The results for the other clusters are shown in the appendix (Fig. A.6 to A.8). But since they consists of only few tests, they are not suitable for drawing conclusions.

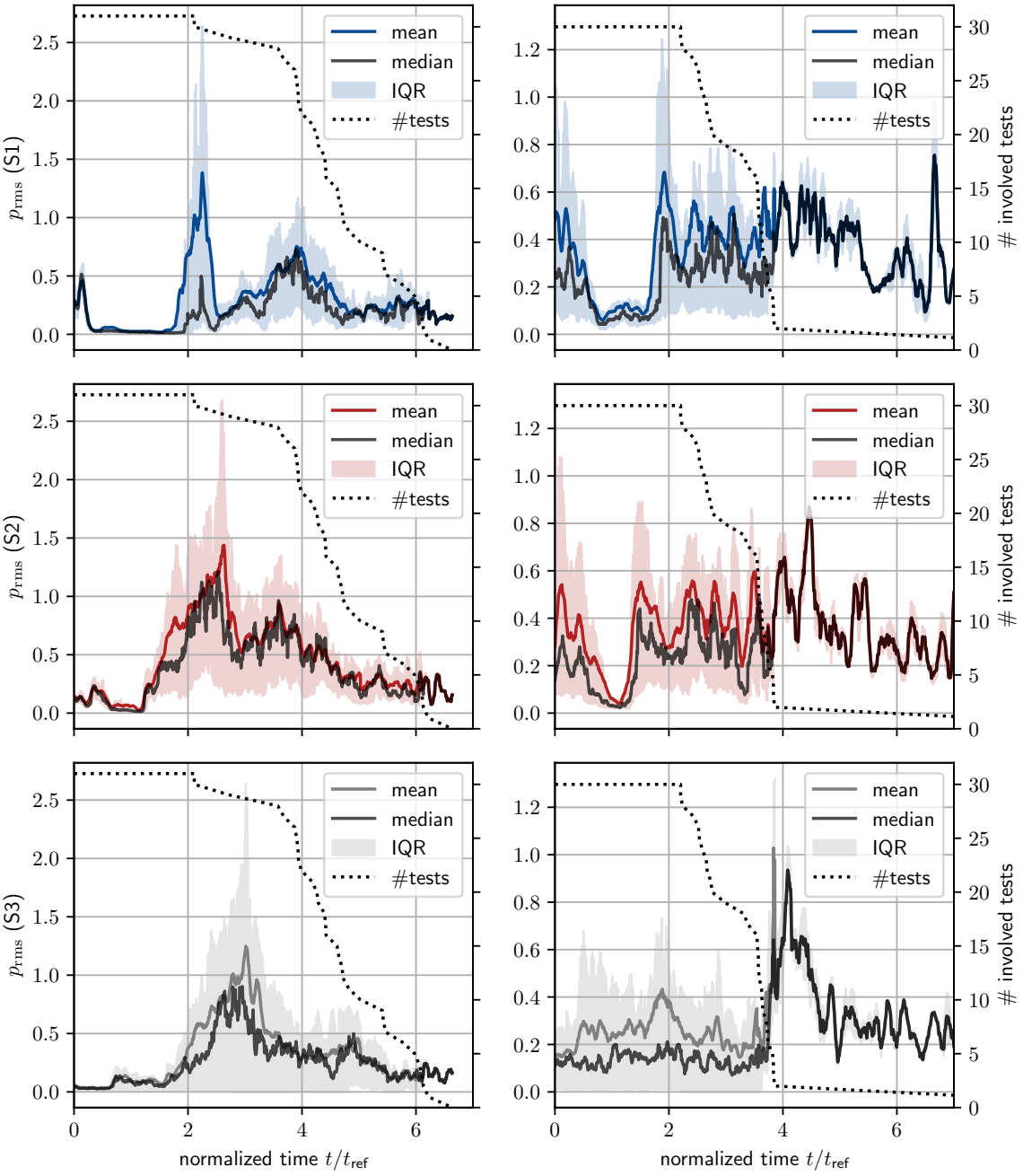

Figure 5.2: LN_2, cluster 1: Noise over time for the first (left column) and second (right column) cavitation valley, at sensors S1 (top), S2 (middle), S3 (bottom)

Observations: Water

The results for class 0 and 1 in water are shown in Fig. 5.3 and Fig. 5.4 for the first two cavitation valleys. In water it stands out that the median noise intensity is small and flat in S1 over most of the valley length. In the beginning intense noise is present which decays smoothly and quickly within less than $t/t_{\text{ref}} = 2$. This can be attributed to the initial oscillation mentioned before in chapter 4.2. The phenomenon of such an oscillation in cavitating flow behind a tension wave is described in literature as well [35]. The mean and IQR shows a strong fluctuation in the noise intensity along the whole valley in cluster 0 and in the second half of the valley in cluster 1. This can be assigned to the short term pressure spikes. That they don't

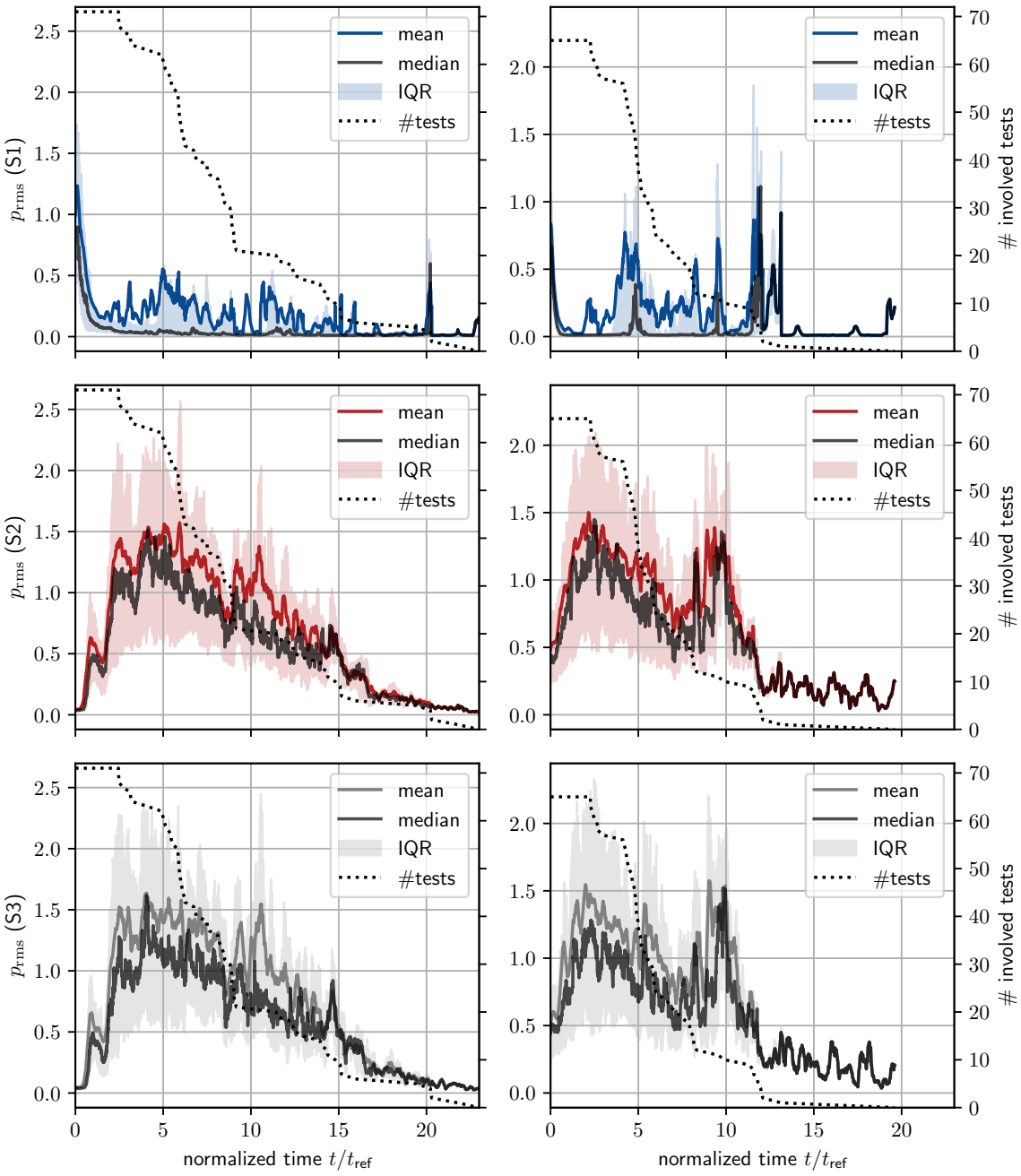

Figure 5.3: Water, cluster 0: Noise over time for the first (left column) and second (right column) cavitation valley, at sensors S1 (top), S2 (middle), S3 (bottom)

have an influence on the median suggests that that the timing of those peaks is random, since from an accumulation of peaks at a certain time it would be expected that the median reacts accordingly.

At positions S2 and S3 the noise intensity is low at the beginning and increases around $t/t_{\text{ref}} = 1$. In cluster 0 this increase is only weak but it is followed by a second and stronger increase at $t/t_{\text{ref}} = 2$. A third step-wise increase occurs around $t/t_{\text{ref}} = 4$. Afterwards the intensity is decreasing steadily. However, it should be noted that at this point the number of considered test is decreasing rapidly as well. Therefore it is not necessarily the case that the noise intensity drops at this point. It could also be that the longest valleys simply are the

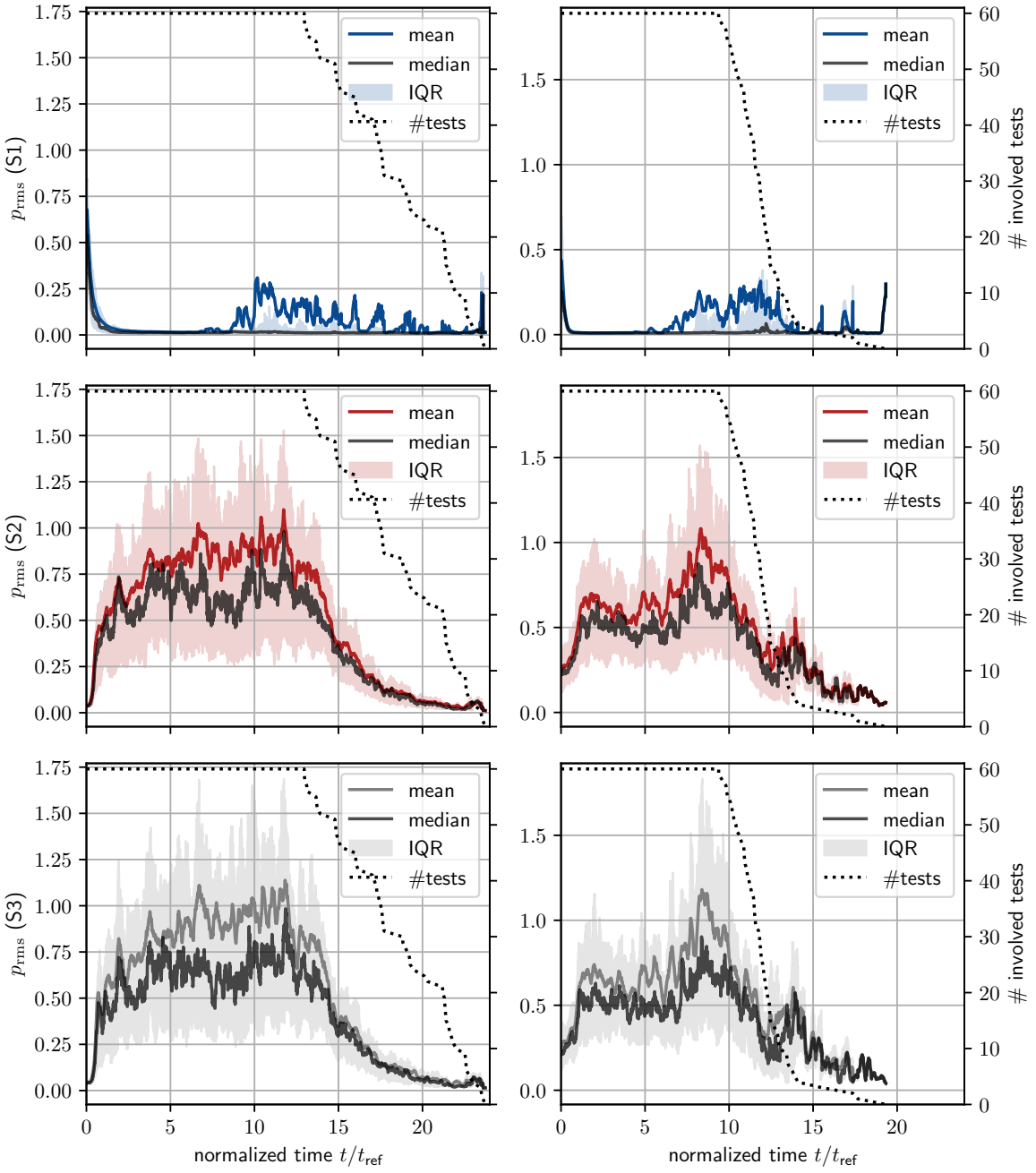

Figure 5.4: Water, cluster 1: Noise over time for the first (left column) and second (right column) cavitation valley, at sensors S1 (top), S2 (middle), S3 (bottom)

least noisy ones and since the other valleys are no longer contributing to the distribution, the overall intensity decreases.

In cluster 1 the first increase around $t/t_{\text{ref}} = 1$ is present as well but it is only followed by small peaks around $t/t_{\text{ref}} = 2$ and shortly before $t/t_{\text{ref}} = 4$. The overall noise intensity is lower than in cluster 0. But it stays more or less constant until $t/t_{\text{ref}} = 12$. Then it decreases. Again, this decrease coincides with the drop in number of involved tests.

From theory, the expectation would be that the noise starts to increase in S2 earlier than in S3. But due to the small distance between both sensors, the delay is so small that this method is not suitable for a reliable conclusion. This question would have to be investigated individually per test.

Unlike in nitrogen, the behavior in the second cavitation valley is very similar to the first one. The main differences are the following: In cluster 0 a peak in S1 at $t/t_{\text{ref}} = 5$ is visible, but note that at this point the number of tests is already halved. The step-wise increase in S2 and S3 is not visible in the second valley. And the noise intensity at $t/t_{\text{ref}} = 0$ is higher than in the first valley.

5.1.2 Frequency dependence

So far, only the complete frequency range from 1 to 30 kHz was considered. It should be investigated, if the noise in different frequency ranges behaves differently over time. Therefore the procedure above is repeated for different frequency ranges. Each frequency range covers 1 kHz. Starting with the frequency band 1-2 kHz, the range is shifted in steps of 100 Hz up to 29-30 kHz. Due to the reasons mentioned above, only the median of the RMS is considered in the following. However, only the general shape of the median over time is of interest. In the next steps the high-frequency changes of the median would be obstructive. Therefore the moving average with a filter size of 10 % of t_{ref} is used to smooth the course over time.

That leads to 281 courses of the RMS-median over time, each corresponding to a certain frequency range. These are plotted as colorplots, which are basically spectrograms but with absolute values matching to the previous consideration of the complete frequency band.

Observations: LN_2

The results for class 0 and 1 in LN_2 are shown in Fig. 5.5 and Fig. 5.6 for the first two cavitation valleys. Regarding class 0, it can be seen that the low frequency noise is much more effected by the initial transient and the peak around $t/t_{\text{ref}} = 2$ than the high frequency noise. The peaks around $t/t_{\text{ref}} = 4$ and the increase at $t/t_{\text{ref}} = 5$ in S1 are also much more pronounced in the low-frequency region. The same is true for the fluctuations in S2 and S3.

In class 1 it can be seen as well that during the initial transient the low-frequencies are effected the most. Afterwards, the low frequencies are especially present around shortly after $t/t_{\text{ref}} = 2$ and around $t/t_{\text{ref}} = 4$. The range around $t/t_{\text{ref}} = 3$ is slightly less pronounced. High frequencies have peaks at those three points as well but in varying intensity. In the mid-frequency range around 15 kHz the third peak seems to be especially pronounced, while in the high-frequencies above but especially at 25 kHz the first and second peak are pronounced the strongest. Another peak that was not easily visible in the previous consideration is present at $t/t_{\text{ref}} = 6$ for frequencies below 15 kHz, however, there are only few tests involved.

In S2 it seems like the two peaks at $t/t_{\text{ref}} = 2.5$ and $t/t_{\text{ref}} = 3.5$ are equally pronounced at low frequencies but at higher frequencies the second peak seems slightly less prominent. It is further noticeable that low frequencies below 10 kHz start to rise much earlier than higher frequencies. The frequency range around 25 kHz seems to have its maximum even later, while the RMS in the other frequency ranges has already dropped again.

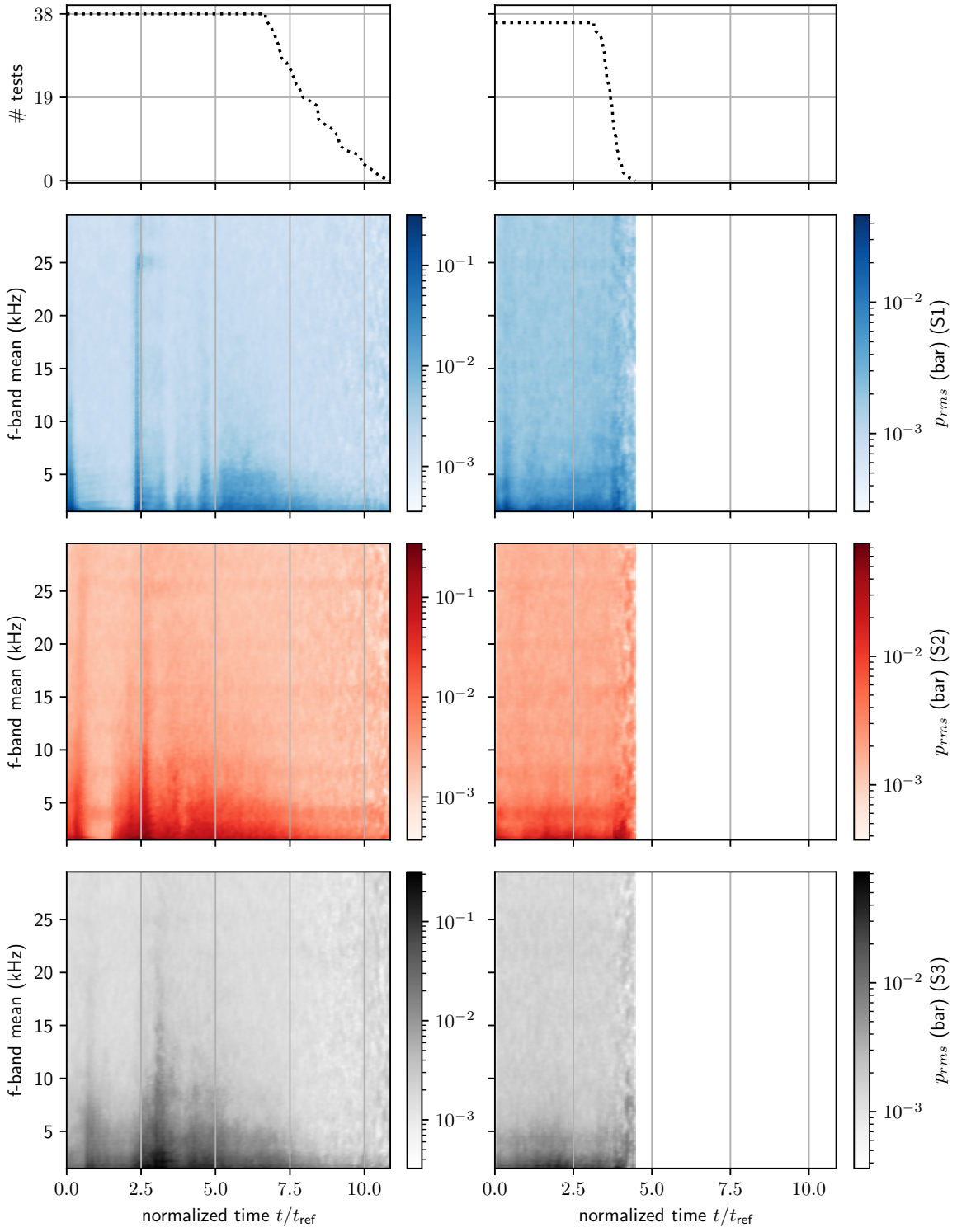

Figure 5.5: LN_2, cluster 0: Frequency dependent noise over time for the first (left column) and second (right column) cavitation valley, at sensors S1 (top), S2 (middle), S3 (bottom)

In S3 the main differences in the behavior over time are an early rise in the very low frequencies around 5 kHz around $t/t_{\text{ref}} = 1$ and a more prominent one over a larger frequency range up to 20 kHz around $t/t_{\text{ref}} = 5$. Again, the frequency range around 25 kHz stands out.

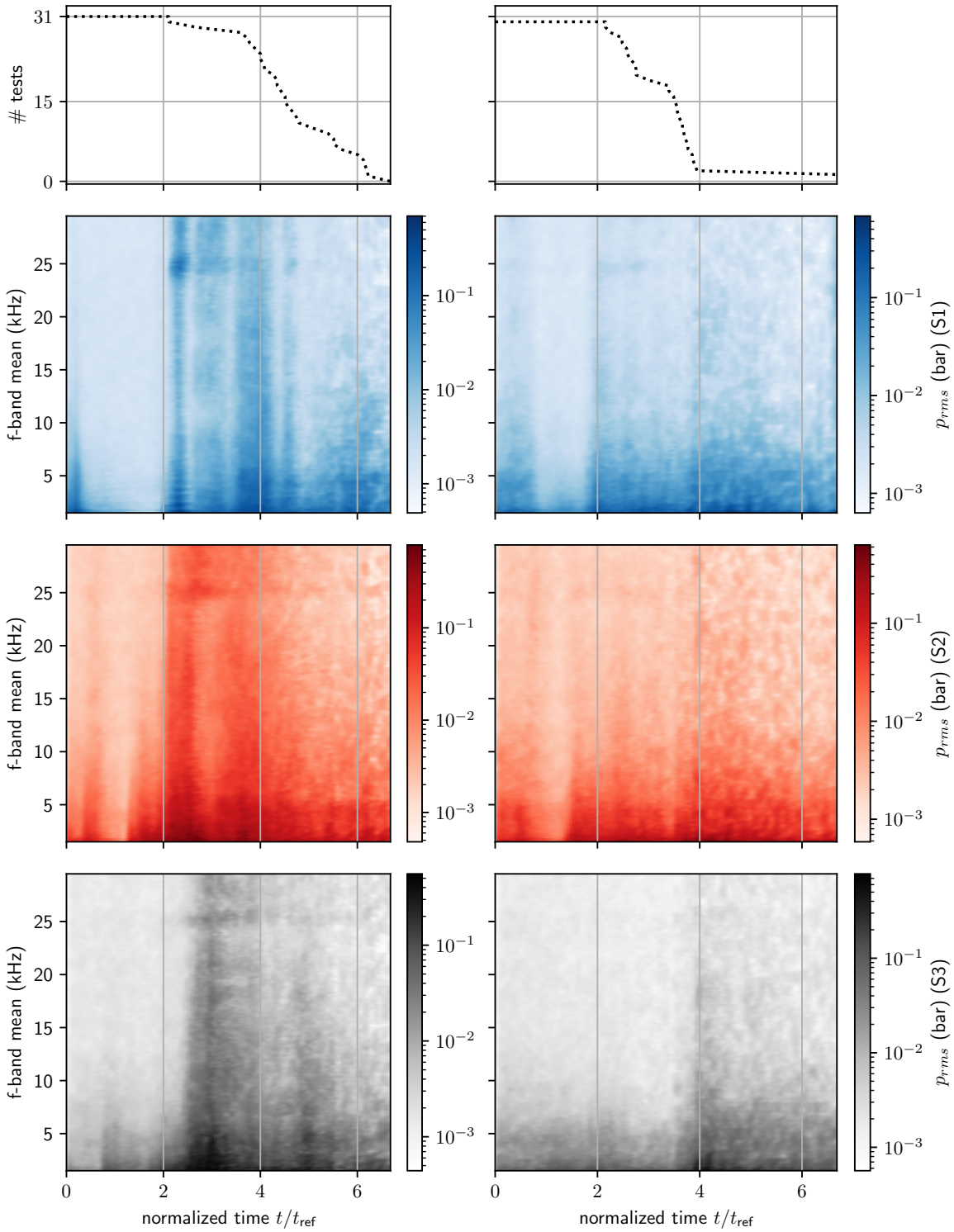

Figure 5.6: LN_2, cluster 1: Frequency dependent noise over time for the first (left column) and second (right column) cavitation valley, at sensors S1 (top), S2 (middle), S3 (bottom)

The second valleys in clusters 0 and 1 are not very informative. Low frequencies are more pronounced in general, but changes over time seem to occur relatively synchronously in the different frequency regions. See Fig. A.14 to Fig. A.16 for the results of the other clusters.

Observations: water

The results for class 0 and 1 in water are shown in Fig. 5.7 and Fig. 5.8 for the first two cavitation valleys. These results are not very informative compared to the LN_2 results.

Most interesting is the initial oscillation in S1 which mainly consists of a frequency close to 5 kHz but with multiple overtones. This frequency is rising by roughly 2 kHz in a time of $t/t_{\text{ref}} = 5$.

Interestingly, even though the median is used for this analysis, peaks in S1 are more visible than when considering the whole frequency range from 1 to 30 kHz. Especially the increase, mainly of high-frequency noise, towards $t/t_{\text{ref}} = 10$ in cluster 1 deviates from this global consideration (compare Fig. 5.4).

At positions S2 and S3 no significant differences between frequency ranges are detectable apart from the general difference in intensity between low and high frequencies.

5.1.3 Discussion

From these results one can see the great differences between the noise characteristics in water and liquid nitrogen. In water the noise in the liquid phase (S2, S3) seems to be independent from what is assumed to be the cavitation region (S1) at first glance. The noise sets on as the tension wave passes. In LN_2 in contrast it is evident that the noise behavior is strongly coupled between the different regions in the pipe. A similar pattern is observed at the different sensor positions, shifted in time, which would suggest propagation of the noise through the fluid. However, the propagation doesn't seem to be trivial and unidirectional. While in water the noise seems to be random over time, a periodicity can be seen in LN_2.

Multiple questions arise, some of which will be investigated in the following part of the chapter: The nature of the peaks that cause a relatively high mean and IQR in water at S1 is unclear yet, as they seem to appear randomly. As mentioned before, no coupling between (S2,S3) and S1 is obvious from the previous observations. But only for complete column separation such a decoupling would be imaginable. In this case, however, no such peaks in the vapour region would be expected. The results in LN_2 partially fit to the theory of a main pressure wave travelling between the tank and the cavitation. It should be investigated in more depth how well the pressure readings fit to this theory. The propagation of the noise related to the first characteristic peak in LN_2 is not obvious and should be further investigated. Another unclear phenomenon is the step-wise increase in noise intensity in water at S2 and S3. Especially for the step at $2 \cdot t_{\text{ref}}$ no explanation is obvious to the author. However, this aspect won't be covered in this thesis.

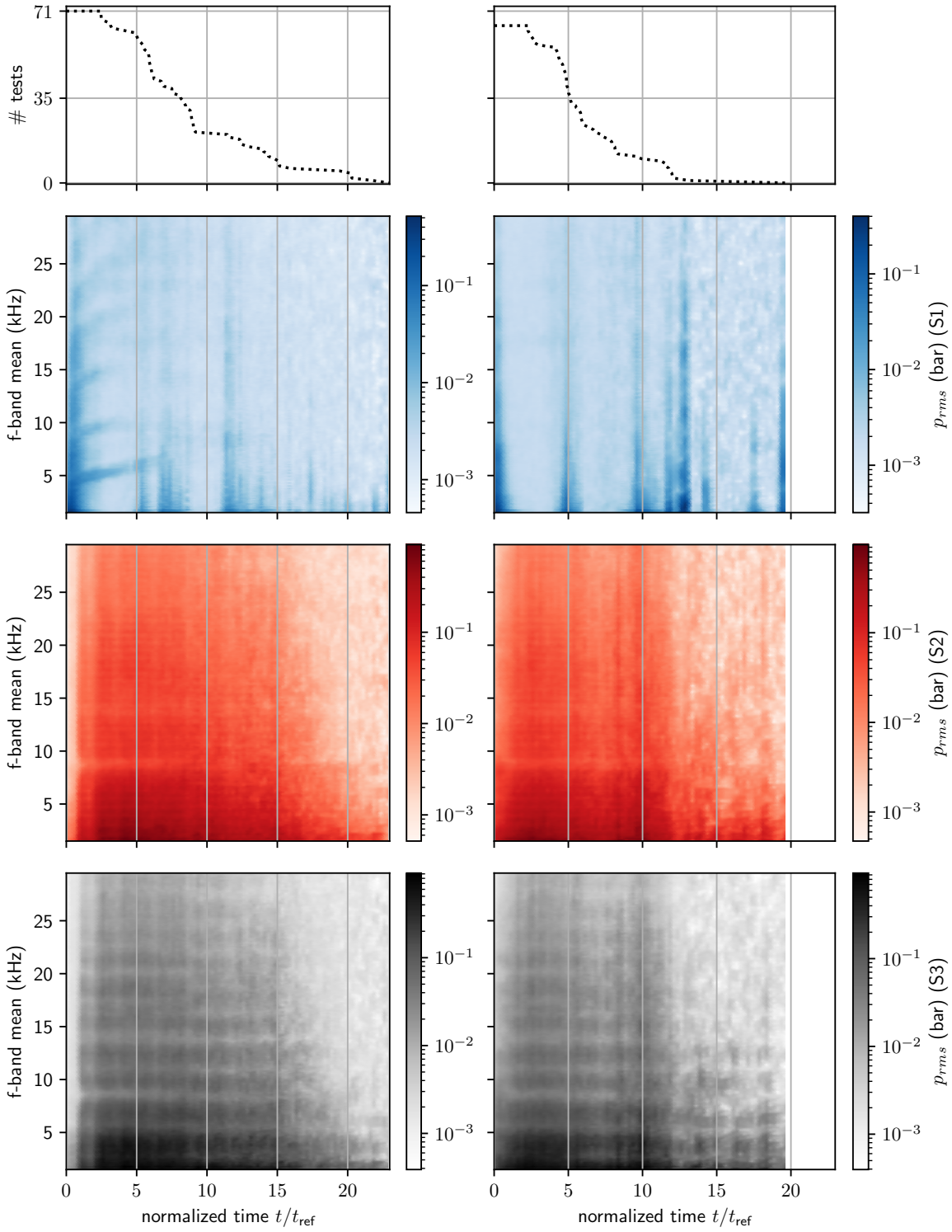

Figure 5.7: Water, cluster 0: Frequency dependent noise over time for the first (left column) and second (right column) cavitation valley, at sensors S1 (top), S2 (middle), S3 (bottom)

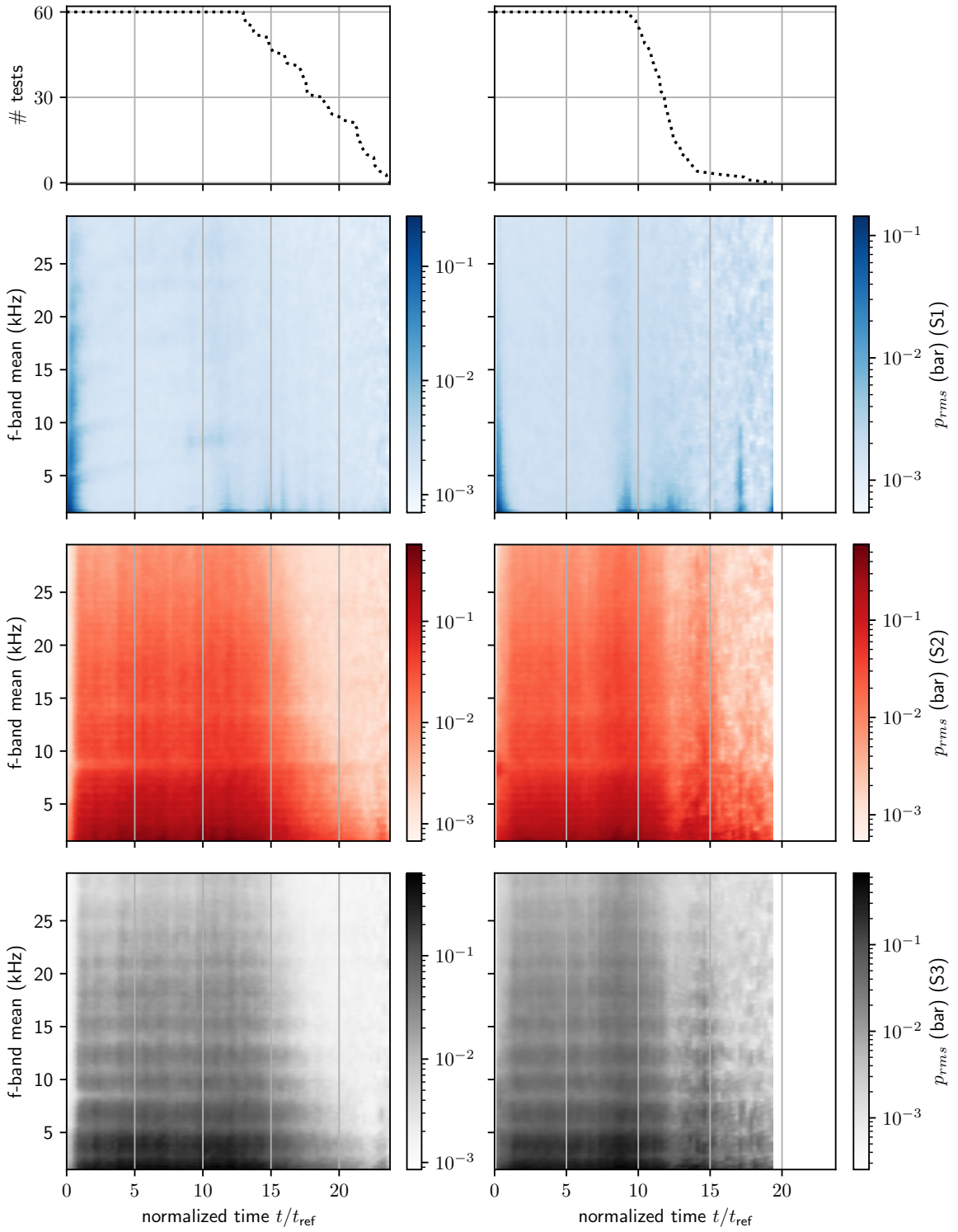

Figure 5.8: Water, cluster 1: Frequency dependent noise over time for the first (left column) and second (right column) cavitation valley, at sensors S1 (top), S2 (middle), S3 (bottom)

5.2 Pressure Peak Analysis

Peaks in the pressure readings were observed previously and raised various questions, which shall be explored in the following.

5.2.1 Water

A dominant feature in the water tests is the presence of strong, short duration pressure peaks in S1 during the cavitation phase as mentioned in the previous section. Traudt et al. [26] supposed that those peaks originate from the primary water-hammer wave and explained the anomalous timing with an extremely slowed down wave propagation speed due to the multiphase conditions.

It is apparent that at positions S2 and S3 also many short duration peaks are measured. Those peaks are more frequent than in S1. See the example plotted in Fig. 5.9. The primary water-hammer wave is not expected to manifest itself as short pressure peaks within the liquid column but rather as a rise in pressure that lasts until the reflected wave passes the sensor position again. Therefore the hypothesis is made that the peaks originate from the collapse of cavitation bubbles. In this case, the collapse might be caused by the primary waves, but the actually measured pressure peaks do not display this pressure wave and might therefore be delayed in time.

To test this hypothesis, an analysis method is proposed which tries to interrelate the peaks measured at the different sensors. The delays between those peaks might provide insight into the mechanism causing the peaks.

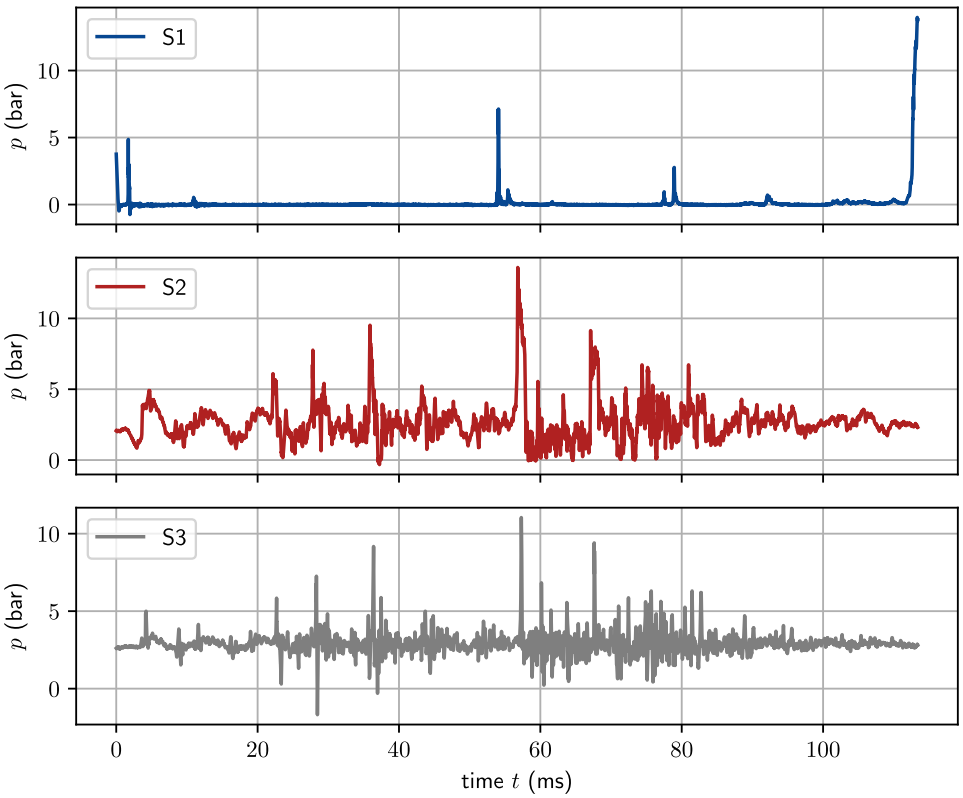

Figure 5.9: Examples of peaks in different sensors

5.2.1.1 The method

The basic principle of this method is to consider all possible combinations of peaks between the three sensors, that could possibly originate from the same source. The assumption is made that there is no cavitation between sensors S2 and S3 and that the wave propagation speed is therefore constant and equals the speed of sound of the liquid phase. By theory the cavitation is mainly accumulated at the valve [3]. The sensors S2 and S3 are positioned close to the tank and are close to each other, reducing the chance of cavitation in this area. The assumption is further justified by the observations in [26] that no cavitation was observed in an optical access between sensors S2 and S3. This information can be used to filter only those peak combinations for which a propagation from S2 to S3 or in the opposite direction is observed. This will be described later in more detail. All other peaks are considered in the beginning, to assure an unbiased approach. There is no physical justification for narrowing down the range around the S1-peaks in which potentially linked S2- and S3-peaks are searched, since it cannot be assumed at this point, that the wave propagation speed along the whole pipe is known. Physical considerations will be made later to filter out combinations that are not possible. Still, this approach will inevitably consider many combinations that do not actually have a common source. The delays between the peaks in those combinations will be randomly distributed. The idea behind this method is that the physical mechanisms that actually occur cause an accumulation of certain delays that deviate from the random distribution.

Peak Detection

The first step of this analysis is the detection of the peaks. This is done via a prominence condition as in section 4.2.1. One common threshold prominence δ_{th} is used for the peak detection in all sensors, which is independent from the one in section 4.2.1. The choice of this parameter will be discussed in section 5.2.1.3. The peaks are referred to as $\Lambda_{S1,i}, \Lambda_{S2,j}$ and $\Lambda_{S3,k}$ in the following, with i, j, k being counter variables.

For the S1-signal the l_{io} value from chapter 4.2.1 is used. Peaks that lie within the initial oscillation phase are excluded, since this oscillation is not found in the other two sensors and does not correspond to the sharp pressure peaks that shall be investigated here. Since the highest peaks sometimes have non-monotonous edges, peaks might be detected on the edge. Therefore it has been shown to be advisable to keep only those peaks that are the highest point within a range of $\pm N_{S1}$ samples.

Peak Combinations

Since the aim of this analysis is to investigate combinations $C\left(\Lambda_{S1,i}, \Lambda_{S2,j}, \Lambda_{S3,k}\right)$ of peaks which can potentially originate from the same source and propagate through the pipe, the peaks detected in S2 and S3 can be reduced by a simple consideration: As mentioned before, it can be assumed that there is no cavitation between S2 and S3 so the propagation speed a_{23} is known and constant. It should be noted, that the drop in pressure can cause previously dissolved gas to come out of solution, which alters the speed of sound. The pressure spikes considered here, however, are of relatively large amplitude ($>$ 1bar). Therefore they do not represent acoustical perturbations and their propagation speed is not affected in the same

way. Since the distance between S2 and S3 is short, the possibility of peaks being radiated from a source between S2 and S3 is neglected. If the above mentioned hypothesis is true, this assumption is valid since no cavitation is expected in this range. Otherwise the impact of this assumption is relatively small as it only concerns $\approx 9\%$ of the pipe.

With these considerations it becomes clear, that only those $(\Lambda_{S2,j}, \Lambda_{S3,k})$ need to be considered, that have a delay corresponding to the wave travel time between S2 and S3. A delay matrix $\mathcal{D}_{23}$ is calculated with

$$(\mathcal{D}_{23})_{j,k} = t_{(\Lambda_{S2,j})} - t_{(\Lambda_{S3,k})}, \tag{5.2}$$

with the timestamps t of the individual peaks. This matrix contains an entry for every combination of $\Lambda_{S2,j}$ and $\Lambda_{S3,k}$. A positive delay consequently corresponds to a propagation from the tank towards the valve and vice versa. For the entries in this matrix, the following condition must be satisfied:

$$\begin{gathered} \frac{\Delta x_{23}}{a_0 \cdot (1+\eta^+)} \leq (\mathcal{D}_{23})_{j,k} \leq \frac{\Delta x_{23}}{a_0 \cdot (1-\eta^-)} \\ \text{or} \\ -\frac{\Delta x_{23}}{a_0 \cdot (1-\eta^-)} \leq (\mathcal{D}_{23})_{j,k} \leq -\frac{\Delta x_{23}}{a_0 \cdot (1+\eta^+)} \end{gathered} \tag{5.3}$$

Here, Δx_{23} is the distance between sensors S2 and S3, a_0 is the speed of sound obtained from the measured temperature $T_{S1,0}$ and pressure data $p_{hp,0}$ at the time just before valve closure. Since these measurements can deviate slightly from reality, a tolerance $\eta^{+/-}$ is introduced with $0 \leq \eta^{+/-} < 1$. The choice of $\eta^{+/-}$ will be discussed in section 5.2.1.3.

All peak combinations $(C_{23})_{j,k}$ for which $(\mathcal{D}_{23})_{j,k}$ does not satisfy these conditions, are discarded. An exemplary S2-S3 delay matrix for a single test is shown in Fig. 5.10. Discarded combinations are greyed out.

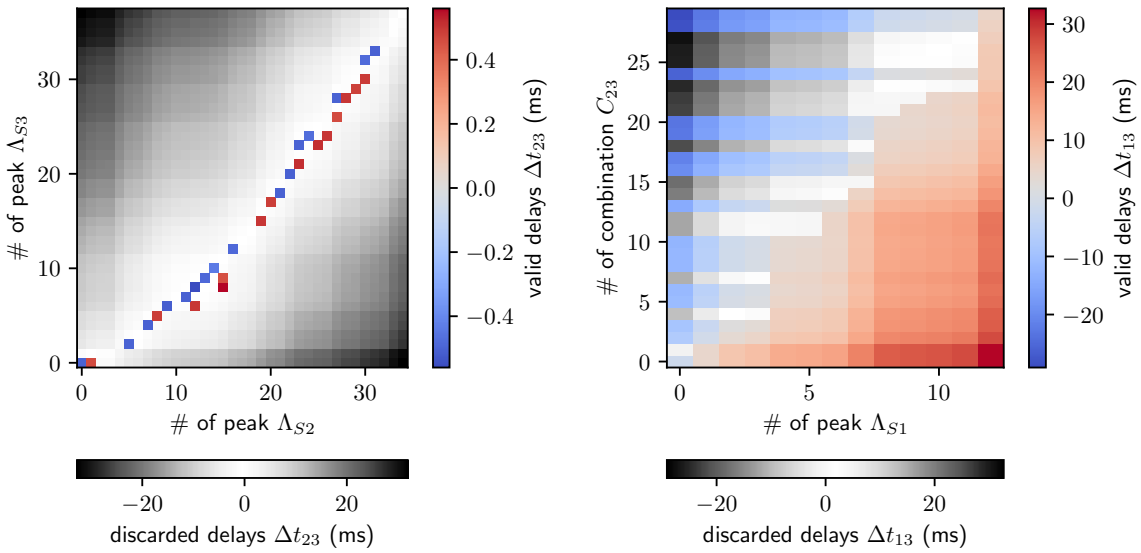

Figure 5.10: Examples of delay matrices, visualization of selection. Left: S2-S3-delays, right: S1-S3-delays

Let $\mathcal{C}_{23}$ be the set of remaining combinations $(C_{23})_{j',k'}$, for which from now on the notation $(C_{23})_{j',k'} = (C_{23})_h$ is used, where h is any combination of the remaining j' and k'. Then a delay matrix $\mathcal{D}_{13}$ can be created with

$$(\mathcal{D}_{13})_{i,h} = t_{(\Lambda_{S1,i})} - t_{(\Lambda_{S3,h})} \tag{5.4}$$

for all combinations $(C_{123})_{i,h}$ of all peaks $\Lambda_{S1,i}$ with all combinations $(C_{23})_h$. $\Lambda_{S3,h}$ is the S3-peak from the combination $(C_{23})_h$.

For some of those combinations it can be shown, that they are physically impossible. For that consider the following cases:

- **The source of the peaks is located between valve and S1:** In this case the peak will first appear in the S1-reading, then in the S2-reading and lastly in the S3-reading $\left(t_{(\Lambda_{S1})} < t_{(\Lambda_{S2})} < t_{(\Lambda_{S3})}\right)$.
- **The source is located between S1 and S2:** In this case multiple scenarios are possible:
  - $\boldsymbol{t_{(\Lambda_{S1})} < t_{(\Lambda_{S2})} < t_{(\Lambda_{S3})}}$
  - $\boldsymbol{t_{(\Lambda_{S2})} < t_{(\Lambda_{S1})} < t_{(\Lambda_{S3})}}$
  - $\boldsymbol{t_{(\Lambda_{S2})} < t_{(\Lambda_{S3})} < t_{(\Lambda_{S1})}}$
- **The source is located between S3 and the tank or in the tank:** In this case the order in time of the three peaks has to be $t_{(\Lambda_{S3})} < t_{(\Lambda_{S2})} < t_{(\Lambda_{S1})}$, with the condition that $\Delta t_{13} \geq \frac{\Delta x_{13}}{a_0 \cdot (1+\eta^+)}$, since the wave propagation might be lowered by the cavitation but it cannot be increased. The wave travel speed between S2 and S1 cannot be higher than between S3 and S2.

Those cases are visualized in Fig. 5.11 (only the relevant part of the propagation path is shown here). This leads to the finding, that the following combinations are impossible:

- $\boldsymbol{t_{(\Lambda_{S1})} < t_{(\Lambda_{S3})} < t_{(\Lambda_{S2})}}$, since that would mean, that the wave would skip S2 while traveling from S1 to S3,
- $\boldsymbol{t_{(\Lambda_{S3})} < t_{(\Lambda_{S2})} \wedge t_{(\Lambda_{S3})} < t_{(\Lambda_{S1})} \wedge \Delta t_{13} < \frac{\Delta x_{13}}{a_0 \cdot (1+\eta^+)}}$, since that would mean that the wave would speed up between S2 and S1.

An exemplary S1-S3 delay matrix is shown in Fig. 5.10 with the invalid combinations blanked out.

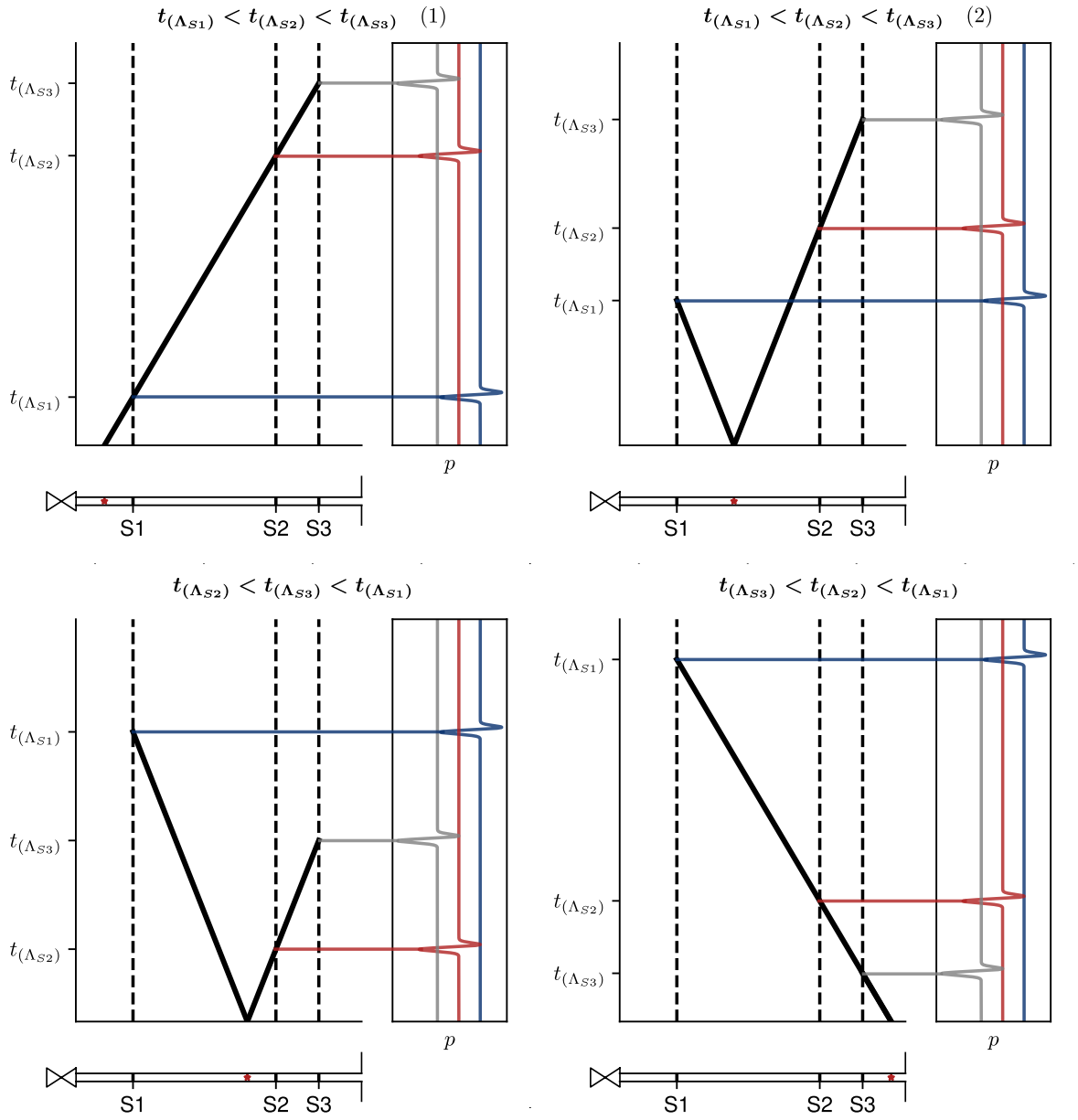

Figure 5.11: Visualization of the different possibilities for the source location

Weighting

Not all peaks found during peak detection are equally significant. In general it can be stated that peaks are especially significant if they have a high prominence and stand out strongly compared to the vicinity in the signal. As a measure for how strongly a peak stands out, the "uniqueness" u for a peak Λ from a signal $\underline{\boldsymbol{p}}$ is defined.

If the signal belongs to sensors S2 or S3, first the moving average $\underline{\boldsymbol{p}}_{\boldsymbol{avg}}$ of $\underline{\boldsymbol{p}}$ is calculated with a filter size N_{avg}. A corrected signal is calculated as $\underline{\boldsymbol{p}}' = \underline{\boldsymbol{p}} - \underline{\boldsymbol{p}}_{\boldsymbol{avg}}$. This is meant to correct for low-frequency fluctuations in the signals which would distort the significance. Consider a strong peak that stands out from its close neighborhood but the whole region lies well below the average value due to low-frequency drop in pressure. Since in a next step the standard deviation will be used, as a threshold, this strong peak would not stand out anymore. This

situation is visualized in Fig. 5.12 with the peak at 45.6 ms. In the bottom plot only the mean of the whole signal is subtracted instead of the moving average.

For the S1-signal, this is not useful, since low frequency fluctuations are less common and the signal is mostly at a steady level only with upwards peaks. Instead, the corrected pressure is here obtained by $\underline{\boldsymbol{p}}' = \underline{\boldsymbol{p}} - p_{\mathrm{ref}}$ using the reference pressure defined in chapter 4.2.1.

From the corrected signal the moving standard deviation $\underline{\boldsymbol{\sigma}}$ is calculated with a filter size N_σ. Now the distance of Λ to the moving standard deviation is evaluated, while leaving the possibility to scale the moving standard deviation by ε, since there is no physical reasoning for $\underline{\boldsymbol{\sigma}}$ as a threshold and the influence of this choice needs to be considered in a sensitivity analysis at a later point:

$$d(\Lambda) = \left(\underline{\boldsymbol{p}}'\right)_\Lambda - \varepsilon \left(\underline{\boldsymbol{\sigma}}\right)_\Lambda . \tag{5.5}$$

Intuitively, d looses its comparative meaning at high values. On the other hand, peaks with negative d have a very poor significance and can be discarded. Therefore d is wrapped in a scaling function to obtain u:

$$u(\Lambda) = \begin{cases} 0, & d(\Lambda) < 0 \\ \frac{d(\Lambda)}{d_{max}}, & 0 \leq d(\Lambda) \leq d_{max} \\ 1, & d(\Lambda) > d_{max}. \end{cases} \tag{5.6}$$

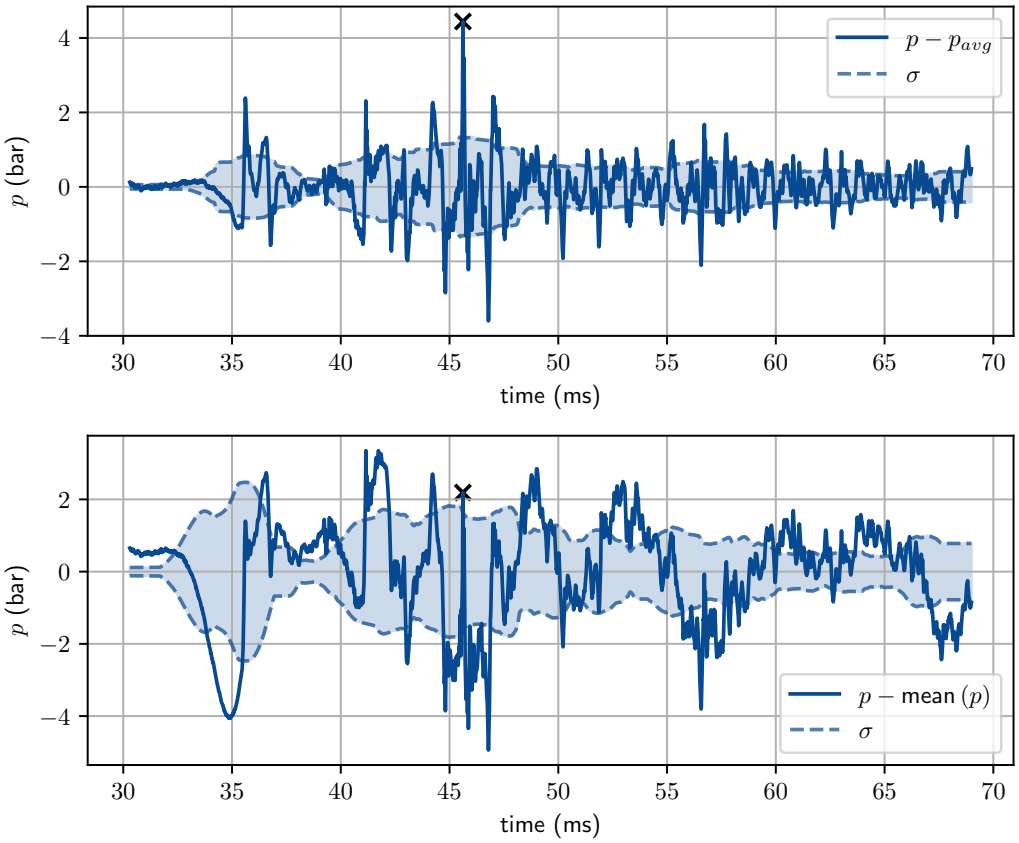

Figure 5.12: Demonstration of uniqueness. Top: moving average subtracted, bottom: simple mean subtracted

Based on the uniqueness u and prominence δ of each associated peak a weight can be assigned to each combination $(C_{123})_{i,h}$, resulting in a weight matrix $\mathcal{W}_{123}$ with

$$(\mathcal{W}_{123})_{i,h} = f_w\Big(u\left(\Lambda_{S1,i}\right), u\left(\Lambda_{S2,h}\right), u\left(\Lambda_{S3,h}\right), \delta\left(\Lambda_{S1,i}\right), \delta\left(\Lambda_{S2,h}\right), \delta\left(\Lambda_{S3,h}\right)\Big). \tag{5.7}$$

Later it will be seen that an additional feature should be included in the weight function. Many formulations for $f_w(...)$ are conceivable and there is no single *right* definition. However, it is necessary to evaluate how the conclusion of this method is influenced by the choice of the weight function. This will be considered in section 5.2.1.3.

5.2.1.2 Preliminary results

For a preliminary consideration some initial values for the parameters used above need to be chosen.

Prominence threshold δ_{th}: Inspection of a large portion of tests showed that a threshold of $\delta_{th} = 1\text{bar}$ is an appropriate choice which includes peaks that seem to be important while excluding obviously unimportant ones.

Range around S1-peaks N_{S1}: It makes sense to choose a value which corresponds to the typical width of the corresponding peaks at their base. This peak width lies in the range of 0.5 ms, so that $N_{S1} = 40$ samples is an appropriate choice.

Tolerances for speed of sound η^-, η^+: The measurement errors of pressure and temperature alone, stated in chapter 3, would suggest that a tolerance of $\pm 0.6\%$ is sufficient. However, a_0 was calculated from the initial conditions and might therefore be altered at the time of consideration. Moreover the width of the peaks introduces an additional error. As a reference of how strongly a deviates from the theoretical a_0 the delay between the rising and falling edges of the first water hammer peak were considered. A rough estimation showed deviations of up to 20%. That was therefore used as an initial value.

Moving average filter size N_{avg}: Since the subtraction of the moving average is used to reduce the effect of low frequency fluctuations, it is reasonable to choose the filter size according to the expected period of those fluctuations. It was observed that the fluctuations fit to twice the wave travel time between S2 and the tank. Therefore $N_{avg} = 187$ samples is used.

Moving standard deviation filter size N_σ: This filter size defines the width of the neighborhood that influences the significance of the peaks. The choice of this parameter is empirical. It was found that $N_\sigma = 413$ samples leads to reasonable results, which corresponds to half the wave travel time between valve and tank.

Scaling ε: This parameter shifts the lower threshold within the uniqueness function. At this point there is no reason for adjustment, so it can be set to $\varepsilon = 1$, so that the threshold is solely determined by σ.

Range for uniqueness scaling function d_{max}: Considering that the standard deviation usually lies well below 2 bar, a peak that exceeds σ by 1 bar can be considered a strong outlier. Therefore $d_{max} = 1$ bar is chosen.

Weight function $f_w(...)$: Here a simple formulation is chosen that treats the S2- and S3-peak as a pair and therefore only takes into account the minimum prominence δ and uniqueness u from both peaks:

$$f_w = u(\Lambda_{S1}) \cdot \min\left[u(\Lambda_{S2}), u(\Lambda_{S3})\right] \cdot \Big(\delta(\Lambda_{S1}) + \min\left[\delta(\Lambda_{S2}), \delta(\Lambda_{S3})\right]\Big). \tag{5.8}$$

The procedure described in section 5.2.1.1 is executed for all tests individually. All peak combinations C_{123} are collected with their respective delays Δt_{13} and weights. A histogram can be created from those delays, weighted by the respective weight.

The histogram, resulting from the parameter choice described above, is depicted in Fig. 5.13. It consists of the entirety of detected peaks in all water tests. It is noticeable that delays around -5 ms stand out strongly. A wave that travels from the valve to the tank would be captured with a delay of -5.19 ms between S1 and S3. A second but much wider peak is apparent around +11 ms.

Due to the nature of this method, this distribution includes many combinations that share one or more common peaks. However, if the pressure peaks are travelling through the pipe, a single peak can in reality only be part of one combination. That means if a specific combination is assumed to be real, all coupled combinations would have to be discarded. The impact of this fact can be visualized as follows:

During the collection of combinations a specific delay $\Delta t'_{13}$ is selected which is assumed to be "the true" delay. That means, if an S1-peak is part of a combination with a delay $\Delta t_{13} = \Delta t'_{13}$, all other combinations including this S1-peak are discarded. If an S1-peak is part of more than one combination with this specified delay, the combination with the highest weight is kept. For S1-peaks with no combination with this delay, all combinations are kept. This can be done for all possible $\Delta t'_{13}$ which results in one histogram per selected $\Delta t'_{13}$. This collection of histograms is plotted in Fig. 5.13 on the right. Note that in this consideration only the coupling via S1-peaks is taken into account. Obviously, peak combinations can be coupled via S2- or S3-peaks as well. The results can be interpreted as follows:

It is expected, that this procedure reduces the weighted frequency for all delays, even for $\Delta t'_{13}$. The frequency for $\Delta t'_{13}$ however will be reduced less. The more the selection of a specific $\Delta t'_{13}$ reduces the overall frequencies, the more the corresponding combinations are coupled to others and the more likely it is that the frequency of this delay is overestimated. It can be seen that delays shortly above 0 ms are highly coupled. Picking one of those reduces the frequency of the others almost to zero.

This demonstrates the need of an additional penalization in the weight function considering the coupling.

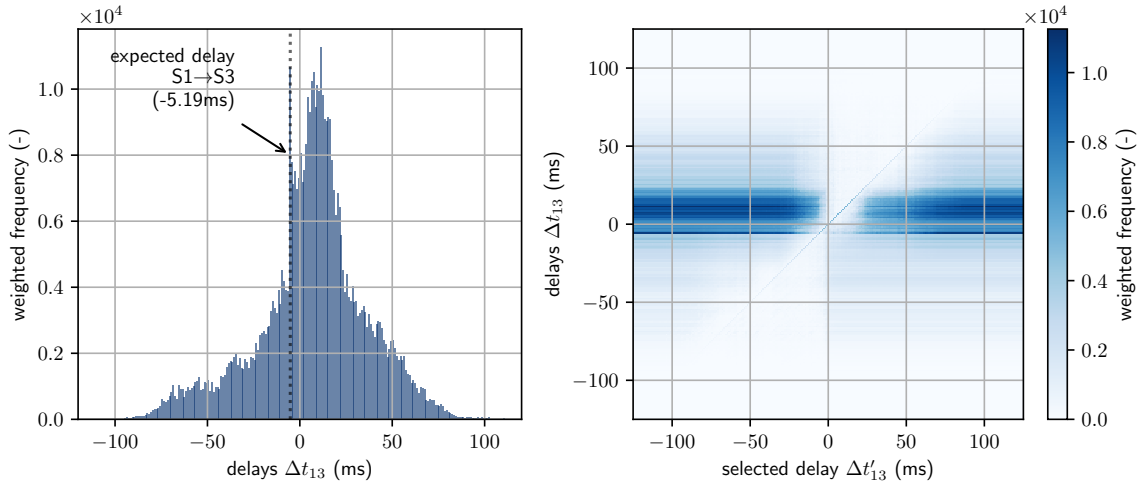

Figure 5.13: Preliminary results. Left: weighted delay histogram, right: cross-dependence via S1

5.2.1.3 Sensitivity Analysis

As stated before, the parameter choices are often empirical. There is no right choice of those parameters but it is important to know how the choice influences the result. Therefore a sensitivity study is performed for all of those parameters.

Weight function

The formulation of the weight function is also considered as such a parameter. As stated before, the coupling between different peak combinations is advisable. Two high-level versions of the weight functions are defined, which incorporate the function $f_w(...)$. The first one does not include the coupling and is simply

$$w_s\left((C_{123})_{i,j,k}\right) = f_w\left((C_{123})_{i,j,k}\right). \tag{5.9}$$

For the second one the set $\mathcal{C}_{\leftrightarrow,i,j,k}$ of all combinations C_{123} coupled with $(C_{123})_{i,j,k}$ needs to be determined. This set is visualized in Fig. 5.14, where each combination is represented by a cube and the blue colored cubes are the combinations from $\mathcal{C}_{\leftrightarrow,i,j,k}$ for $(C_{123})_{i,j,k}$, which is colored red.

Now the wrapping function is defined as

$$w_l\left((C_{123})_{i,j,k}\right) = \frac{f_w\left((C_{123})_{i,j,k}\right)}{\sum\limits_{(C_{123})_l \in \mathcal{C}_{\leftrightarrow,i,j,k}} f_w\left((C_{123})_l\right)}. \tag{5.10}$$

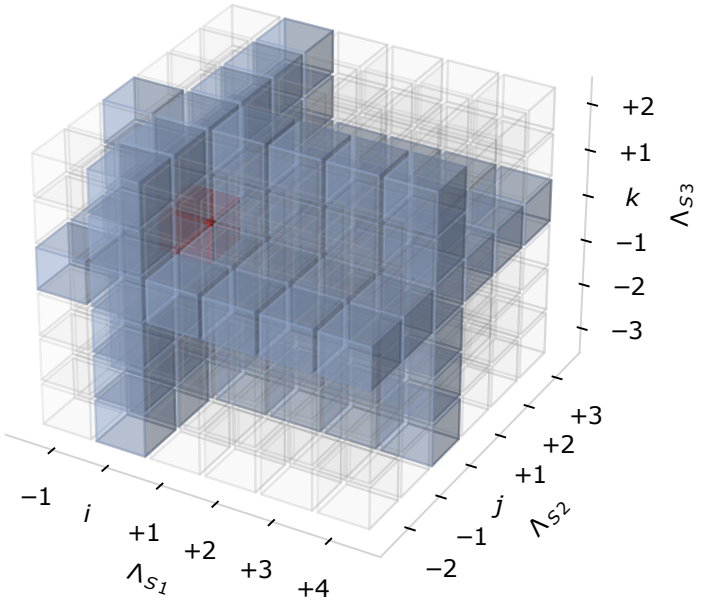

Figure 5.14: Visualization of the coupling between combinations

The following base functions are tried out (for the sake of clarity the notations $u(\Lambda_{S1}) = u_{S1}$ and $\delta(\Lambda_{S1}) = \delta_{S1}$ are used):

$$f_{w1}(C_{123}) = u_{S1} \cdot \min[u_{S2}, u_{S3}] \cdot (\delta_{S1} + \min[\delta_{S2}, \delta_{S3}]), \tag{5.11}$$

$$f_{w2}(C_{123}) = u_{S1} \cdot u_{S2} \cdot u_{S3} \cdot (\delta_{S1} + \delta_{S2} + \delta_{S3}), \tag{5.12}$$

$$f_{w3}(C_{123}) = \text{mean}[u_{S1}, u_{S2}, u_{S3}] \cdot \text{mean}[\delta_{S1}, \delta_{S2}, \delta_{S3}], \tag{5.13}$$

$$f_{w4}(C_{123}) = \min[u_{S1}, u_{S2}, u_{S3}] \cdot \min[\delta_{S1}, \delta_{S2}, \delta_{S3}], \tag{5.14}$$

$$f_{w5}(C_{123}) = u_{S1} \cdot u_{S2} \cdot u_{S3}, \tag{5.15}$$

$$f_{w6}(C_{123}) = u_{S1} \cdot \min[u_{S2}, u_{S3}], \tag{5.16}$$

$$f_{w7}(C_{123}) = \text{mean}[u_{S1}, u_{S2}, u_{S3}], \tag{5.17}$$

$$f_{w8}(C_{123}) = \min[u_{S1}, u_{S2}, u_{S3}] \tag{5.18}$$

and for reference:

$$f_{w0}(C_{123}) = 1. \tag{5.19}$$

For each definition f_{wx} the analysis is performed and the distribution is normalized by its maximum weighted frequency. This is done with both w_s and w_l as wrapping function. The other parameters are kept equal as chosen above. The results are shown in Fig. 5.15. Refer to A.22 for a closer look into the middle range of the distribution. It can be seen that the weight functions emphasize the peak at -5 ms. The steep edge is present in the reference case as well, but the peak is much less pronounced. Including the prominence (plotted in blue) in the weight function enhances this peak relative to the range around +5 ms. The qualitative conclusion would be the same for all f_w, but it is more obvious for f_{w1} and f_{w2}. Taking the coupling between combinations into account in contrast has a big effect. The range around

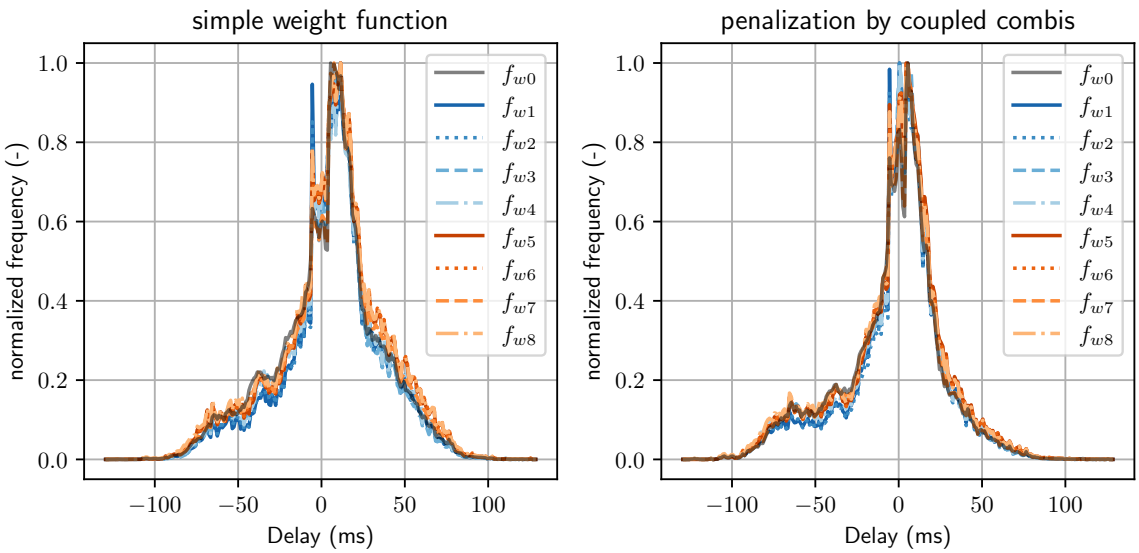

Figure 5.15: Sensitivity analysis: weight function

+11 ms is strongly attenuated, which was expected, considering the results seen in Fig. 5.13. Interestingly, a peak at +5 ms persists and an additional peak approximately at 0 ms arises.

Some of the remaining parameters are expected to have a strong cross influence as they influence the same aspect of the method. Those are

- the upper and lower tolerance for the speed of sound η^- and η^+,
- the window size for the moving standard deviation N_σ and the scaling factor ε and
- ε and the uniqueness scaling range d_{max}.

Obviously other pairs of parameters or even larger groups of parameters can have cross influences, but considering all those possibilities would be disproportionally complex since the goal of this study is only to estimate whether the choice of parameters changes the conclusion of the method.

To be able to evaluate the coupled influence of those parameters, a one-dimensional parameter is needed, describing the deviation of the distribution from a reference distribution. As reference the distribution resulting from the parameter choice described in section 5.2.1.2 is used but with the more elaborate weight wrapping function w_l. For the following sensitivity analysis the parameters that are not under investigation are set to these values. The deviation of a distribution F from the reference distribution F_{ref} is defined as the sum of the absolute differences, but with the sign of the sum of the raw differences. That way, differences do not cancel each other out, but information about whether F tends to be above or below F_{ref} is preserved:

$$\Delta F = \operatorname{sgn}\left(\sum (F - F_{\text{ref}})\right) \cdot \sum \operatorname{abs}(F - F_{\text{ref}})\,. \tag{5.20}$$

The distribution of ΔF over the two involved parameters can be used to find parameter ranges that seem to differ from each other. From those ranges single parameter combinations can be picked and the complete delay distribution can be evaluated.

Prominence threshold δ_{th}

The prominence threshold is investigated in a range from 0.5 bar to 3 bar. For each value the delay distribution is calculated and normalized. Those distributions are plotted as a color plot in Fig. 5.16. It can be seen that the peak at roughly +5 ms is only present for low thresholds. The peak around 0 ms is as well reduced for larger thresholds. The peak at -5 ms remains prominent for the whole considered range. Additionally, a higher thresholds leads to a more narrow distribution.

Range around S1-peaks N_{S1}

Ranges between $N_{S1} = 1$ and $N_{S1} = 100$ are considered. This parameter has a similar effect as the prominence threshold but less pronounced. The results can be found in Fig. 5.16.

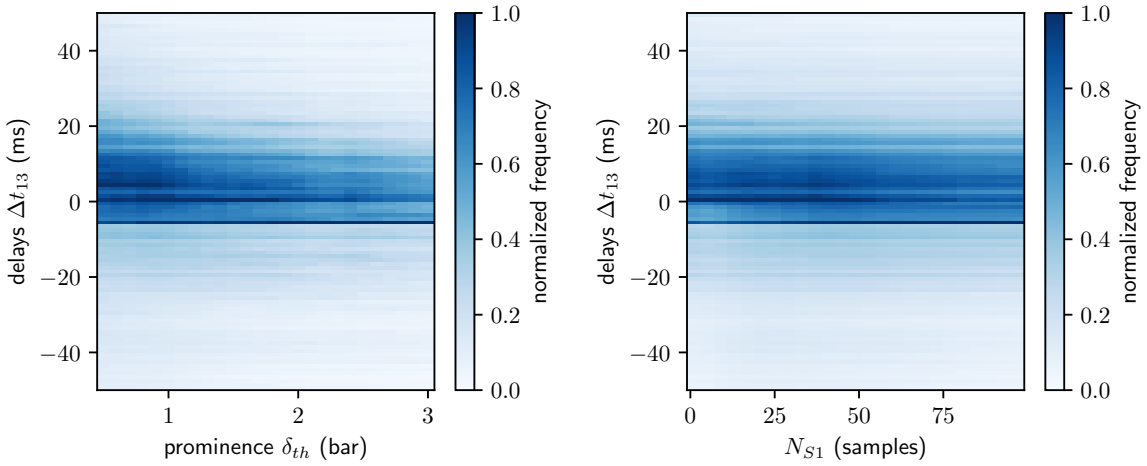

Figure 5.16: Sensitivity analysis: prominence threshold δ_{th} (left) and range around S1-peaks N_{S1} (right)

Speed of sound tolerances η^-, η^+

The tolerances are investigated in a range from 0.003 to 0.5, with increasing step size towards higher tolerances. The results are presented in Fig. 5.17. The peak at -5 ms seems to be prominent for a wide range of $\eta^- - \eta^+$ combinations and the distributions do not differ strongly. Large η^- and relatively small η^+ however lead to high values in the range of +5 to +10 ms, as can be seen in the enlarged plot in Fig. A.23. Very small tolerances lead to deviating results. Examples can be seen in Fig. A.23, which covers the parameter range within the hatched square in Fig. 5.17 on the left. However, combination 11 (shown in Fig. A.23) is the only one for which the peak at -5 ms is not significantly pronounced. At those small tolerances only very few combinations C_{23} are kept, so small changes in the tolerance can lead to massive differences since the impact of every single combination becomes great.

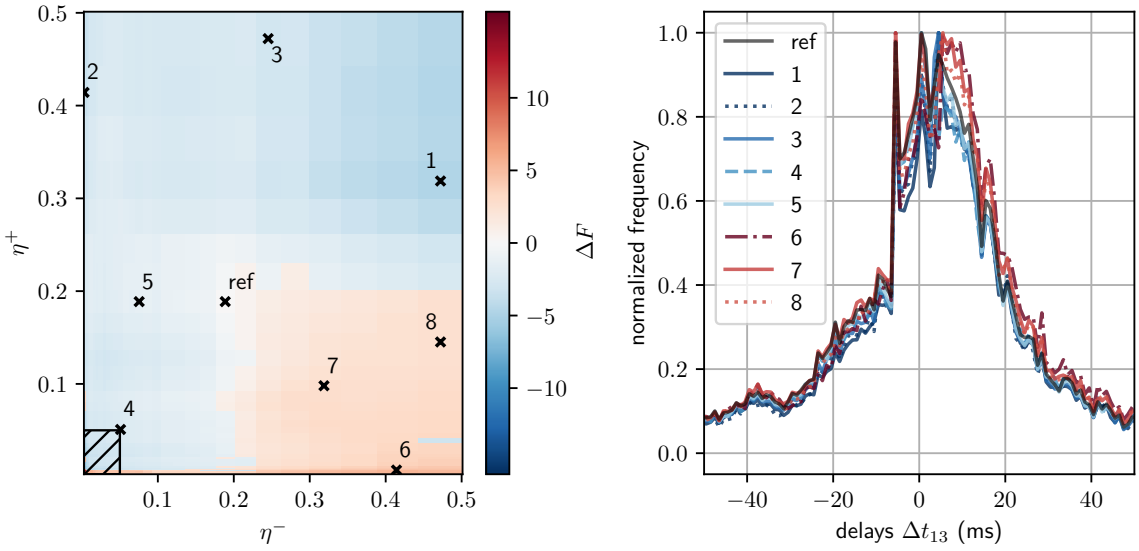

Figure 5.17: Sensitivity analysis: the speed of sound tolerances η^-, η^+. ΔF (left) and delay distributions for selected parameter combinations (right)

Moving standard deviation N_σ, ε

N_σ is investigated in a range between 53 and 773 samples. The scaling factor ε is varied within a range of 0.5 to 1.5. Qualitatively all combinations that were considered in detail showed a similar result. See Fig. 5.18 for an overview. Combination 3 deviates in that the peak at -5 ms is slightly less pronounced, combination 1 shows lower values around +5 ms.

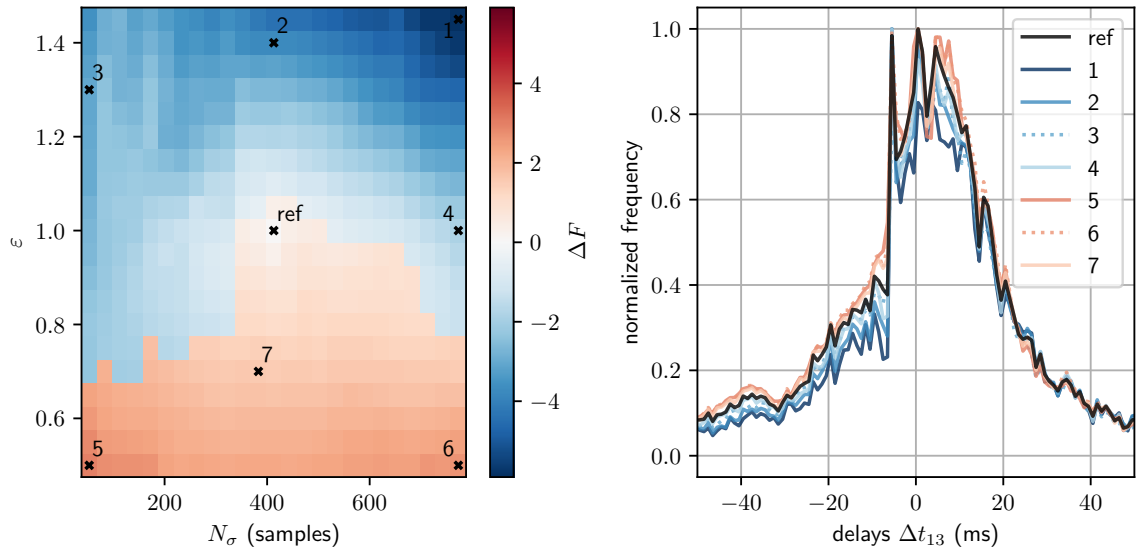

Figure 5.18: Sensitivity analysis: moving standard deviation filter width N_σ and scaling ε. ΔF (left) and delay distributions for selected parameter combinations (right)

Uniqueness scaling d_{max}, ε

The scaling range was tested for values between 0.5 and 3. The factor ε was tested in the same range above. The results can be seen in Fig. 5.19. Again, the peak around -5 ms is almost

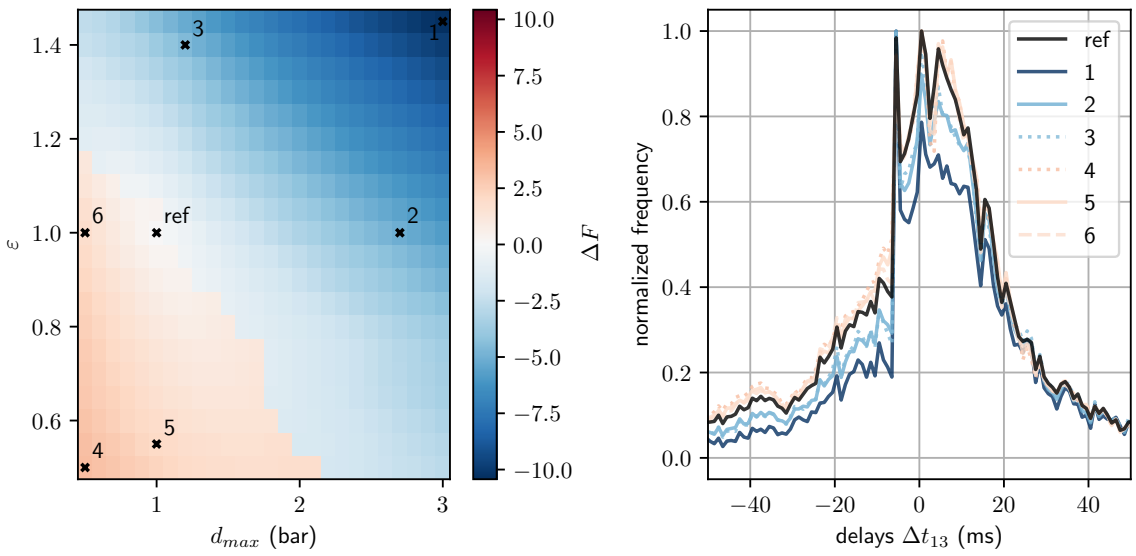

Figure 5.19: Sensitivity analysis: uniqueness scaling d_{max} and ε. ΔF (left) and delay distributions for selected parameter combinations (right)

unaffected by the parameter changes. The values around 0 ms and +5 ms are lowered by large values for d_{max} and even more so for combinations with additionally large ε.

Moving average filter width N_{avg}

The moving average is varied between $N_{avg} = 61$ and $N_{avg} = 781$. As can be seen in Fig. 5.20, the influence of the filter width is very weak. The peak at +5 ms seems to gain in prominence slightly with high filter sizes, while the peak at -5 ms is lowered marginally.

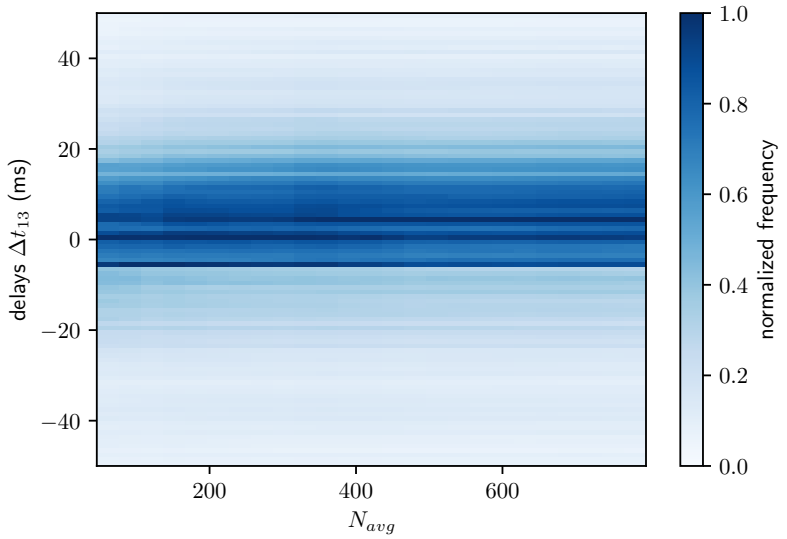

Figure 5.20: Sensitivity analysis: moving average filter width N_{avg}

It has become apparent, that the qualitative result is relatively stable regarding the free parameters. Especially the peak at -5 ms is very prominent in almost all distributions considered before. The ratio between this peak and the values at delays around +5 to +10 ms varies between the parameter choices. The values for those positive delays are often reduced by parameters that reduce the impact of low-amplitude peaks (like d_{max} and δ_{th}).

Based on this findings the parameter combination used so far can be kept and used for the final conclusion. As stated before, this is not considered to be *the right* choice, but based on the sensitivity analysis, the results are consistent within a wide parameter range.

5.2.1.4 Results and discussion

The resulting distribution is depicted in Fig. 5.21. To be able to assess how meaningful the frequencies of certain delays are, a random reference distribution is considered. This distribution is obtained by altering the position of the S1-peaks randomly within the range specified by the cavitation valley length of the individual tests. The rest of the method is kept the same. This way 30 random distributions are calculated and the mean of those is used as a reference.

It becomes apparent that the peaks at -5 ms and around 0 ms in the measured distribution deviate strongly from the reference distribution. The third peak around +5 ms is present in the reference as well but at a lower level. The reason for this sharp edge in the distributions gets clear when the combinations are considered separately according to the direction of propagation between S2 and S3 (see Fig. 5.22). The distribution of peaks traveling from the tank towards the valve is sharply cut at approximately 5 ms. This is due to the condition applied before. 5 ms is roughly the delay for a wave traveling with the liquids speed of sound from S3 to S1. Delays Δt_{13} below that for pressure peaks traveling from the tank towards the valve are not possible since that would mean that the wave speeds up between S2 and S1.

It is obvious that much more combinations are found for peaks traveling towards the tank than for peaks coming form the tank. In addition the distribution for S2←S3 is close to the corresponding reference distribution.

As mentioned before, a delay Δt_{13} of -5.19 ms would correspond to a wave being created somewhere between the valve and S1. The extreme prominence of the corresponding bin in the distribution supports the initial hypothesis that the cavitation bubble collapse causes the peaks. If the peaks would directly correspond to the main water-hammer waves, the preferred direction of propagation would be expected to be S3→S2, since in theory during the cavitation phase tank pressure waves would propagate towards the valve and would be reflected as vapor pressure waves at the cavity. However the distribution around 0 ms does not fit well to the expectation. The hypothesis would lead to the expectation that the distribution has its highest point at -5.19 ms and decreases steadily with delays >-5.19 ms. That is because the largest cavitation bubbles are expected to exist close to the valve, both because of theory (the tension is strongest at the valve, bubbles have more time to grow) and observations from the footage from Traudt et al. [26]. The increase observed between -5 and 0 ms is therefore surprising. It would correspond to an accumulation of large bubbles in the center between S1 and S3, but there is no physical reason to assume that this is actually the case. These conclusions about the location of the peaks source rely on the assumption that the wave propagation speed is constant along the pipe and equal to the liquids speed of sound. This is not guaranteed due to

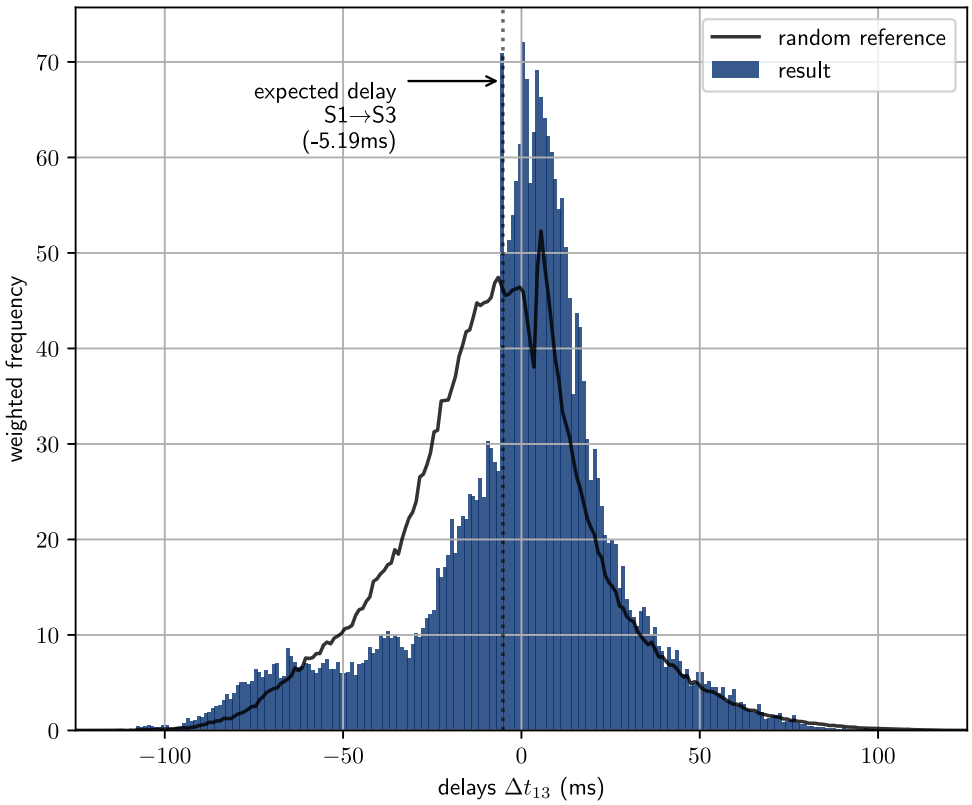

Figure 5.21: Results of water peak delay analysis

intense cavitation, however the peak at -5 ms suggests that in many cases this is actually the case, at least for the corresponding peaks (which might be of especially high amplitude) and between S1 and S3.

Of course, this distribution must not be interpreted as a representation of the actually occurring peak combinations. As a result of the method the distribution includes many combinations whose peaks are not caused by a single common event, even though it would be theoretically possible. Only deviations from the reference distribution, which represents the methods inherent noise, are relevant.

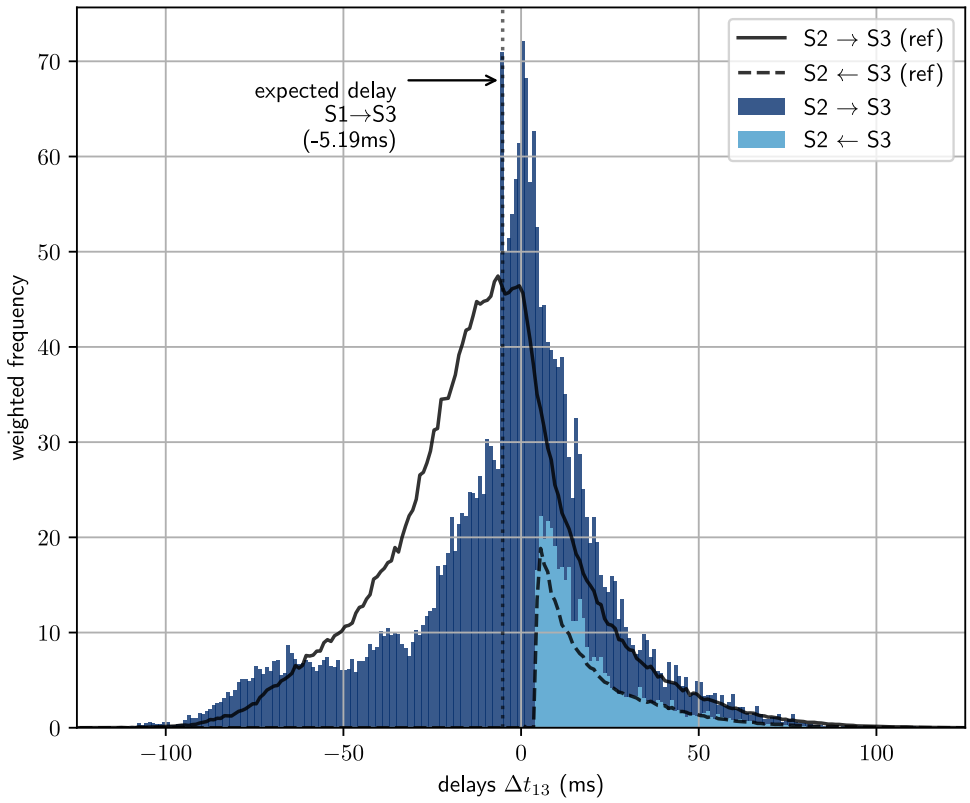

Figure 5.22: Results of water peak delay analysis, split by direction of propagation

5.2.2 Liquid nitrogen

The method described in section 5.2.1 cannot be applied to the LN_2 tests. The characteristics of the pressure readings are vastly different between water and liquid nitrogen. These sharp peak that can be found in water are not present in LN_2. Instead the fluctuations are of rather low frequency. However, a prominent feature in the LN_2 tests is the strong and relatively wide peak in the S1-readings after approximately twice the wave travel time through the pipe. This feature occurs during tests of clusters zero and one. Intuition suggests that this is the pressure wave traveling between cavity and tank which is predicted by theory. Comparing the pressure readings at sensor positions S1 and S2 supports this assumption. One can see the pressure rise at S2 before the peak in S1 and drop after the pressure has dropped in S1 (Fig. 5.23). However, the S3 reading contains an additional oscillation with twice the expected frequency. Klein et al. [14] attributed this frequency to a standing wave with open/open boundary conditions. In general the shape of the waves in S2 and S3 shows that the rectangular shape of the S1-peak is not just explainable by the simple theory of fluid hammer with column separation. It should therefore be investigated in more detail in the following.

5.2.2.1 Timing

First, it should be quantified how well the timing of those peaks coincides with theory. The timing includes both position in time and the duration of the peak. The clustering in section 4.2 succeeded in grouping the tests that show such peaks in clusters 0 and 1. Almost all tests within those clusters feature such a peak. This allows for a very simple method for determining

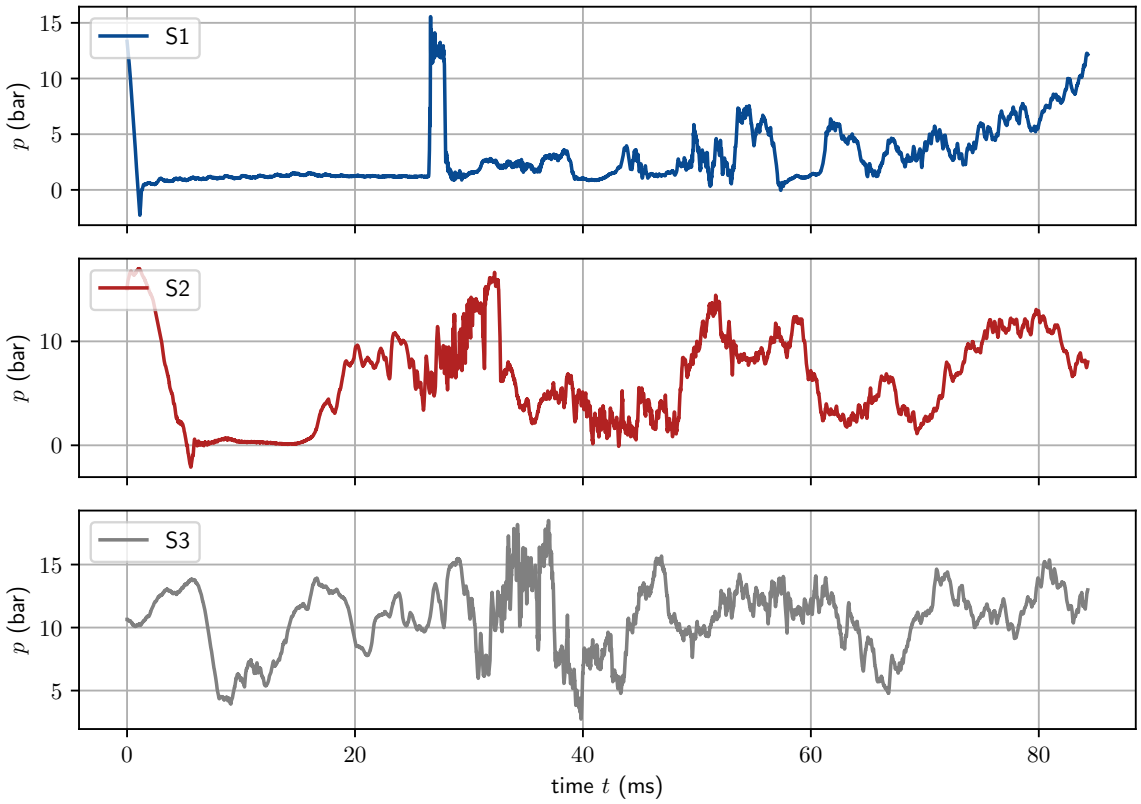

Figure 5.23: Exemplary pressure readings in LN_2

the position of the rising and falling edge of the peak, since such methods usually get complex due to anomalous data, that still has to be treated accurately.

The S1 pressure reading is scaled again, according to equation (4.3). To exclude the initial transient, the noise onset t_{no} defined in section 4.2.1 is used. Setting the timestamp of the first sample of the valley to 0 ms, the data is only considered from $t_{no}/2$ on. The rising and falling edges are now simply defined by the crossings of the pressure signal and a threshold $\tilde{p}_{th}$. The rising edge is the sample i_r where the signal exceeds the threshold the first time. The falling edge is the sample i_f where the signal falls below the threshold again, with the condition $i_f \geq i_r + n_{\text{offset}}$. See Fig. 5.24 for a visualization. This condition ensures that high-frequency oscillations during rise do not lead to an i_f which still lays on the rising edge. Since the number of tests is manageable, it was determined by trial and error, that $n_{\text{offset}} = 20$ has the desired effect.

The threshold $\tilde{p}_{th}$ needs to be chosen in an appropriate way. Therefore a parameter study is performed. In steps of 0.01 the rising and falling edges are detected for all associated tests for thresholds between 0.05 and 1. The deviation between two consecutive thresholds th_j and $\text{th}_{j+1}$is defined as the sum of squares of the deviations of all tests:

$$d_r = \sum \left((i_r)_{\text{th}_j} - (i_r)_{\text{th}_{j+1}} \right)^2 \tag{5.21}$$

or

$$d_f = \sum \left((i_f)_{\text{th}_j} - (i_f)_{\text{th}_{j+1}} \right)^2 \tag{5.22}$$

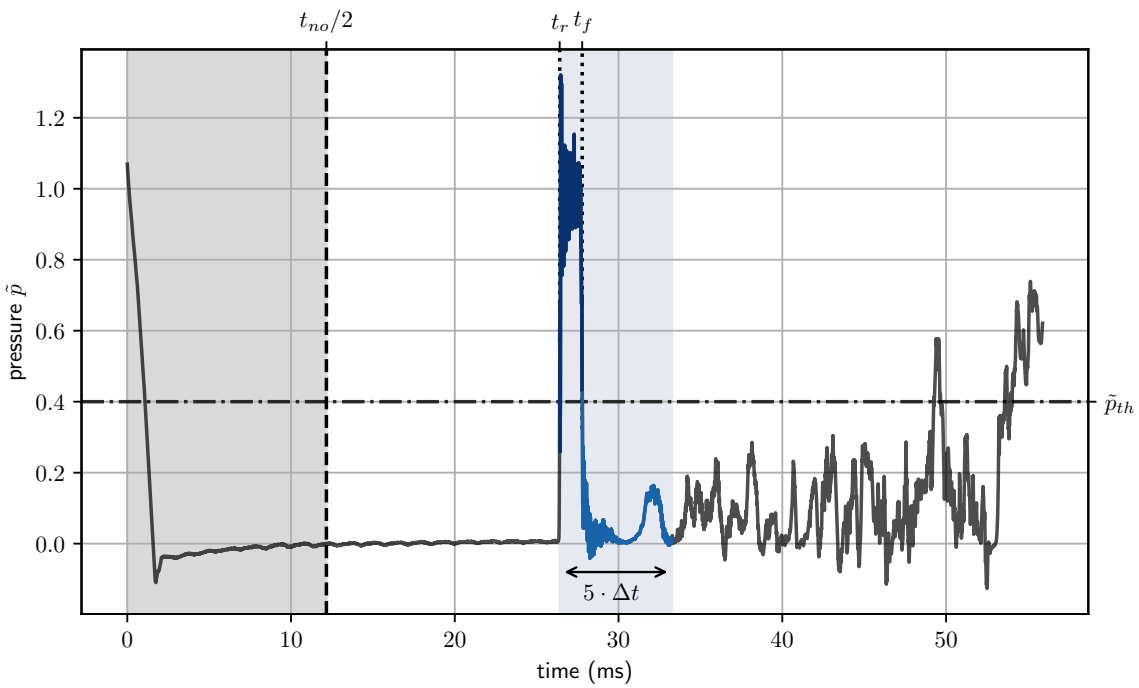

Figure 5.24: Visualization of peak edge detection

respectively. The accumulated deviation is plotted in Fig. 5.25. It can be seen that there is very little change between the thresholds in the range of 0.12 to 0.52. A slight gradient is noticeable in the falling edge branch until thresholds shortly below 0.4. The number of tests in which the peak is detected is decreasing from around th = 0.43 with increasing threshold since the peak is not equally strong in all tests. This is visualized in Fig. 5.25 as well. Therefore th = 0.4 is chosen as a threshold with little impact.

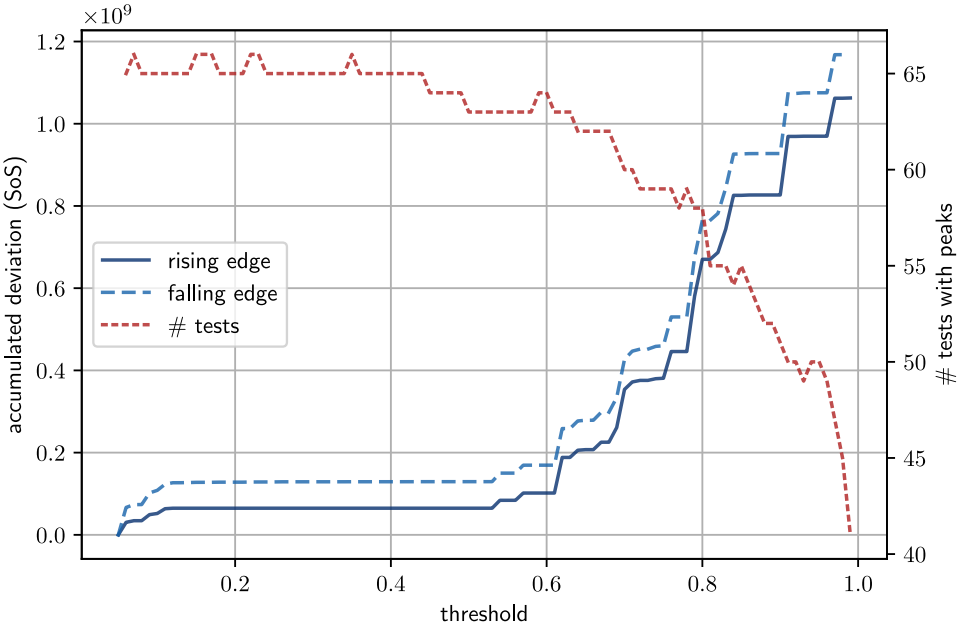

Figure 5.25: Parameter study of threshold used for edge detection

The distribution of time t_r corresponding to the sample i_r over all applicable tests can be evaluated. Since $t = 0$ is determined from the S1 reading, it should be treated as the point of wave passage through position S1 at x_1. The expected time according to theory is therefore $t_{exp} = 2 \cdot \frac{l - x_1}{a}$. The distribution of t_r is shown in Fig. 5.26 on the left. The expected time is displayed as a range according to the measurement errors for p and T which result in a deviation of a. It can be seen that the center of the distribution lies outside of this range. The peak often occurs slightly later than expected. The duration of the peak $\Delta t = t_f - t_r$ can be evaluated the same way. Here the expected duration is $\Delta t_{exp} = 2 \cdot \frac{x_1}{a}$. The resulting distribution is shown on the right of Fig. 5.26. Here it can be seen that the peak is slightly shorter than the theory would suggest.

In both cases the observations are close to the theory but trying to explain the deviations simply by a reduced speed of sound due to cavitation fails as the shorter peak suggests the contrary. If there is a column separation at the valve, the boundary to the liquid could act as a point of reflection instead of the valve, which could explain the deviations.

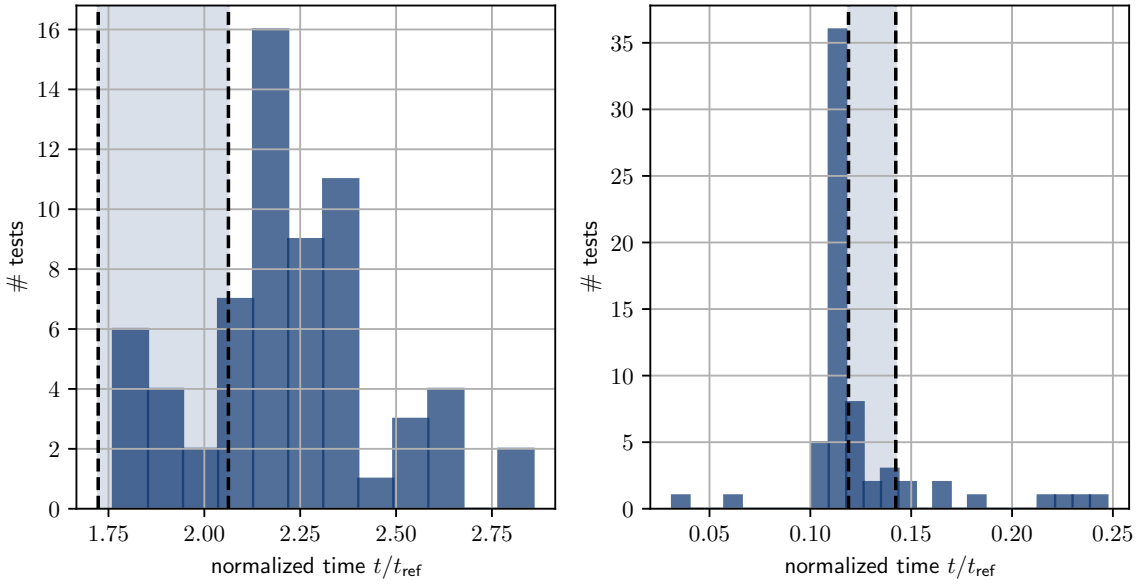

Figure 5.26: Timing of characteristic peak. Left: time until peak, right: duration.

5.2.2.2 High frequency noise

A prominent feature during the characteristic peak is a high frequency noise that seems to occur directly with the rising edge of the peak. The frequency content of this noise will be investigated in the following. It is apparent from the waveform that the noise decays only slowly and is still present after the falling edge of the peak. For the frequency analysis an extended part of the signal can therefore be used. Not only the peak itself but a time span with five times the peak duration, starting at the rising edge, is used. This is visualized in Fig. 5.24. For each test the spectrum is calculated via FFT. To be able to calculate a mean spectrum, all participating spectra need to have a common frequency resolution. Therefore the spectra are downsampled to the minimum frequency resolution. The resulting mean spectrum and the amplitude range between minimum and maximum are shown in Fig. 5.27. It is evident, that frequencies around 25 kHz stand out strongly. In Fig. A.24 the distribution of the frequency

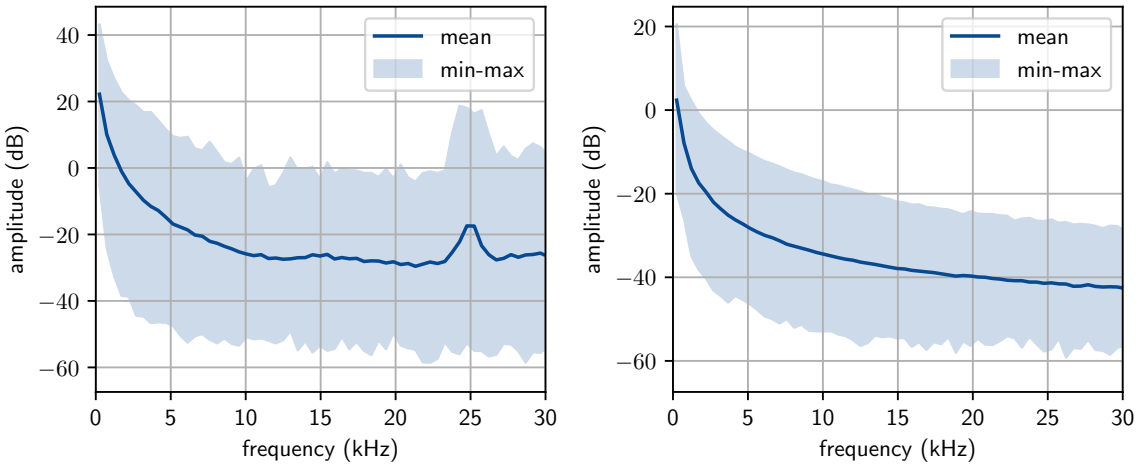

Figure 5.27: Mean frequency spectra. Left: during peak, right: before peak.

with maximum amplitude within the range of 20-30 kHz over all corresponding tests is depicted. It can be seen, that the peak at 25 kHz is not due to a few outliers but this frequency is dominant for the majority of tests. A comparison with the spectrum obtained from the part of the cavitation valley before the rising edge shows that this noise is characteristic for the peak (see Fig. 5.27).

For the sake of completeness it should be noted how the conversion of the amplitudes into decibels takes place. Since the power spectrum is considered, the following conversion is used

$$A = 10 \cdot \log_{10} \left(\frac{P^2}{P_{\text{ref}}^2} \right) \text{dB}, \tag{5.23}$$

where P^2 is the output of the FFT. The reference P_{ref} is chosen to be the uncertainty of measurement of the pressure sensors. Since the pressure signals were scaled, this uncertainty needs to be scaled the same way.

It is noteworthy that this noise seems to consist mainly of one discrete frequency. Since this noise occurs during intense cavitation, it is reasonable to consider the possibility of bubble oscillations as a cause. The bubble size necessary for oscillation with 25 kHz would be well below 1 mm, according to equation (2.20). This seems plausible, however at those small sizes the bubbles would probably be present as clouds. Bubble clouds can have a much lower natural frequency than the individual bubbles [36].

Interestingly, when analysing the frequency content of the signal during the rising edge of the first main fluid hammer peak, a similar frequency seems to be standing out. For that, simply the time interval $\Delta t = t_{\text{ref}}$ right at the first pressure rise is considered. This is visualized in Fig. 5.28 on the left. In the same figure on the right the measured frequency spectrum is shown. At approximately 26 kHz, the prominent frequency is slightly higher than during the characteristic peak during cavitation.

One possible explanation for this observation could be that a very sharp increase in pressure, as it is present during both the first fluid hammer peak and the characteristic peak, might excite vibrations in the structure. In this case the measured noise could be the result of a fluid

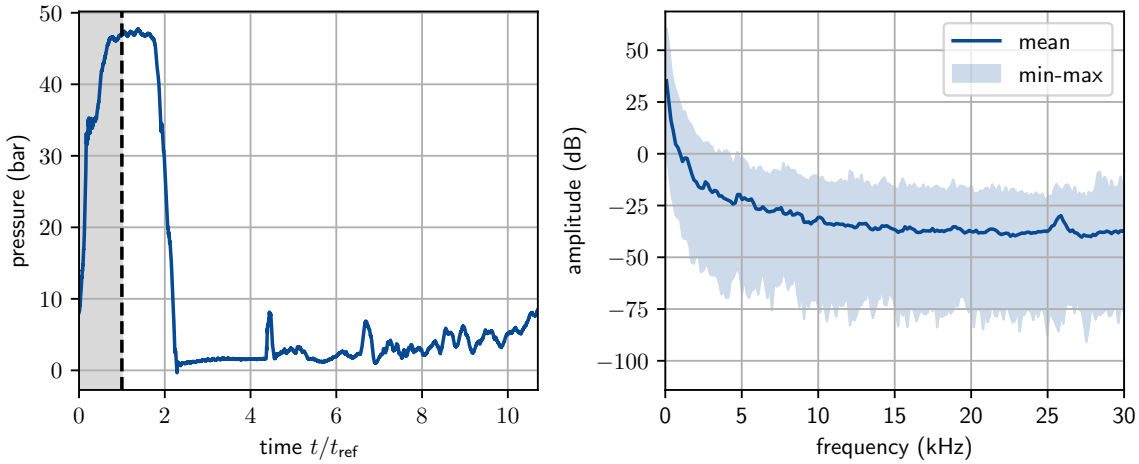

Figure 5.28: Frequency analysis of first rise. Left: considered slice of pressure signal, right: spectrum.

structure interaction and the frequency difference mentioned above could be due to the two phase conditions during the cavitation phase.

It can be seen that this high frequency noise is present in all three sensors. The noise onset, however, does not simply go along with the rising edge of the pressure wave. Instead it appears as if the noise originates from some point along the pipe and propagates from there towards the valve and the tank.

By comparing the pressure traces of the three sensors in 5.23 it is apparent that the pressure rise during the first wave passage is much steeper at position S1 than at S2 or S3. From gas dynamics it is known that a pressure wave travelling through a compressible medium becomes steeper over time. Since the speed of sound in compressible fluids is dependent on the pressure, the low pressure part of a rising edge of a pressure wave will travel more slowly than the high pressure part. From literature a homogeneous two-phase mixture would be expected in LN_2 during cavitation, which could explain the compressibility of the fluid. That would mean that the noise is excited at the point in the pipe where the rising edge of the pressure wave reaches some critical steepness.

It should be made clear that this hypothesis goes beyond the scope of this thesis since the available data is not sufficient for robust claims on this theory. However, it demonstrates the importance of a detailed investigation of the onset of this high frequency noise, which will be conducted in the following. The following two questions shall be investigated:

(1) Can the noise onset in all three sensors be traced back to one common source?

(2) If so, can a relationship be found between the position of this source and the boundary conditions of the tests?

5.2.2.3 Noise source tracking

The idea of the method for determining the location of the noise source is the following:

- Determine the point of time of the noise onset at all sensor positions.
- Calculate the delays between the three noise onsets.

- Assume a constant speed of propagation, since even the high frequency noise has a large amplitude compared to acoustic disturbances.
- With this information calculate the theoretical origin of the noise.

This principle is visualized in Fig. 5.29.

Since only the specific 25 kHz noise is relevant, the signals are band-pass filtered, keeping the frequency band between 22 and 28 kHz. Onset detection is usually done with more sophisticated approaches operating in frequency domain [37]. However, since the considered signal is now of very narrow bandwidth, such approaches are not applicable. Therefore amplitude and time based approaches have to be used.

The basic method after band-pass-filtering is the following: Use the first part of the signal with a time-span of t_{ref} as reference. It was checked that the noise onset never occurs within this time for any sensor. The RMS-value of this part is calculated and referred to as $\hat{p}_{\text{ref}}$ in the following. Since the problem is well constrained it can be seen that the leftover signal can be cropped to a duration of $4 \cdot t_{\text{ref}}$ in order to reduce complexity of the following steps. After this time the noise has already decayed.

On this signal a moving RMS $\hat{p}$ is calculated. A small filter size is desired here to reduce the error due to a smearing of the transients. Manual inspection showed, that 25 samples produces reasonable results.

In the signal from sensor S1 the onset is very sharp and therefore easy to detect. Here the noise onset can be defined as the first sample at which the condition $\hat{p} > \hat{p}_{\text{ref}} + \hat{p}_{\text{th}}$ is met. The threshold $\hat{p}_{\text{th}}$ is set to 0.02 bar. Manual inspection showed that the onset is characterized

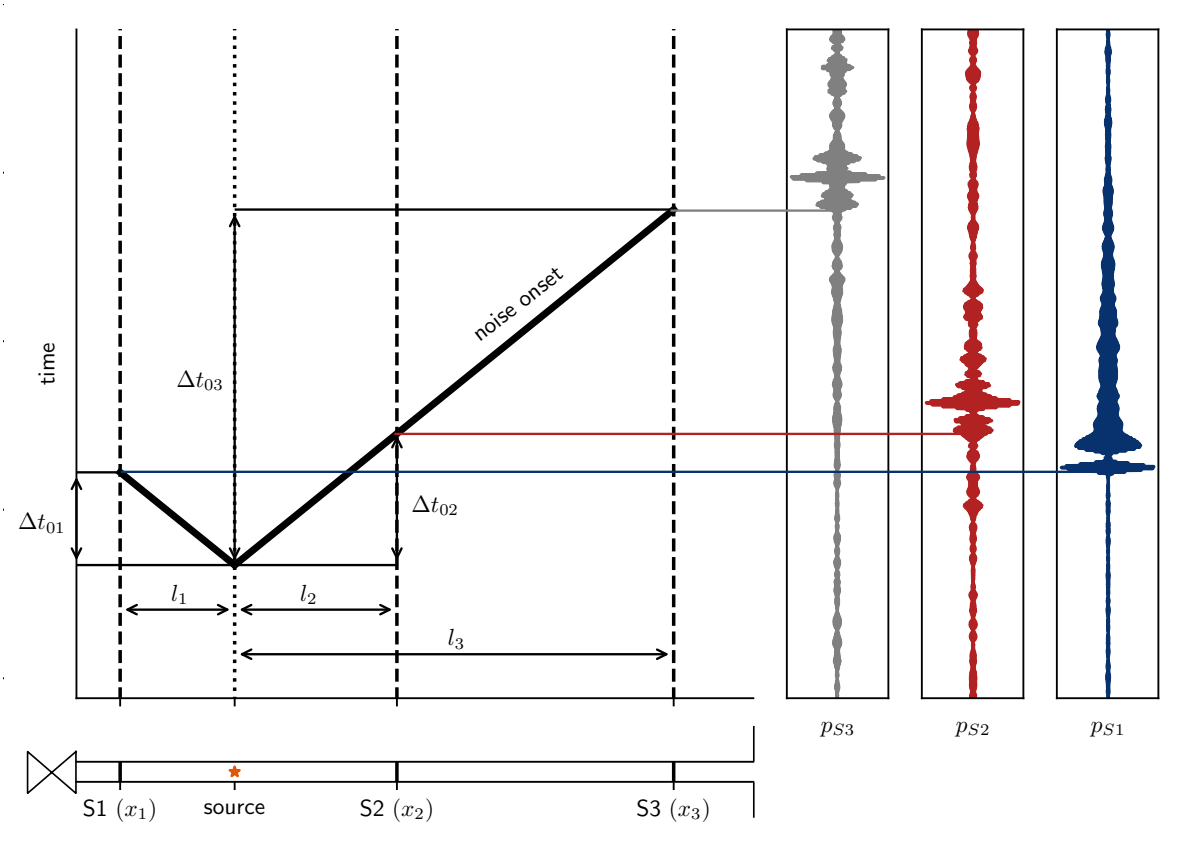

Figure 5.29: Schematic of noise onset tracking

correctly in all corresponding tests by this method. Since the onset is very sharp, there is no need for analyzing the influence of $\hat{p}_{\mathrm{th}}$. It can clearly be seen, that this choice produced the very good results. The only uncertainty comes from the filter size of the moving RMS and is therefore small enough to be neglected for the purpose of this analysis.

For sensors S2 and S3 the onset definition is not as easy. The onset differs in sharpness and the amount of ground noise even before the noise onset is not consistent between the tests. The chance of misdetection is considerably higher than for S1 using the simple approach described above. Additionally, even with manual inspection it is not clear where exactly the noise sets on.

It was found that the waveforms of the filtered S2 and S3 signals are usually similar. The delay between those two signals can therefore be determined via cross-correlation. Calculating the cross-correlation simply on the bandpass filtered signals, however, proved to be unreliable in this case. A few pre-processing steps need to be carried out:

- The positive envelopes $\underline{\boldsymbol{e}}$ of the signals $\underline{\hat{\boldsymbol{p}}}$ are calculated as shown in Fig. 5.30 a).
- The mean of the envelope is set to zero by $\underline{\boldsymbol{e}} - \mathrm{mean}\,(\underline{\boldsymbol{e}})$.
- The shifted envelope is scaled to an absolute maximum of 1 by $\underline{\boldsymbol{e}}/\max\,(\mathrm{abs}\,(\underline{\boldsymbol{e}}))$.
- Since the matching features between both signals often are relatively short peaks, additional scaling is applied in order to increase the relative amplitude of those peaks:

$$\underline{\boldsymbol{e}}_s = \underline{\boldsymbol{e}} \cdot [\mathrm{abs}\,(\underline{\boldsymbol{e}}) \cdot (1 - s) + s]\,. \tag{5.24}$$

With this scaling function each value is scaled according to the term in rectangular brackets. The parameter s determines the degree of scaling. For $s = 1$ there is no scaling since the term would be equal to 1. For $s = 0$ each value is scaled by its absolute value. To increase the robustness, the cross correlation is performed for multiple values for s between 0.1 and 0.9. Moving forward, the mean of the resulting cross-correlations is used. An exemplary cross-correlation is depicted in Fig. 5.30 b). The delay Δt_{23} between sensors S2 and S3 is then obtained from the lag τ with the maximum cross-correlation value.

The moving RMS of both signals calculated before can be shifted according to this delay ($\underline{\hat{\boldsymbol{p}}}'$) and summed up to:

$$\underline{\hat{\boldsymbol{p}}}'_{sum} = \underline{\hat{\boldsymbol{p}}}'_{S2} + \underline{\hat{\boldsymbol{p}}}'_{S3}. \tag{5.25}$$

The condition for the noise onset is now $\underline{\hat{\boldsymbol{p}}}'_{sum} > (\hat{p}_{\mathrm{ref}})_{S2} + (\hat{p}_{\mathrm{ref}})_{S3} + \hat{p}_{\mathrm{th}_2}$ (see Fig. 5.30). The time of the noise onset found here is offset with the Δt_{23} to find the onset time in the original signal. The delay between S2 and S3 is not affected by this definition but is solely defined by the cross-correlation. The delays Δt_{12} and Δt_{13} however are based on this definition. The cross-correlation is used to achieve more consistent results. The cross-correlation is more likely to find the true delay Δt_{23} than the RMS-threshold alone.

With those delays one can calculate the theoretical location of the source. As mentioned before, for this the speed of propagation has to be assumed to be constant. The noise under consideration with amplitudes around 0.1 to 0.2 bar cannot be considered as an acoustic oscillation. Therefore the reduction of the propagation speed can be less severe. As known

from theory, shock waves can travel through a bubbly liquid with velocities much higher than the reduced speed of sound [19]. It was also seen, that the main wave seems to travel with approximately the speed of sound of the liquid phase. Therefore here, the speed of propagation is assumed to be constant and equal to the speed of sound in the liquid phase. This assumption still is a simplification and the quantitative results should be treated with caution.

The delays between source and the sensors can then be obtained by

$$\Delta t_{01} = \frac{l_1}{a}, \quad \Delta t_{02} = \frac{l_2}{a}, \quad \Delta t_{03} = \frac{l_3}{a}. \tag{5.26}$$

The observed delay between two sensors can then be expressed as

$$\Delta t_{12} = \Delta t_{02} - \Delta t_{01} = \frac{l_2}{a} - \frac{l_1}{a}, \quad \Delta t_{13} = \frac{l_3}{a} - \frac{l_1}{a}, \quad \Delta t_{23} = \frac{l_3}{a} - \frac{l_2}{a}. \tag{5.27}$$

See Fig. 5.29 for a visual explanation of those variables. Since

$$l_1 + l_2 = x_2 - x_1, \quad l_1 + l_3 = x_3 - x_1, \quad l_2 + l_3 = x_3 - x_2 \tag{5.28}$$

are known, the equations above can be resolved for any l. Since this is a 1D-problem, two sensors would be enough for localization in between those two sensors. The third sensor can be used to check for consistency. The source position will be expressed as distance to S1 (l_1).

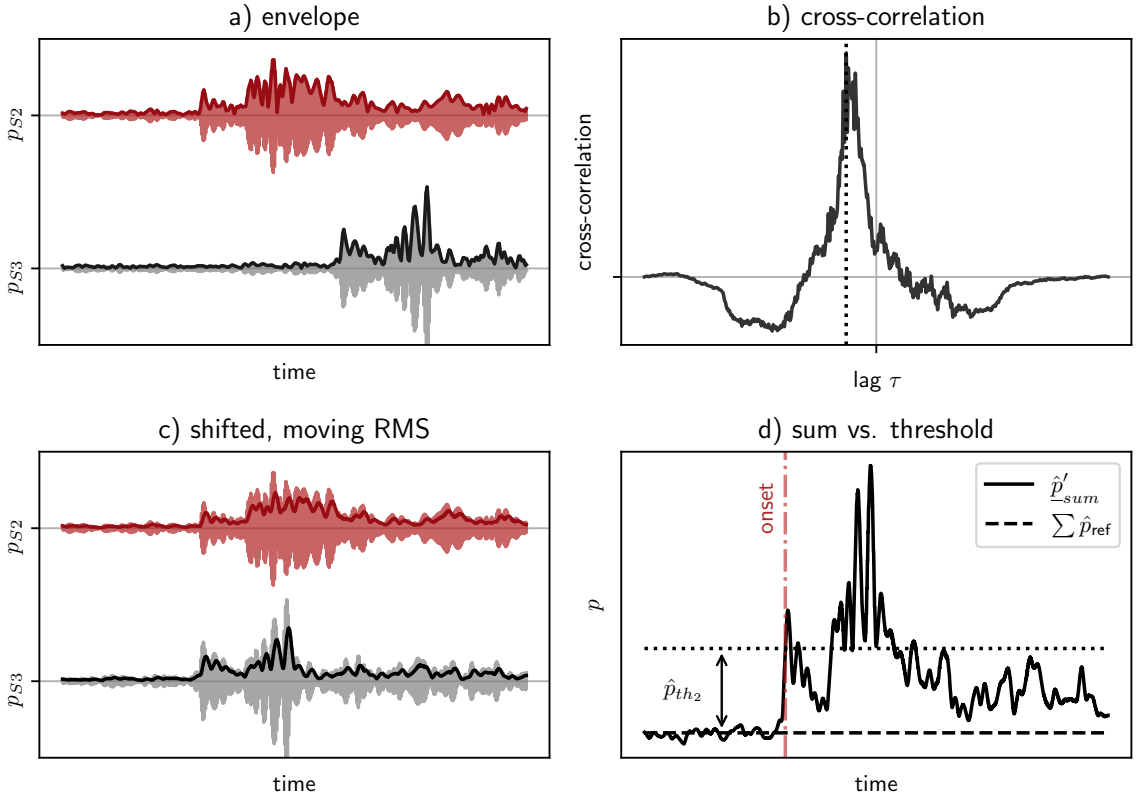

Figure 5.30: Schematic of onset detection in S2 and S3

This can be done in two ways:

$$l_1 = \frac{x_{12} - a\Delta t_{12}}{2} \quad \text{or} \tag{5.29}$$

$$l_1 = \frac{x_{13} - a\Delta t_{13}}{2}. \tag{5.30}$$

Equations (5.29) and (5.30) are identical if $a \cdot \Delta t_{23} = x_3 - x_2$. Since the noise onset in S2 and S3 depends on the choice of the threshold $\hat{p}_{\mathrm{th}_2}$ and since it is not obvious how to define a *correct* threshold, the position is calculated for various different thresholds between 0.01 and 0.2. The results are scattered in Fig. 5.31 over the initial tension which is expressed by the difference of the theoretical Joukowsky pressure according to (2.1) and the "distance" between system pressure and vapor pressure. For every test, the distribution of calculated positions for the different thresholds is visualized by a standard boxplot. To check for consistency, l_2 is considered according to

$$l_2 = \frac{x_{23} - a\Delta t_{23}}{2} \tag{5.31}$$

and is plotted in Fig. 5.31 on the top. Note that the threshold $\hat{p}_{\mathrm{th}_2}$ has no influence here, because Δt_{23} depends on the cross-correlation only. Since l_2 is calculated from sensor pair (S2, S3), a source position outside the range between both sensors cannot be resolved. It would therefore be expected that for $l_1 < x_2 - x_1$ the condition $l_2 = 0$ m holds. Likewise, l_1 is expected to lay between 0 m and $\Delta x_{12} = 3.8$ m. The results in Fig. 5.31 show mostly good agreement with those expectations. The calculated distance l_2 has a small relatively constant offset from 0 m which indicates a small deviation in the speed of sound. Considering the deviation of $\pm 9\%$ only due to the measurement resolution of the pressure and temperature sensors, this is not unexpected. A few tests, however, show relatively strong deviation. It can be seen that the tests with $l_1 < 0$ m also have an anomalous l_2. Those tests show an anomalous behavior in general as it is noticeable that for those tests the noise onset is only detected for small thresholds $\hat{p}_{\mathrm{th}_2}$. The values exceeding Δx_{12} at high tensions indicate a slower speed of sound between S2 and S1 than calculated. This was seen in the timing analysis of the rising edge as well and is therefore not surprising.

Given that for the majority of tests the conditions are met or deviations are small and explainable, it can be safely assumed that the noise in all three sensors indeed has a common origin.

From Fig. 5.31 it is also clear that the calculated source position follows a trend depending on the boundary conditions. The higher the initial tension, the closer the position l_1 is to the tank.

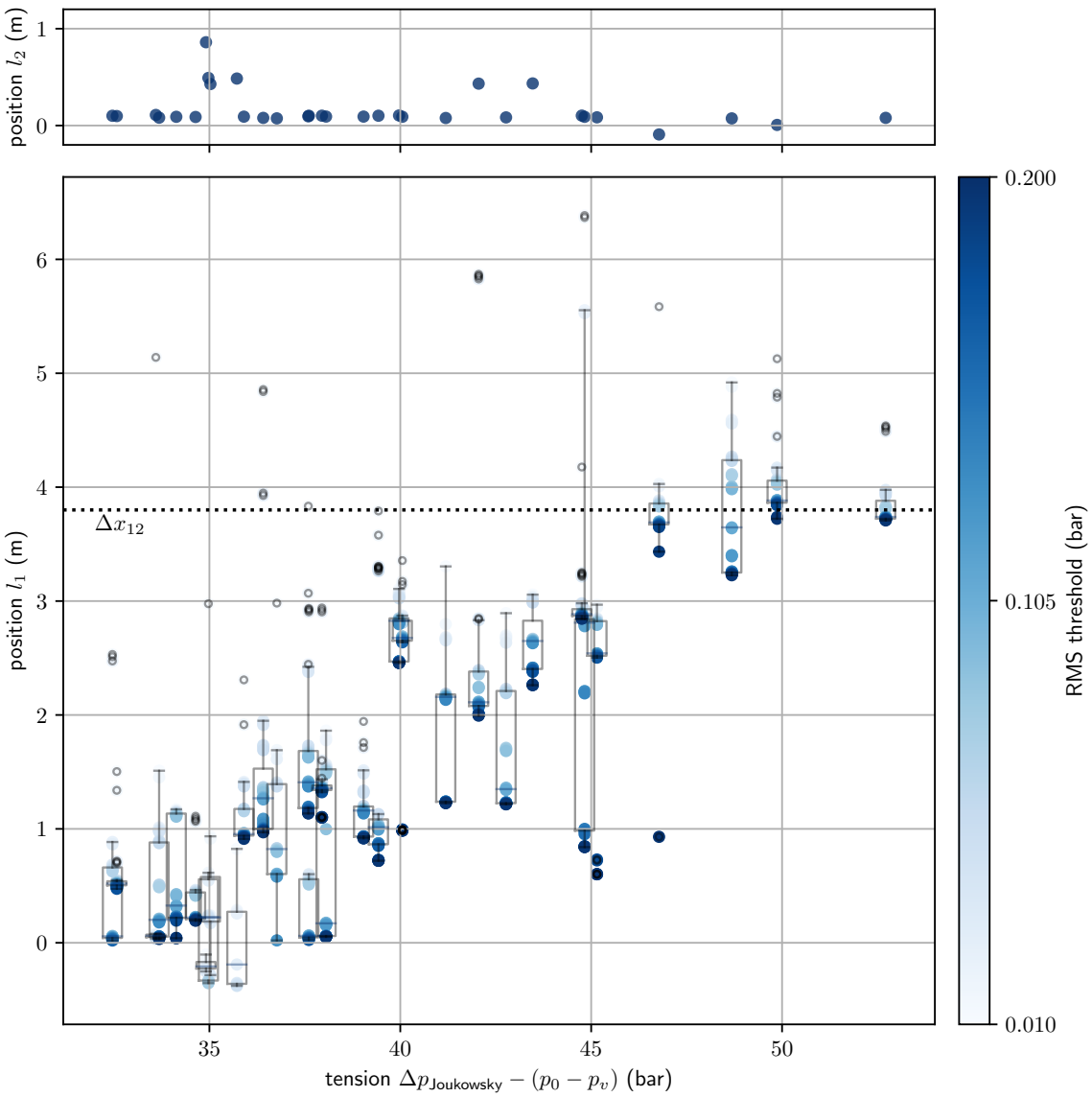

Figure 5.31: Noise source tracking results

5.2.2.4 Discussion

The localization of the source has a lot of uncertainty. The possible error of the calculated speed of sound is relatively large and the assumption of a constant speed of sound is a simplification, even though the results suggest that the reality is not far off. Otherwise it would be expected that the calculated values for l_1 and l_2 violate the consistency conditions more severely. Additionally the determination of the noise onset in S2 and S3 is still vague. However, for the purpose of this analysis only qualitative information is needed, which is satisfactorily provided by this method.

The main findings of the noise onset analysis are the following:

- The noise onset in the different sensors can be tracked back to a common point of origin. The noise appears to be excited at some location in the pipe between S1 and S2 as the wave passes through.

- This location depends on the tension on the fluid. A higher tension goes along with a location closer to the tank.

The results fit to the theory mentioned previously, that the main pressure wave becomes steeper while travelling through the pipe, eventually leading to the excitation of the high-frequency vibration. If this is true, a likely cause for the steepening is the presence of a homogeneous two-phase mixture due to the cavitation. Even though the compressibility of liquid nitrogen itself is comparably high, it is not sufficient to explain the fast steepening observed in the measurements, as the estimation in A.2 shows. It also fits that the position of the source shifts towards the tank with increasing tension. Given the considerations above, this would indicate that the cavitation region is spread further into the pipe with higher tension, which fits to theory.

These considerations are merely one possible interpretation of the observations. Even though the results of this analysis are consistent with the hypothesis proposed above, it cannot be ruled out that a different mechanism would cause the same observations. By no means the results can be viewed as evidence for the hypothesis. Additional insight would be needed by more dense instrumentation and preferably an optical access. The assumption that the noise is caused by fluid-structure interactions would have to be checked by a dedicated analysis of the test bench.

6 Conclusion

The aim of this thesis was to provide insight into certain aspects of pressure fluctuations during the cavitation phase following pressure surges. The noise in general was considered as well as short duration peaks in the pressure readings.

The measurement data consisted of a multitude of individual tests. In order to allow for a meaningful statistical evaluation, the tests were clustered first according to the characteristics of the pressure readings at the sensor position closest to the valve during the first cavitation phase. Seven parameters were proposed to describe those characteristics. It was found that the clustering in this 7-dimensional space lead to reasonable clusters in the space of the tests boundary conditions as well.

Based on these clusters the behavior of the noise over time was evaluated statistically. It was found that in water the noise in the liquid phase is independent from the noise in the cavitation region. No matching pattern was observed between those two regions. In contrast, the noise in liquid nitrogen showed a strong coupling between the cavitation and liquid phase regions. The dependence of the noise on the main pressure wave seems to be much more obvious in LN_2 than in water.

Short duration peaks were noticed in the water tests, especially at sensor S1. The previous statistical evaluation indicated that those peaks occur rather randomly and do not accumulate at certain points in time. To investigate the nature of those peaks a tracking method was proposed which interrelates the occurrence of those peaks at the different sensor positions in order to analyze the delays for clues to the origin of the peaks. Since only three sensor positions were available, the peaks measured at those positions could not be clearly correlated and a broad approach was needed. Conclusions could be drawn from statistical accumulations of delays and the deviation from the random reference. It was observed that an extraordinarily large portion of peaks originate from the part of the pipe between valve and sensor S1. This supports the theory that the peaks are caused by the collapse of cavitation bubbles, since the largest bubbles are expected to be located in this region.

In liquid nitrogen, a characteristic peak resembling a square wave pulse was observed in many tests at the sensor position closest to the valve. Certain aspects of this dominant feature were observed in more detail. It was shown that the timing of these peaks is in rough

agreement with the timing of the main pressure wave which is expected by theory during the cavitation phase. However, deviations suggest a reduced speed of sound, possibly due to the cavitation. The duration (or width) of the peaks also matches the theory with some deviations. Those deviations seem to contradict the deviations of the timing at first glance. A possible explanation could be the presence of a column separation at the valve.

It was observed that these peaks often go along with a high frequency noise with a discrete frequency of approximately 25 kHz. A method was developed to determine the onset of this noise at all three sensor positions in order to locate the origin of the noise. It was shown that the noise indeed seems to originate from a point in the pipe which usually lies between sensor positions S1 and S2. It seems to be excited upon wave passage. The position of this point of origin was shown to depend on the boundary conditions of the test. At higher tensions the origin lies closer to the tank. This finding is especially interesting since the cavitation is expected to spread further into the pipe at higher tensions as well. A hypothesis for the mechanism causing the noise was put forward.

Based on literature and previous considerations the expectation is, that a main difference between water and LN_2 lies in the number and size of the cavitation bubbles. In water, larger bubbles and an inhomogeneous distribution is expected, while for LN_2 theory would suggest a fog-like appearance, i.e. many small homogeneously distributed bubbles. The observations of this work are in line with these expectations: The decoupling between cavitation region and liquid column, which was observed in water during the investigation of the noise over time, indicates a vastly different nature of the cavitation than in LN_2. The pressure spikes observed in water seem to originate from bubble collapse which would suggest relatively large bubbles. In LN_2 no such spikes were observed. Instead wave steepening and the excitation of high-frequency noise were seen which could potentially be explained by a distributed homogeneous two-phase mixture.

However, those are merely interpretations of the observations. For robust claims on the nature of the cavitation more extensive instrumentation would be needed. With a larger number of pressure sensors spread along the pipe the propagation of the pressure waves and peaks could be tracked more reliably which could enable more far-reaching conclusions. A definite proof of the differences in the nature of the cavitation would require an optical access. It would be best to have multiple such accesses distributed over the pipe in order to evaluate the spread of the cavitation and potentially observe the pressure waves visually.

References

[1] C. Lardier. “The soviet manned lunar program N1-L3”. In: *Acta Astronautica* 142 (2018), pp. 184–192.

[2] V. L’Hullier. “Propulsion in the ATV Spacecraft System - Lessons Learnt”. In: *45th AIAA/ASME/SAE/ASEE Joint Propulsion Conference & Exhibit*. Denver, 2009.

[3] A. Bergant, A. Simpson, and A. Tijsseling. “Water hammer with column separation: A historical review”. In: *Journal of Fluids and Structures* 22.2 (2006), pp. 135–171.

[4] C. Bombardieri, T. Traudt, and C. Manfletti. “Experimental and Numerical Analysis of Water Hammer During the Filling Process of Pipelines”. In: *Space Propulsion 2014*. 2014.

[5] J. Záruba. *Water Hammer in Pipe-Line Systems*. Vol. 43. Developments in Water Science. Elsevier, 1993.

[6] B. B. Sharp and D. Sharp. *Water hammer: practical solutions*. Oxford a.o.: Butterworth-Heinemann, 1996.

[7] M. S. Ghidaoui, M. Zhao, D. A. McInnis, and D. H. Axworthy. “A Review of Water Hammer Theory and Practice ”. In: *Applied Mechanics Reviews* 58.1 (Mar. 2005), pp. 49–76.

[8] D. J. Korteweg. “Ueber die Fortpflanzungsgeschwindigkeit des Schalles in elastischen Röhren (On the propagation speed of sound in elastic pipes)”. In: *Annalen der Physik* 241.12 (1878). (in German), pp. 525–542.

[9] E. B. Wylie and V. L. Streeter. *Fluid transients*. New York u.a.: McGraw-Hill, 1978.

[10] A. Bergant, A. S. Tijsseling, J. P. Vítkovský, D. I. Covas, A. R. Simpson, and M. F. Lambert. “Parameters affecting water-hammer wave attenuation, shape and timing—Part 1: Mathematical tools”. In: *Journal of Hydraulic Research* 46.3 (2008), pp. 373–381.

[11] H.-M. Prasser, A. Böttger, and J. Zschau. *Entwicklung von Zweiphasenmeßtechnik für vergleichende Untersuchungen zur Beschreibung von transienten Strömungen in Rohrleitungen (Development of two-phase measurement technology for comparative investigations to describe transient flows in pipelines)*. Tech. rep. FZR-233. (in German). Forschungszentrum Rossendorf, Feb. 1999.

[12] E. B. Wylie. “Simulation of Vaporous and Gaseous Cavitation”. In: *Journal of Fluids Engineering* 106.3 (Sept. 1984), pp. 307–311.

[13] D. Duri, P. Kreit, J.-L. Bozet, and S. Le Martelot. “Atomization chill-down demonstrator for the next generation cryogenic rocket engines: experiments and first results”. In: *8TH EUROPEAN CONFERENCE FOR AERONAUTICS AND SPACE SCIENCES (EUCASS)*. Madrid, Spain, 3July 2019.

[14] S. Klein, T. Traudt, and M. Oschwald. “Comparison between water and liquid nitrogen pressure surge experiments to analyse cavitation induced noise growth”. In: *11th International Symposium on Cavitation*. Daejon, Korea, 2021.

[15] J. Steelant. “Multi-Phase Fluid-Hammer in Aerospace Applications”. In: *12th International Conference on Pressure Surges*. Dublin, Ireland, 2015.

[16] R. P. Prickett, E. Mayer, and J. Hermel. “Water Hammer in a Spacecraft Propellant Feed System”. In: *Journal of Propulsion and Power* 8.3 (1992), pp. 592–597.

[17] B. Brunn. “Kavitation und die Zugfestigkeit von Flüssigkeiten (Cavitation and the Tensile Strength of Liquids)”. (in German). Ph.D. Thesis. Darmstadt, Germany: Technische Universität Darmstadt, 2006.

[18] D. H. Trevena. *Cavitation and tension in liquids*. Bristol, Philadelphia: Adam Hilger, 1987.

[19] C. E. Brennen. *Cavitation and Bubble Dynamics*. Vol. 44. Oxford engineering science series. New York, Oxford: Oxford University Press, 1995.

[20] H. W. Xiang. *The Corresponding-States Principle and its Practice. Thermpdynamic, Transport and Surface Properties of Fluids*. Amsterdam a.o.: Elsevier, 2005.

[21] J.-P. Franc and J.-M. Michel. *Fundamentals of cavitation*. Vol. 76. Fluid mechanics and its applications. Dordrecht u.a.: Kluwer Academic Publishers, 2004.

[22] A. Wei, L. Yu, L. Qiu, and X. Zhang. "Cavitation in cryogenic fluids: A critical research review". In: *Physics of Fluids* 34.10 (2022).

[23] M. G. De Giorgi, D. Bello, and A. Ficarella. "Analysis of Thermal Effects in a Cavitating Orifice Using Rayleigh Equation and Experiments". In: *Journal of Engineering for Gas Turbines and Power* 132.9 (June 2010).

[24] M. Petkovšek and M. Dular. "Cavitation dynamics in water at elevated temperatures and in liquid nitrogen at an ultrasonic horn tip". In: *Ultrasonics Sonochemistry* 58 (2019).

[25] Y. Zhang, X. Ren, Y. Wang, X. Li, Y. Ito, and C. Gu. "Investigation of the cavitation model in an inducer for water and liquid nitrogen". In: *Proceedings of the Institution of Mechanical Engineers, Part C: Journal of Mechanical Engineering Science* 233.19-20 (2019).

[26] T. Traudt, C. Bombardieri, and C. Manfletti. "High Speed Imaging of Water Hammer with Column Separation". In: *12th International Conference Pressure Surges 2015*. 2015.

[27] M. L. Rodríguez. "Multiphase Fluid Hammer: Modeling, Experiments and Simulations". Ph.D. Thesis. Spain: Universidade da Coruña, 2013.

[28] M. Jansson, M. Andersson, and M. Karlsson. "High-Speed Imaging of Water Hammer Cavitation in Oil–Hydraulic Pipe Flow". In: *Fluids* 7 ().

[29] J. B. Gouriet, A. Huertas-Martinez, J. M. Buchlin, M. R. Vetrano, and J. Steelant. "Multiphase Fluid Hammer with Cryogenic Fluids". In: *Space Propulsion 2016*. 2016.

[30] G. Agrawal, S. Sunil Kumar, and D. K. Agarwal. "Pressure Surge During Cryogenic Feedline Chilldown Process". In: *Journal of Thermal Science and Engineering Applications* 8.1 (Nov. 2015).

[31] S. Klein, T. Traudt, and M. Oschwald. "Influence of cavitation on the acoustic boundary conditions in water hammer experiments". In: *18th International Symposium on Transport Phenomena and Dynamics of Rotating Machinery*. 2020.

[32] E. B. Wylie, V. L. Streeter, and L. Suo. *Fluid transients in systems*. NJ: Prentice Hall Englewood Cliffs, 1993.

[33] C. M. Bishop. *Pattern Recognition and Machine Learning*. Information Science and Statistics. New York: Springer, 2006.

[34] P. J. Rousseeuw. "Silhouettes: A graphical aid to the interpretation and validation of cluster analysis". In: *Journal of Computational and Applied Mathematics* 20 (1987), pp. 53–65.

[35] J. Bode, G. E. A. Meier, and M. Rein. "Cavitation behind tension waves". In: *Adiabatic Waves in Liquid-Vapor Systems*. Berlin, Heidelberg: Springer, 1990.

[36] D. Koller and P. Shankar. "Acoustical emissions from bubble clouds". In: *Ultrasonics* 32.3 (1994), pp. 229–233.

[37] D. Stowell and M. D. Plumbey. "Adaptive whitening for improved real-time audio onset detection". In: *Proceedings of the International Computer Music Conference (ICMC'07)*. Copenhagen, Denmark, Aug. 2007, pp. 312–319.

A

Appendix

A.1 Supplementary figures

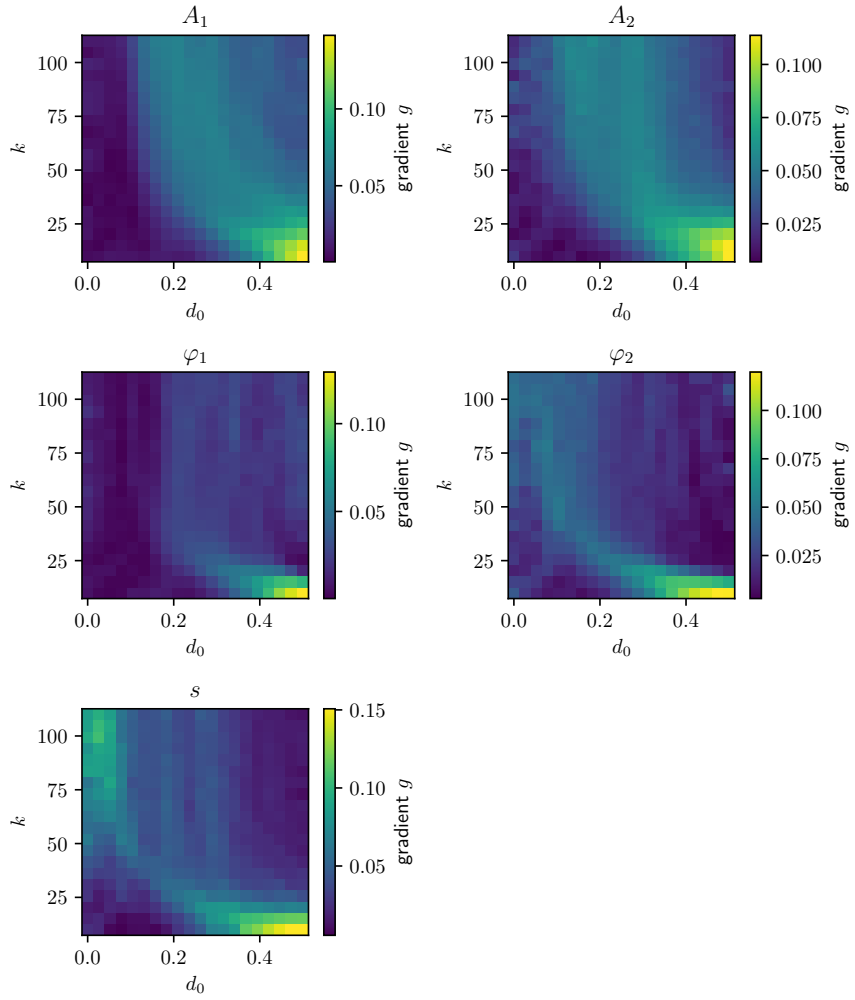

Figure A.1: Gradients per cluster parameter

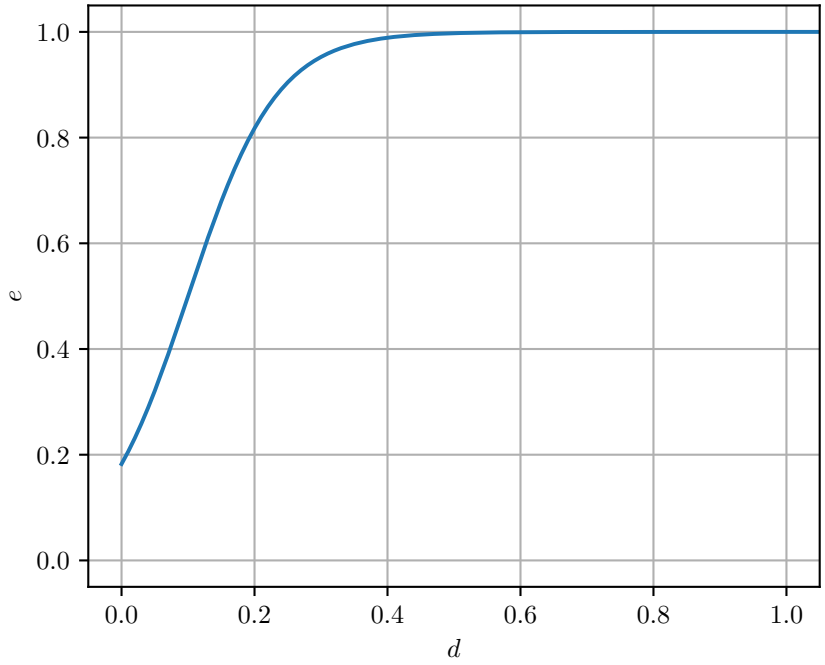

Figure A.2: Logistic error function with parameters chosen via parameter study

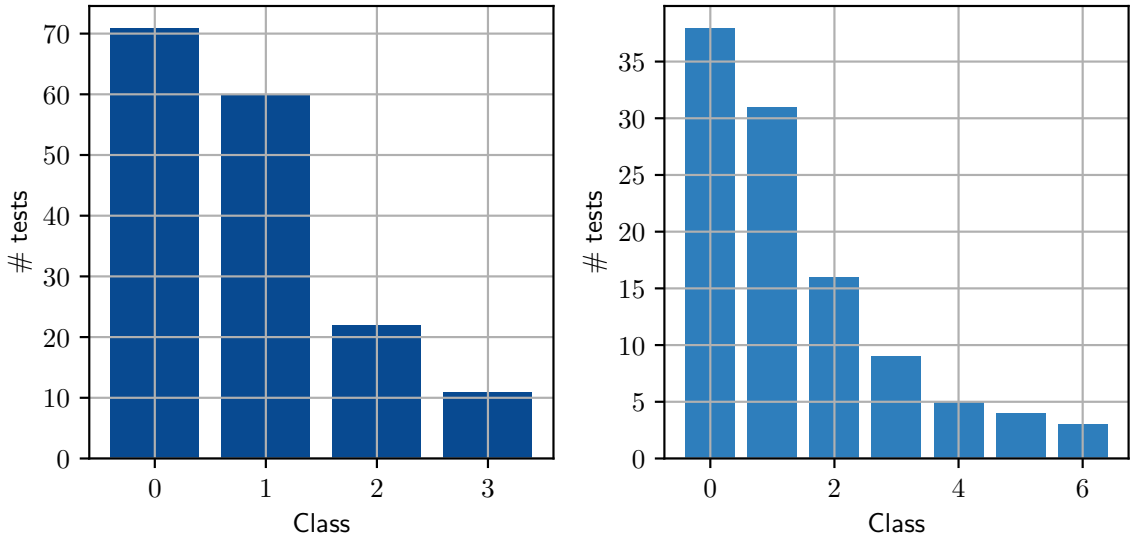

Figure A.3: Cluster sizes. Left: water, right: LN_2

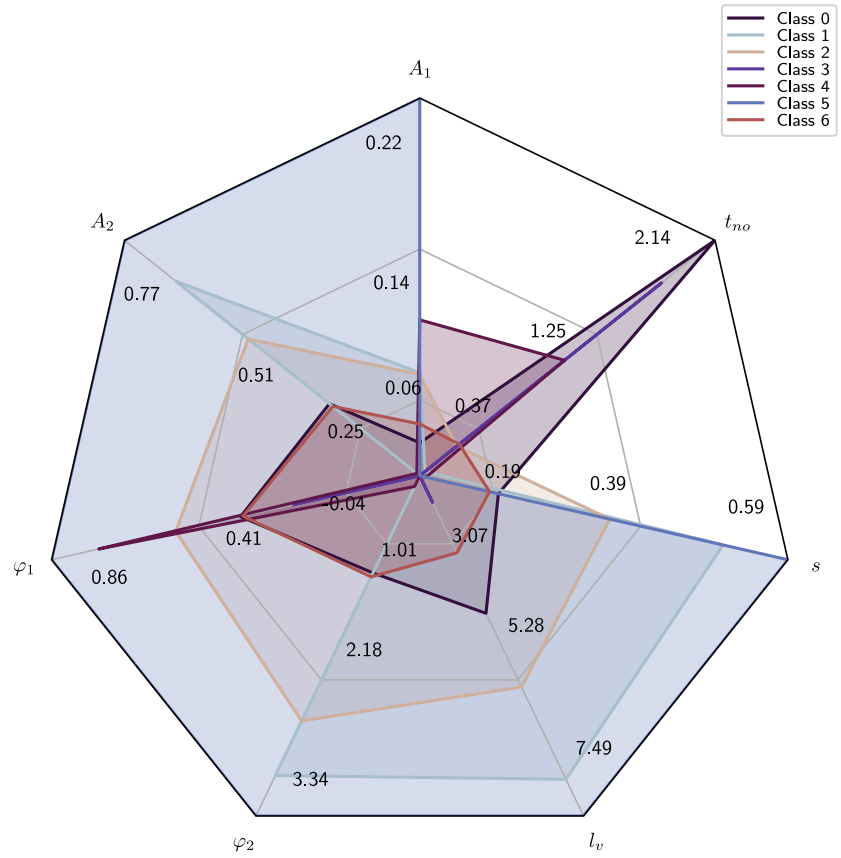

Figure A.4: Visualization of cluster centers for LN_2

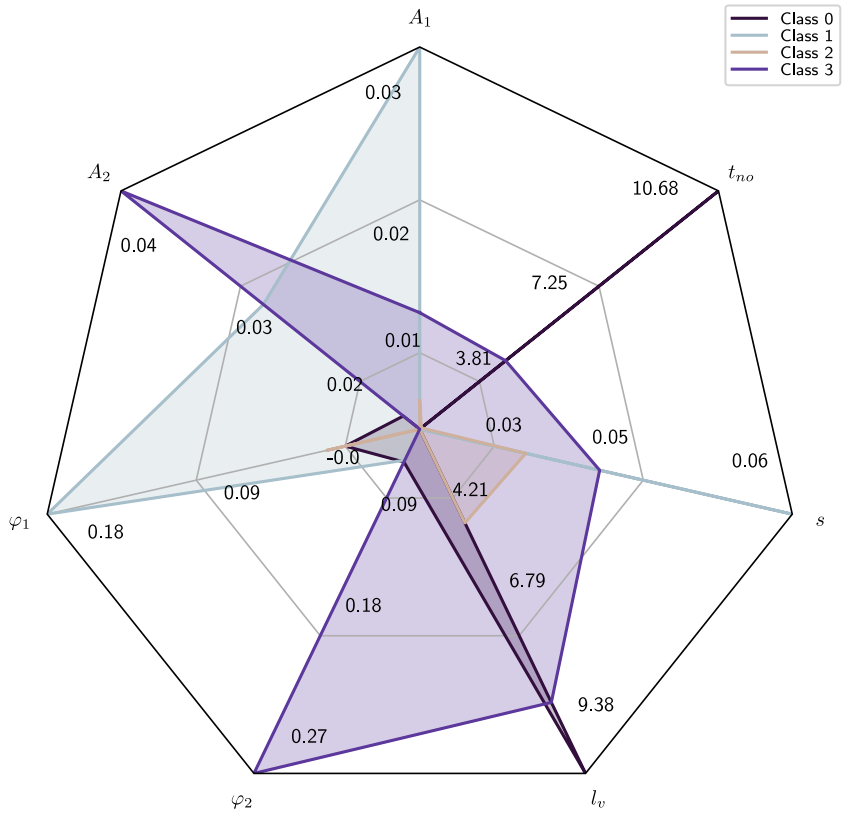

Figure A.5: Visualization of cluster centers for water

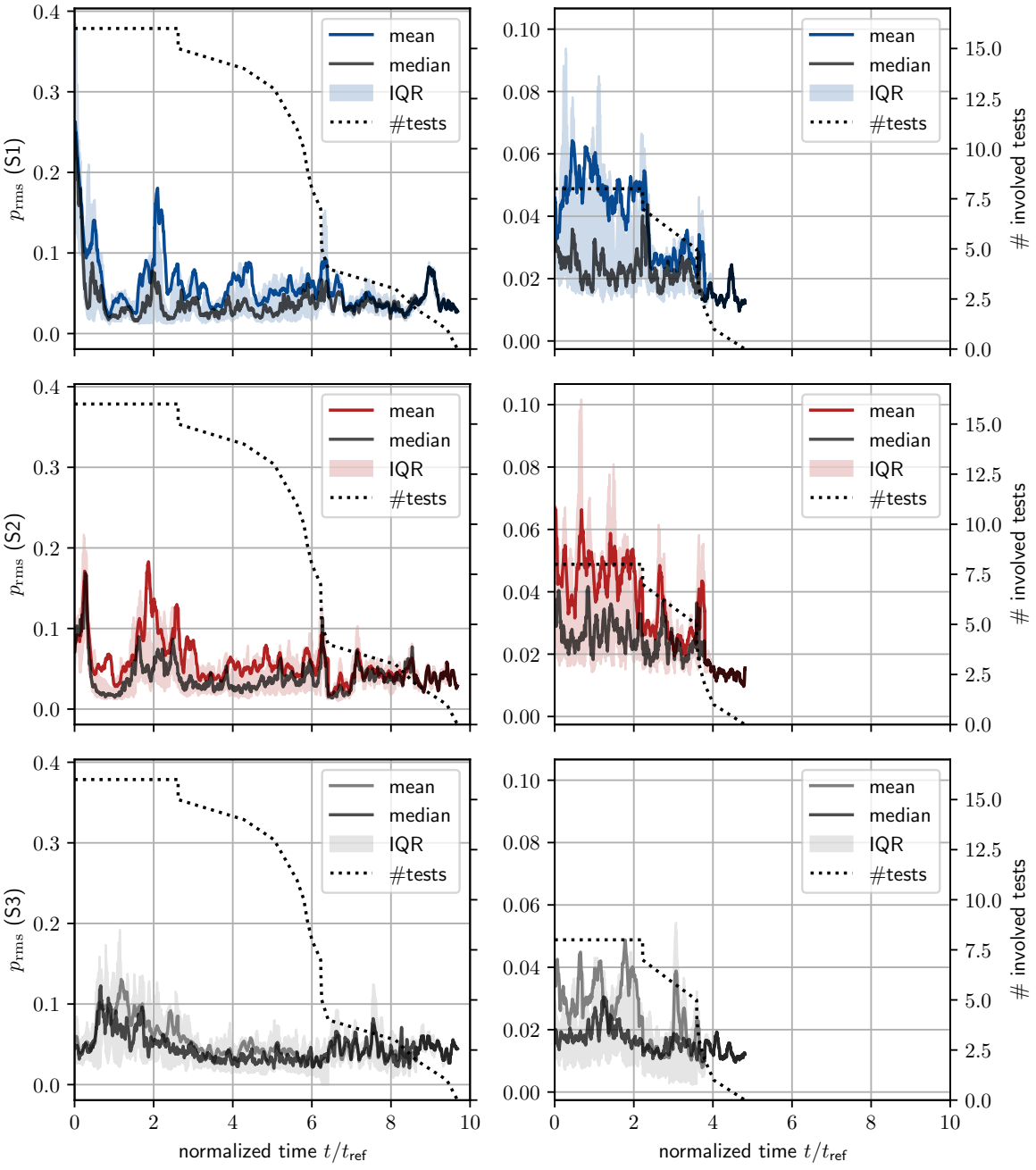

Figure A.6: LN_2, cluster 2: Noise over time for the first (left column) and second (right column) cavitation valley

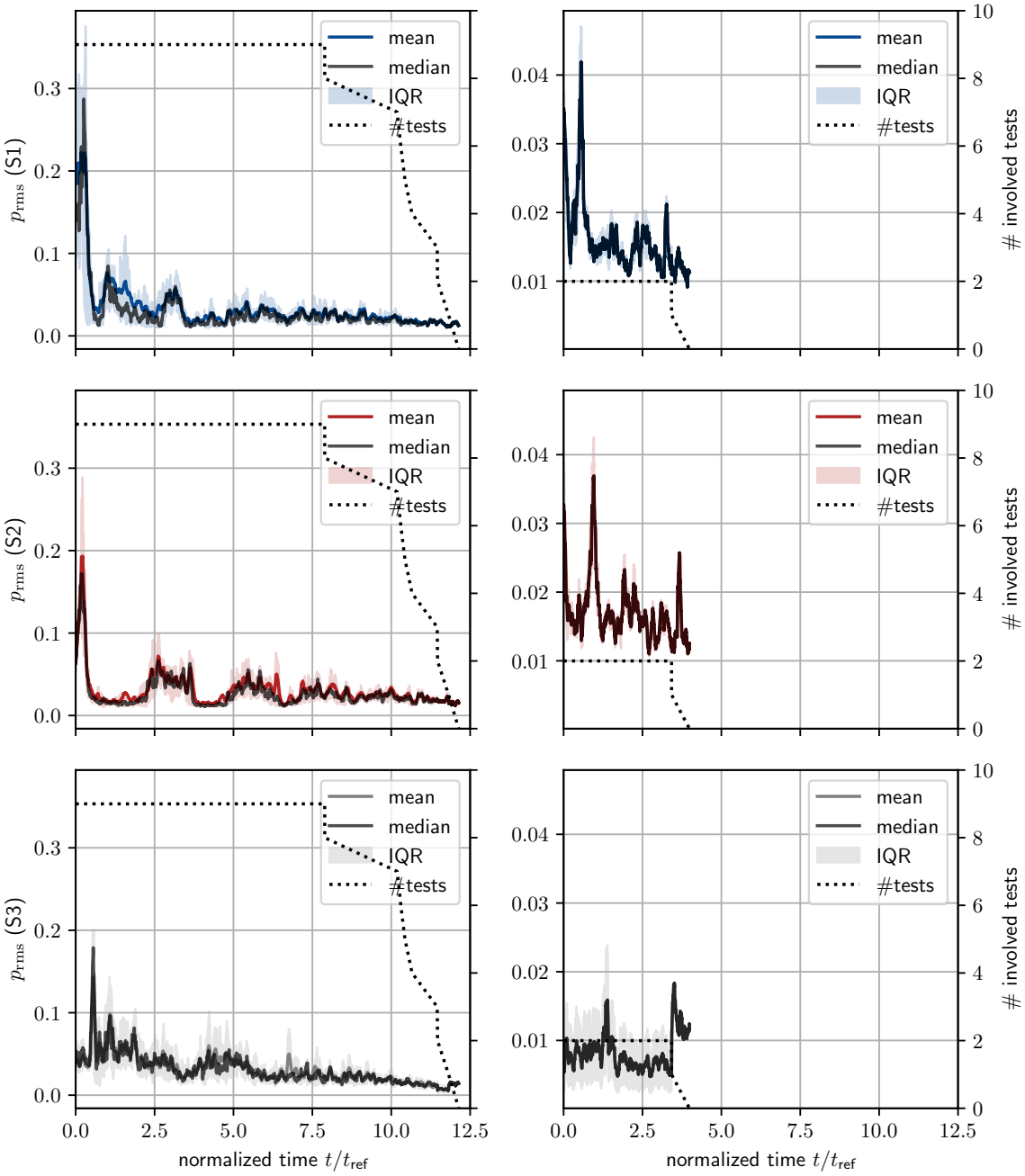

Figure A.7: LN_2, cluster 3: Noise over time for the first (left column) and second (right column) cavitation valley

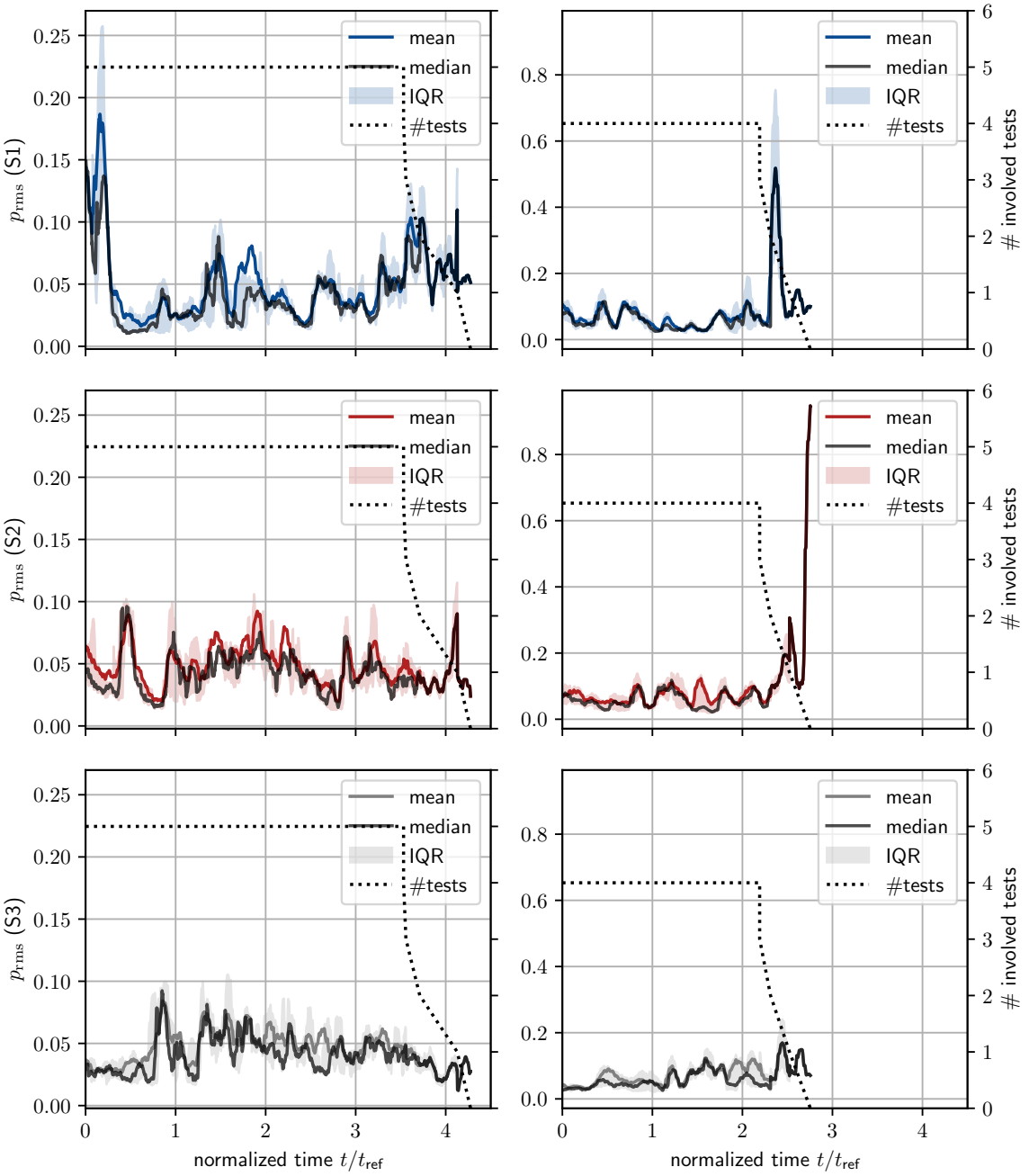

Figure A.8: LN_2, cluster 4: Noise over time for the first (left column) and second (right column) cavitation valley

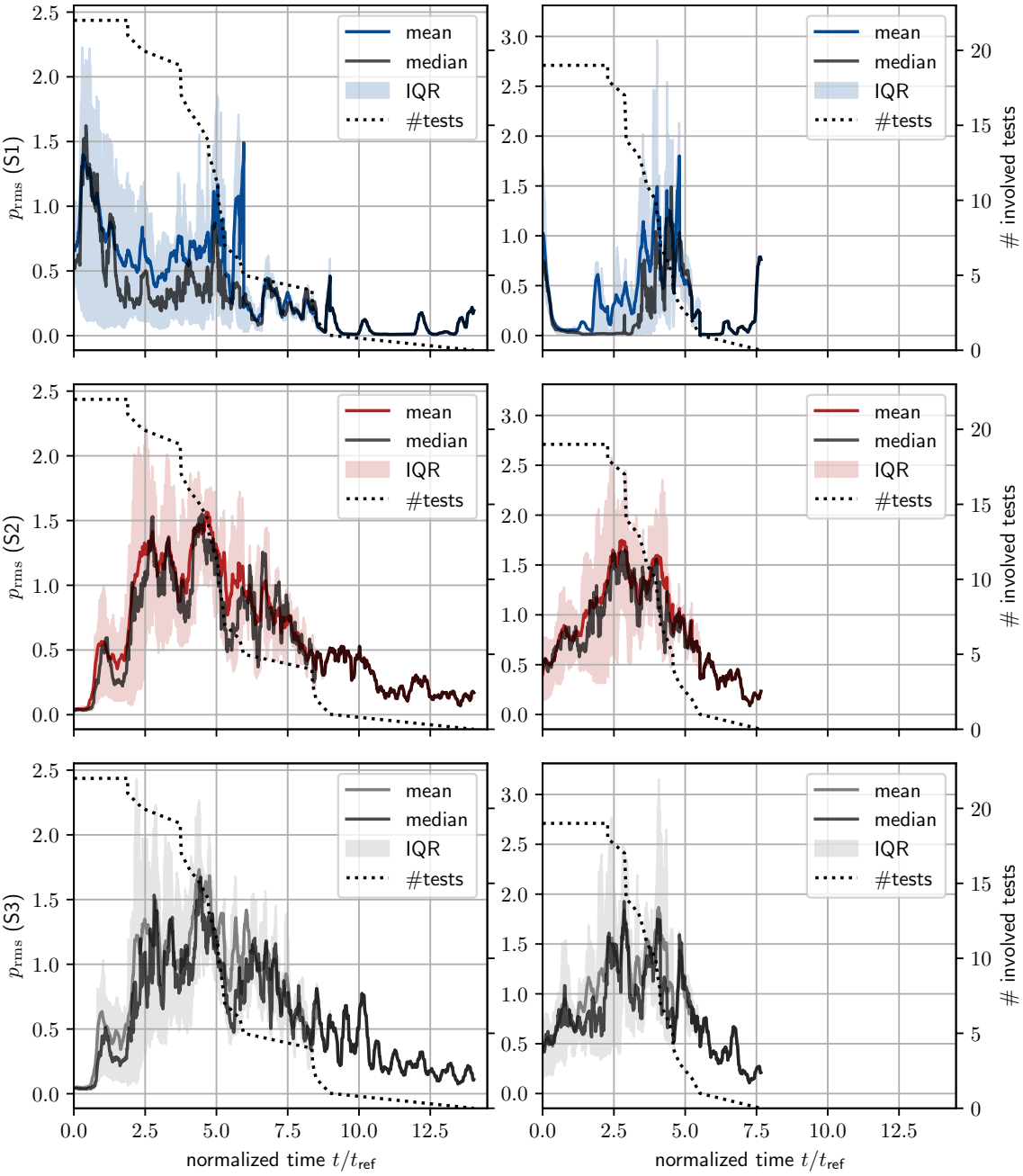

Figure A.9: Water, cluster 2: Noise over time for the first (left column) and second (right column) cavitation valley

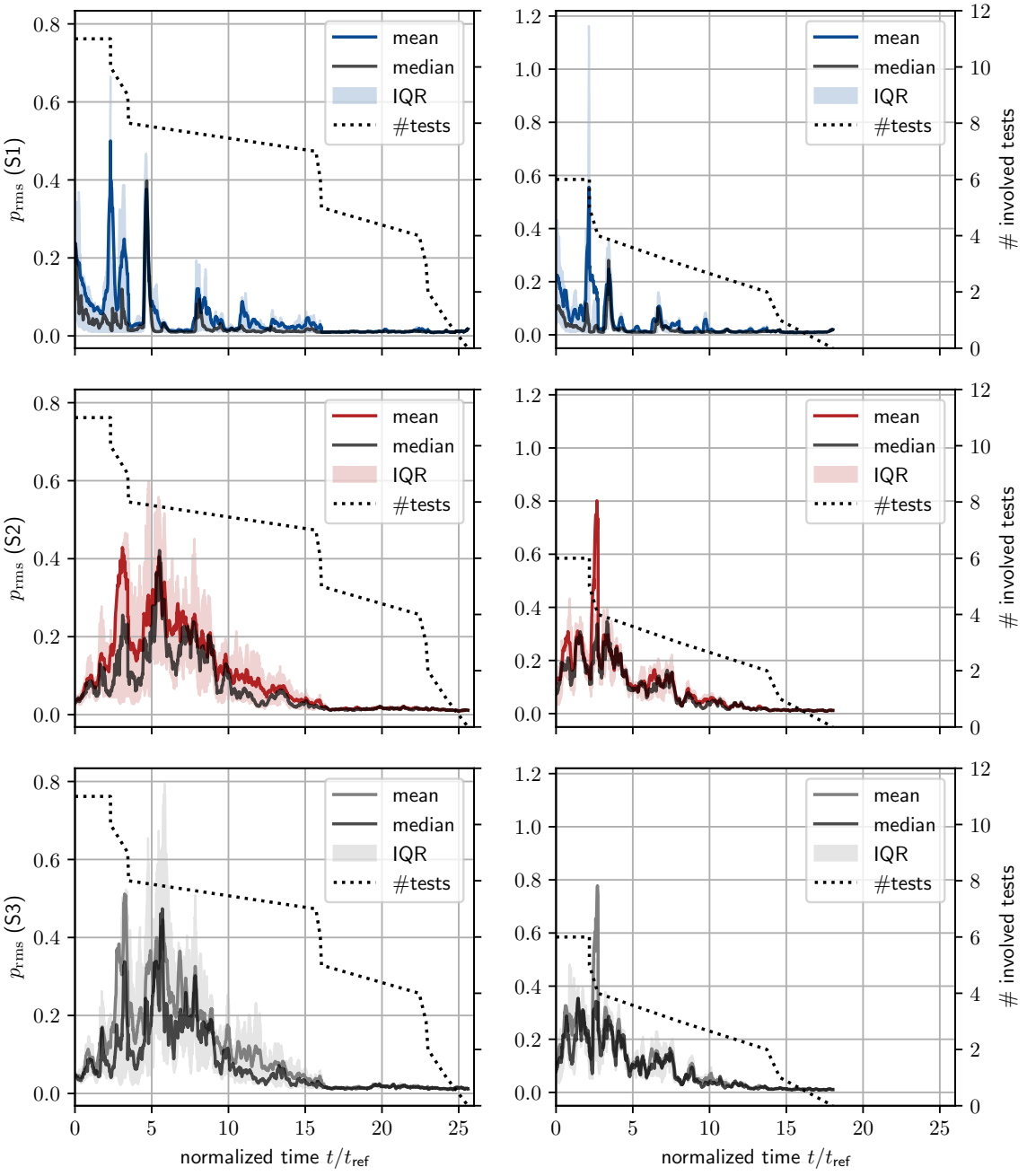

Figure A.10: Water, cluster 3: Noise over time for the first (left column) and second (right column) cavitation valley

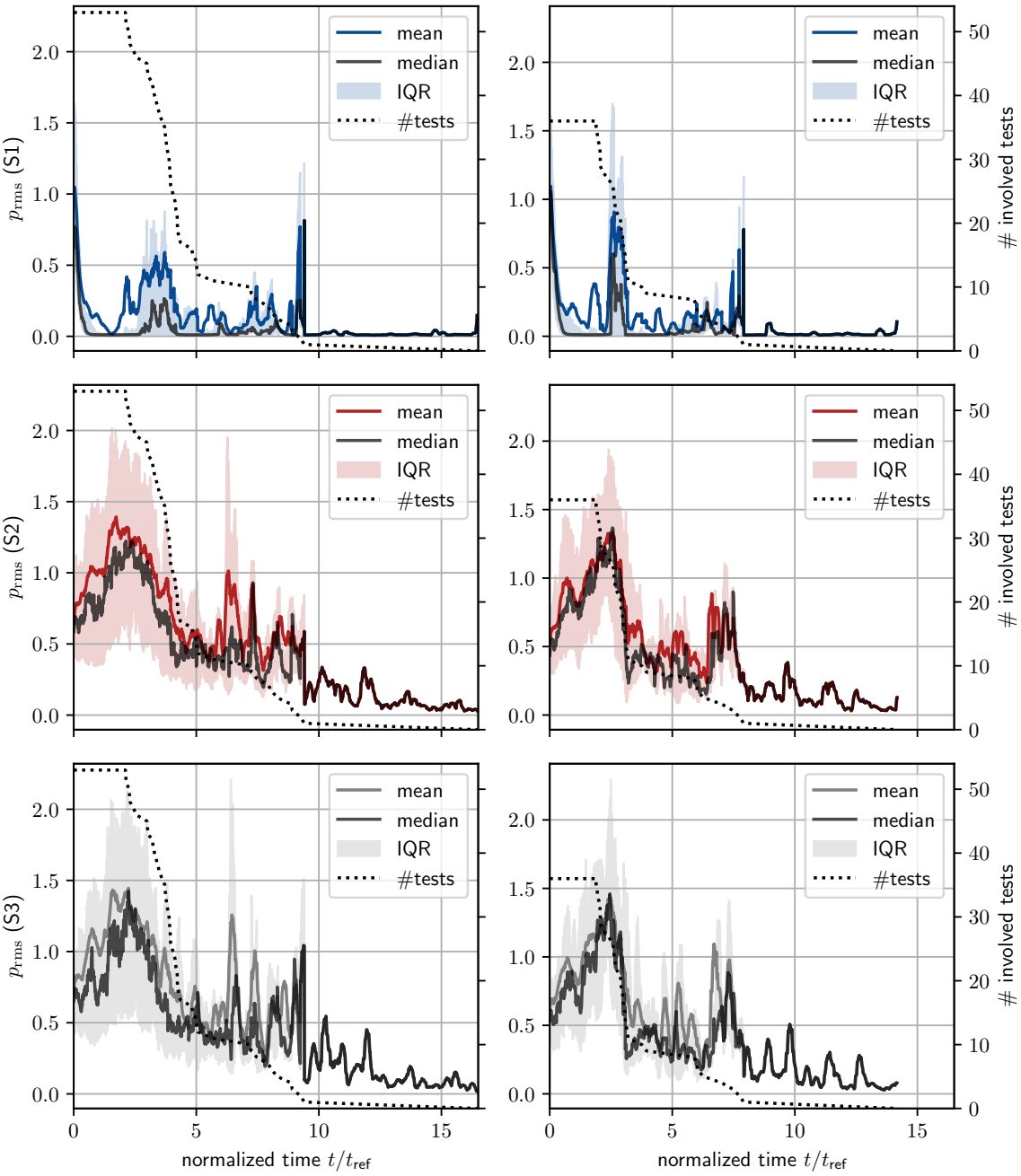

Figure A.11: Water, cluster 0: Noise over time for the third (left column) and fourth (right column) cavitation valley

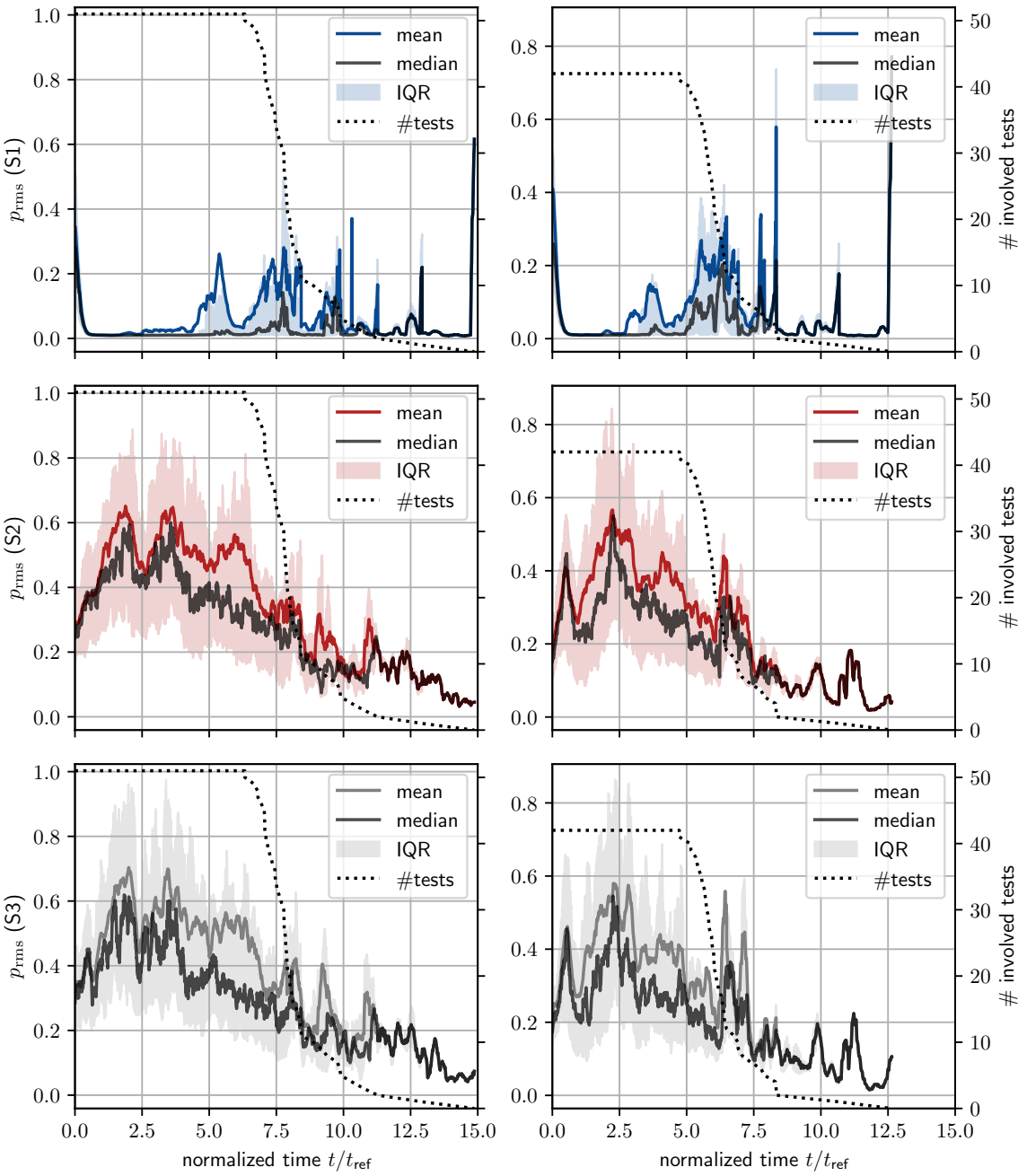

Figure A.12: Water, cluster 1: Noise over time for the third (left column) and fourth (right column) cavitation valley

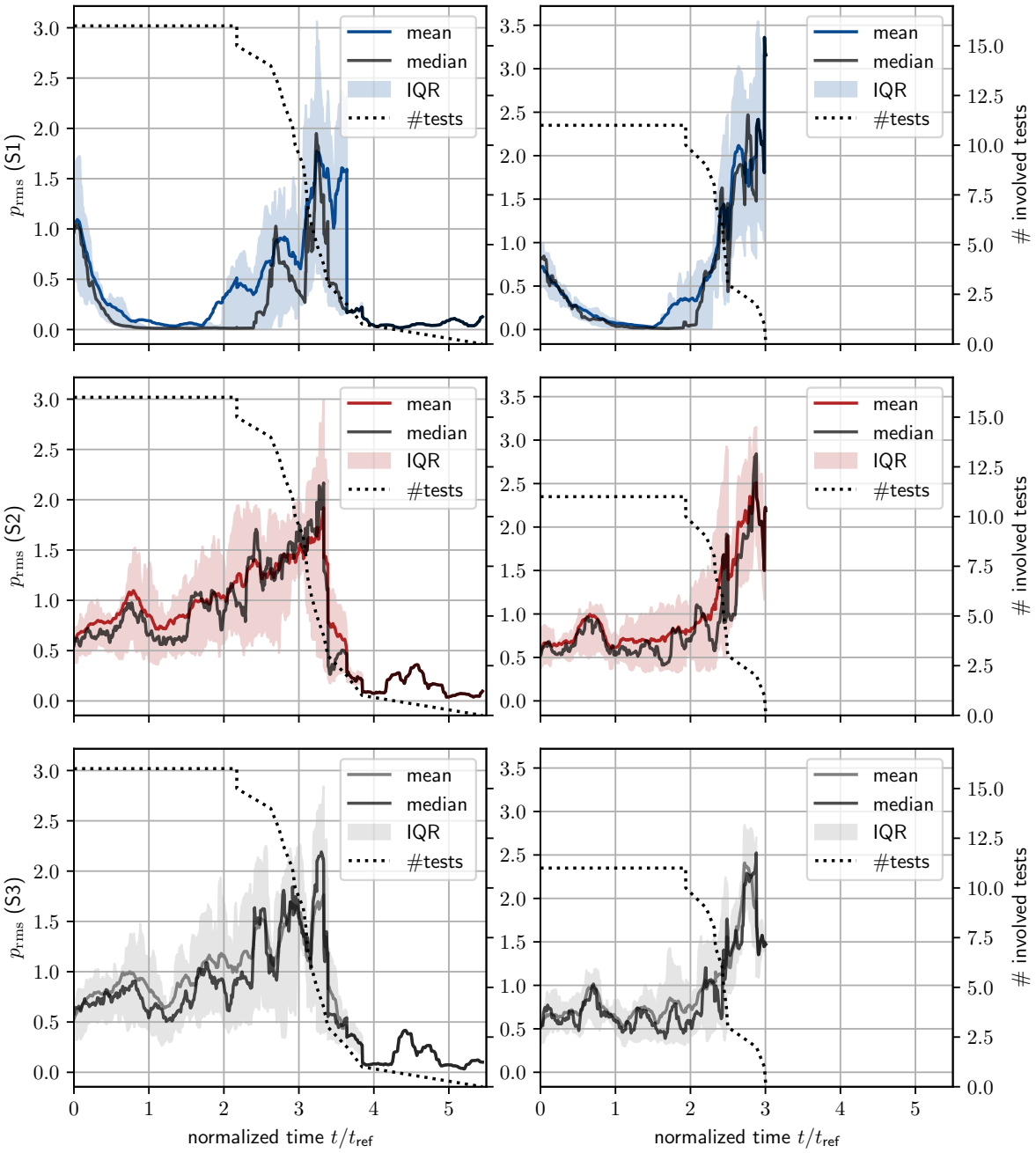

Figure A.13: Water, cluster 2: Noise over time for the third (left column) and fourth (right column) cavitation valley

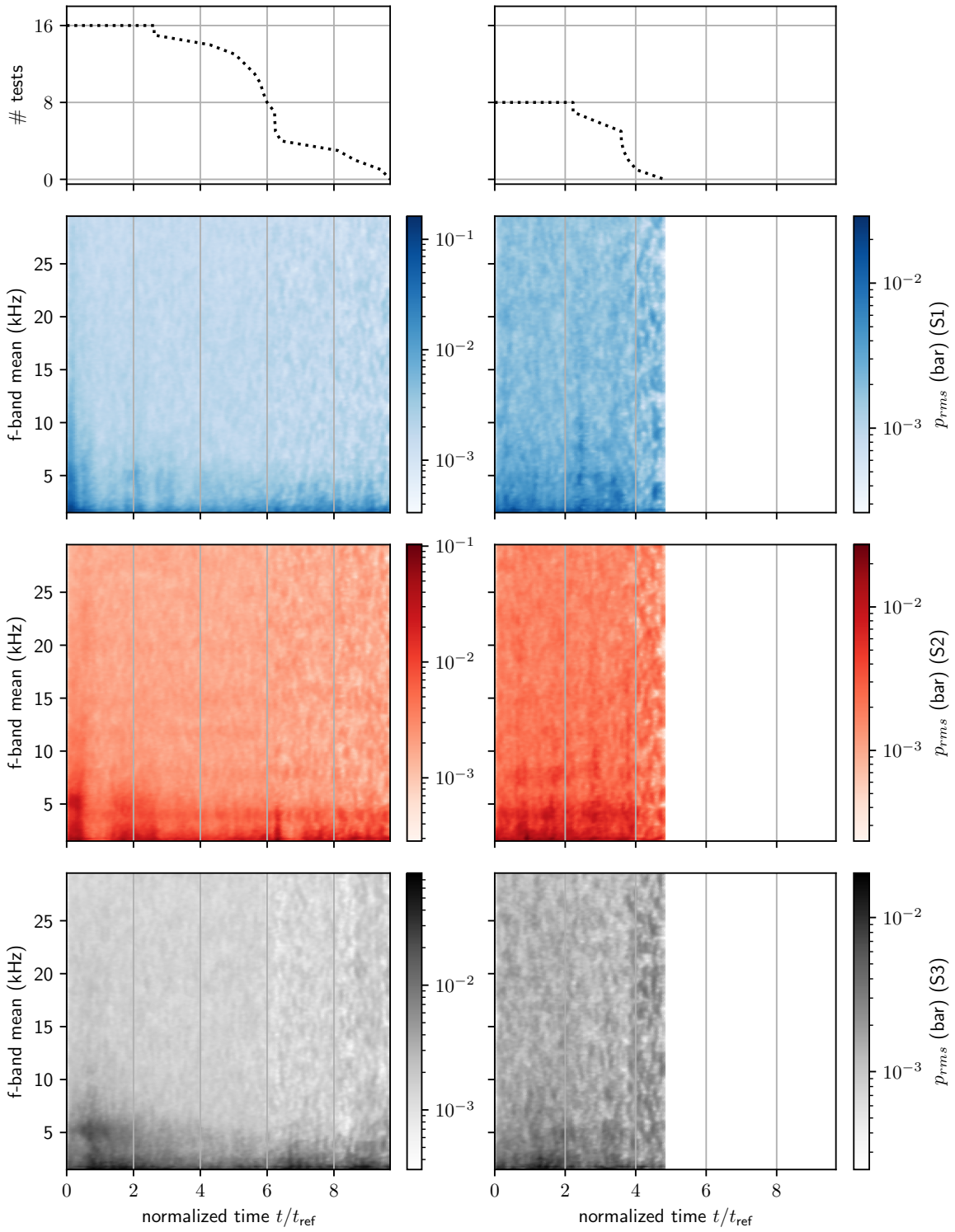

Figure A.14: LN_2, cluster 2: Frequency dependent noise over time for the first (left column) and second (right column) cavitation valley

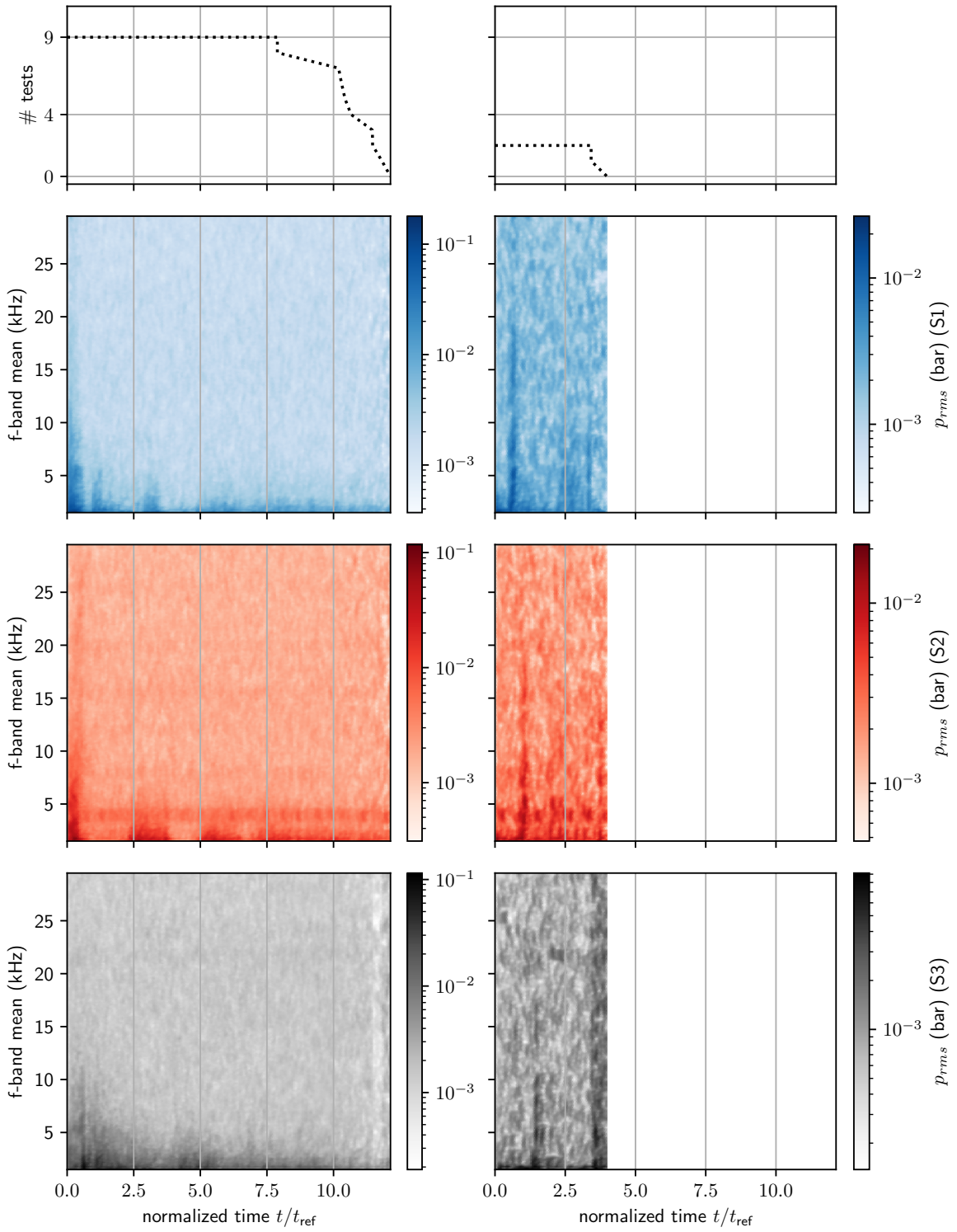

Figure A.15: LN_2, cluster 3: Frequency dependent noise over time for the first (left column) and second (right column) cavitation valley

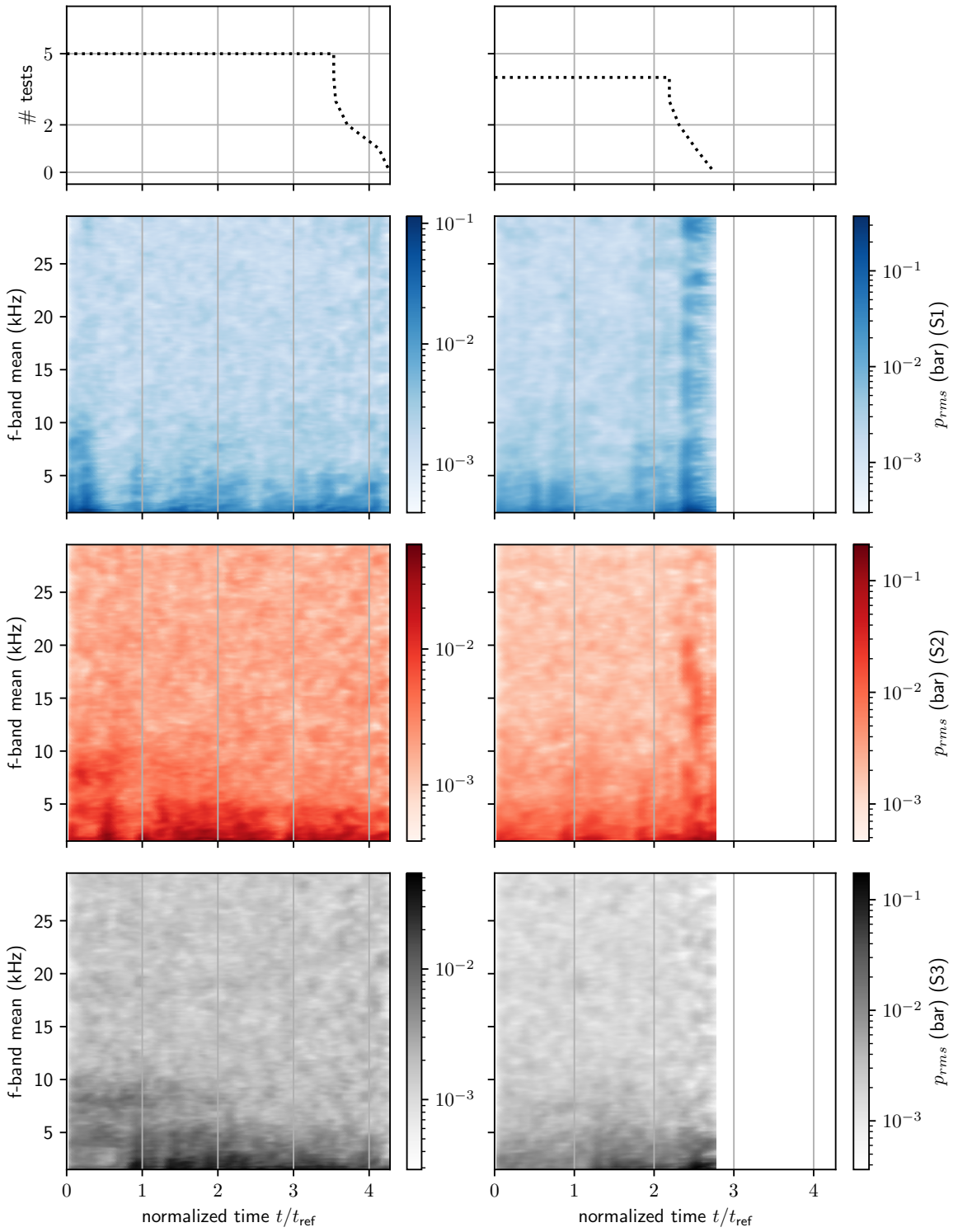

Figure A.16: LN_2, cluster 4: Frequency dependent noise over time for the first (left column) and second (right column) cavitation valley

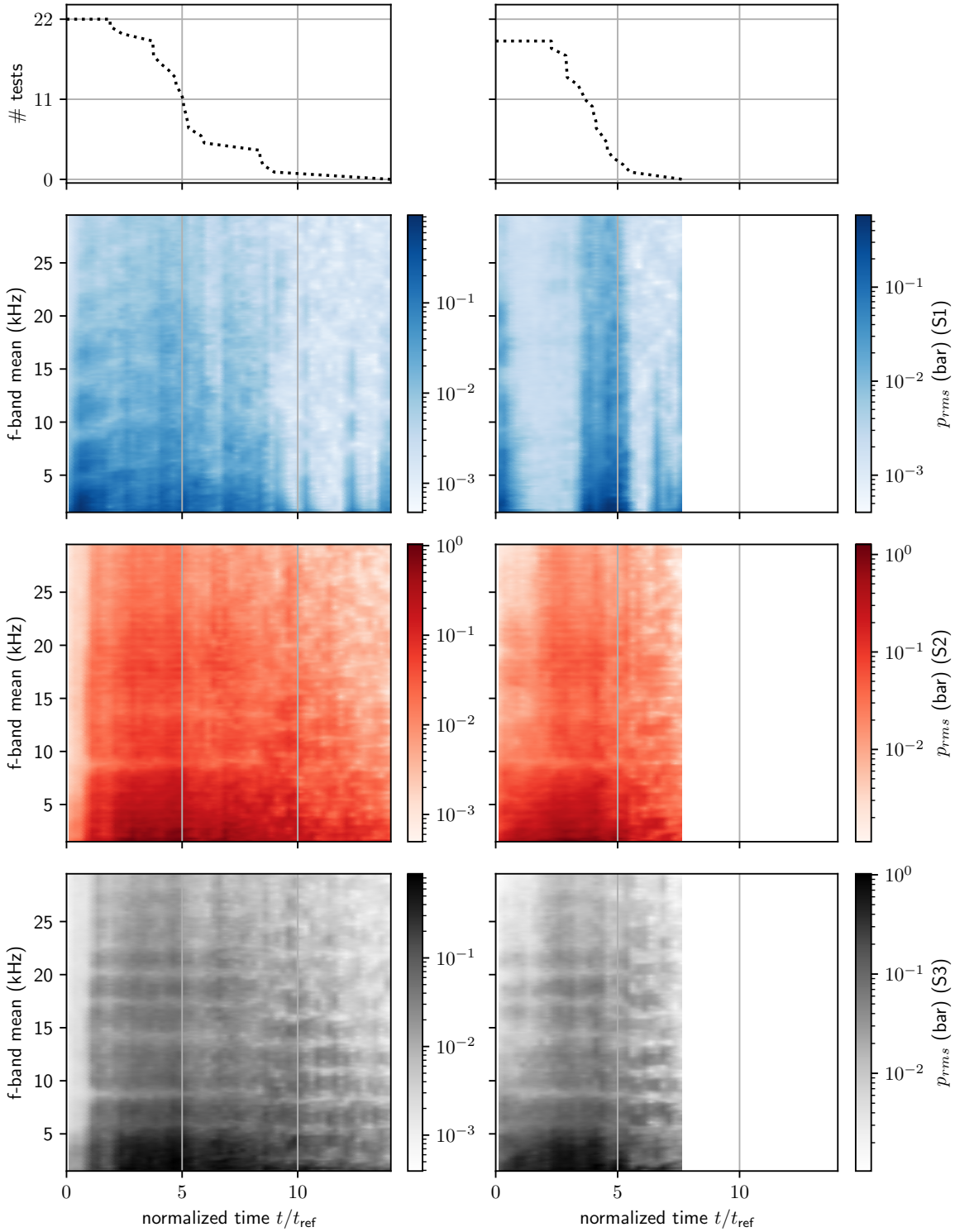

Figure A.17: Water, cluster 2: Frequency dependent noise over time for the first (left column) and second (right column) cavitation valley

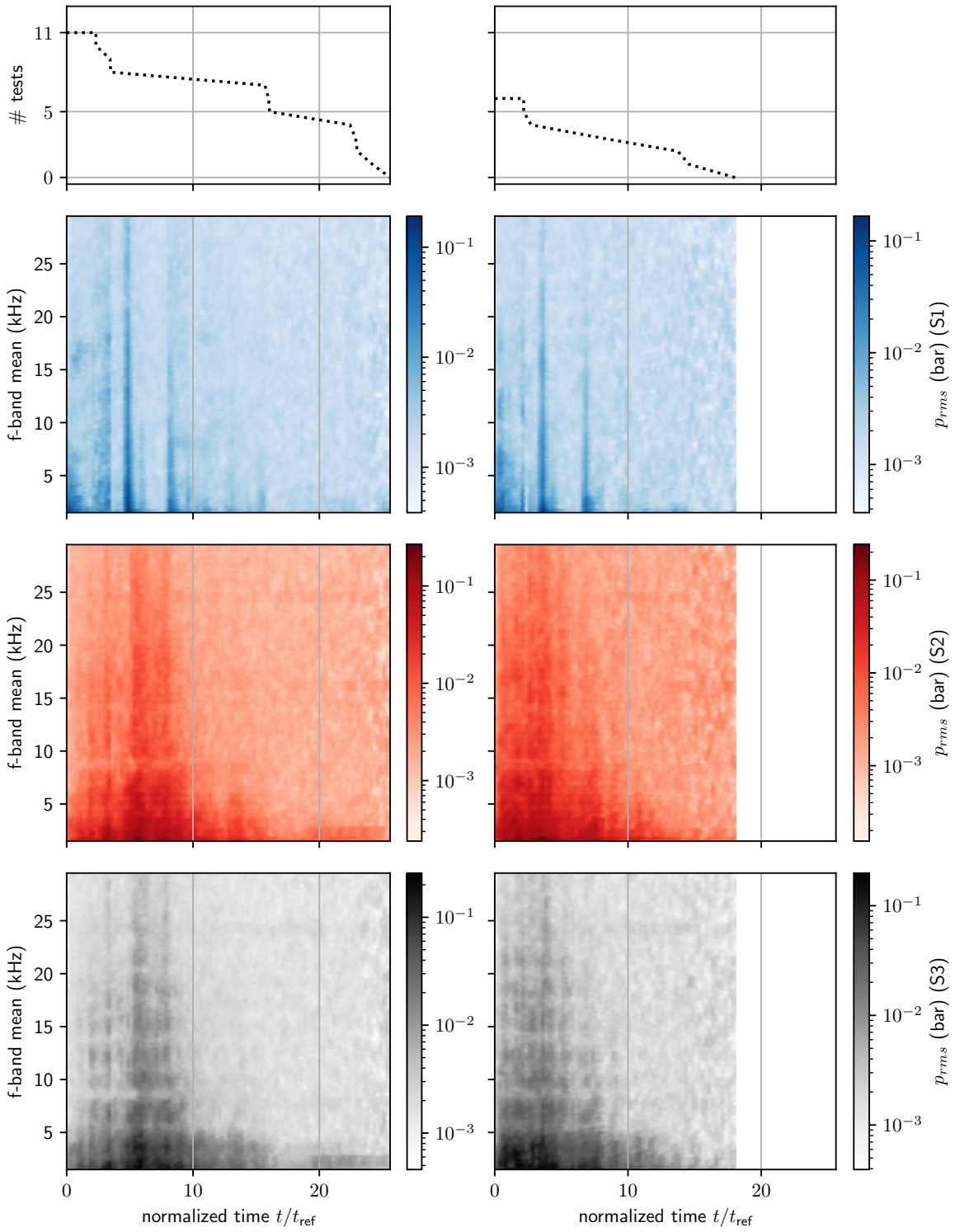

Figure A.18: Water, cluster 3: Frequency dependent noise over time for the first (left column) and second (right column) cavitation valley

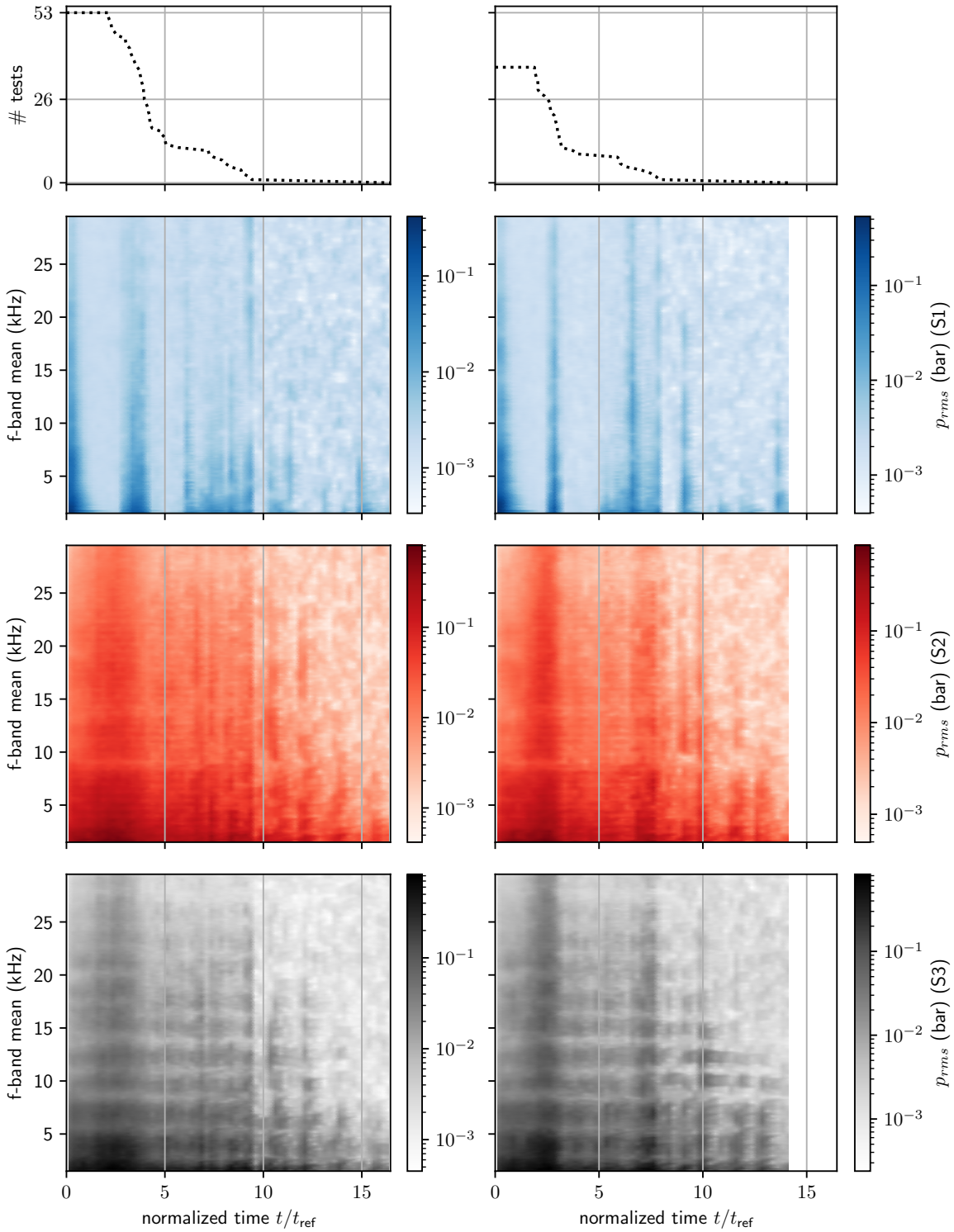

Figure A.19: Water, cluster 0: Frequency dependent noise over time for the third (left column) and fourth (right column) cavitation valley

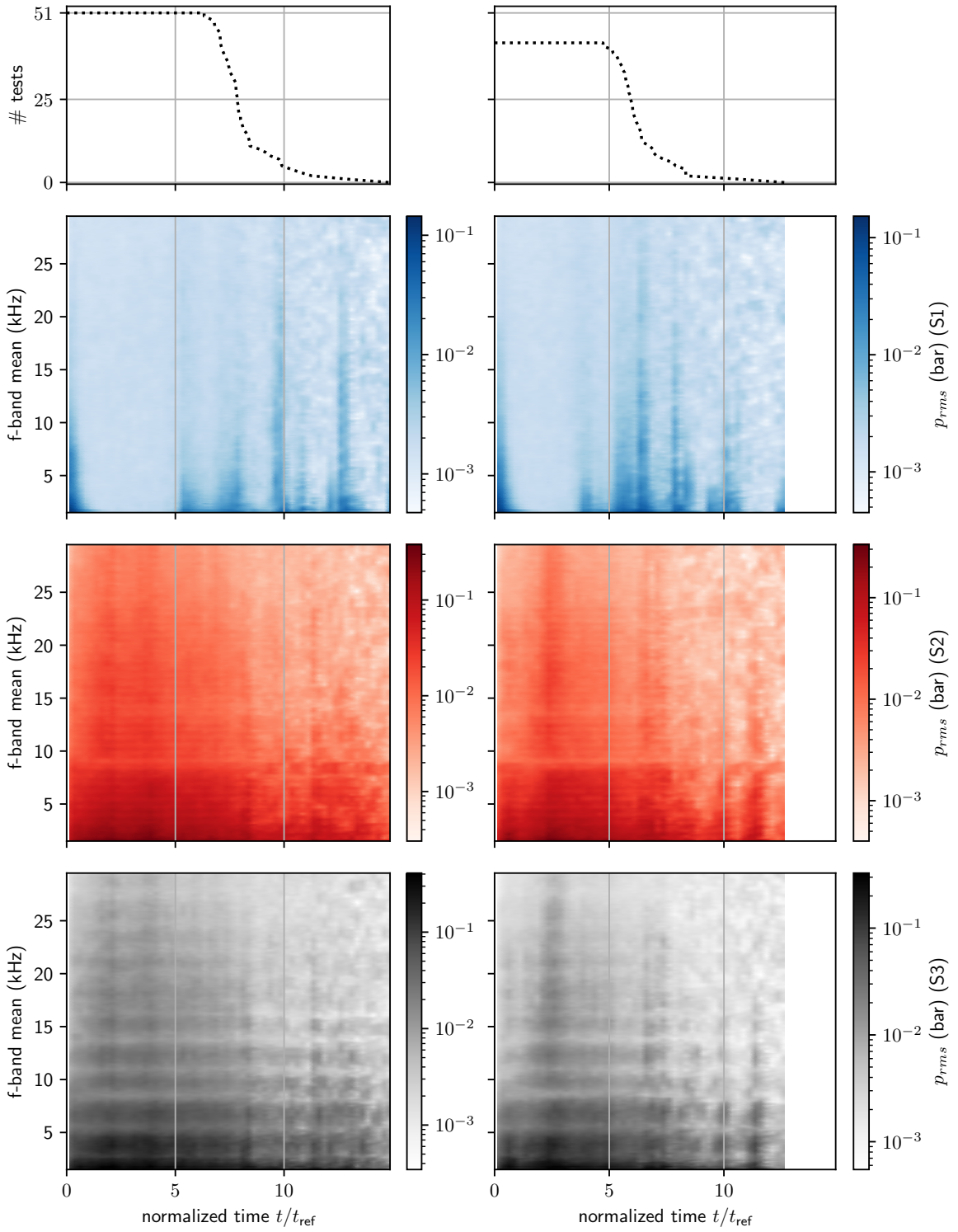

Figure A.20: Water, cluster 1: Frequency dependent noise over time for the third (left column) and fourth (right column) cavitation valley

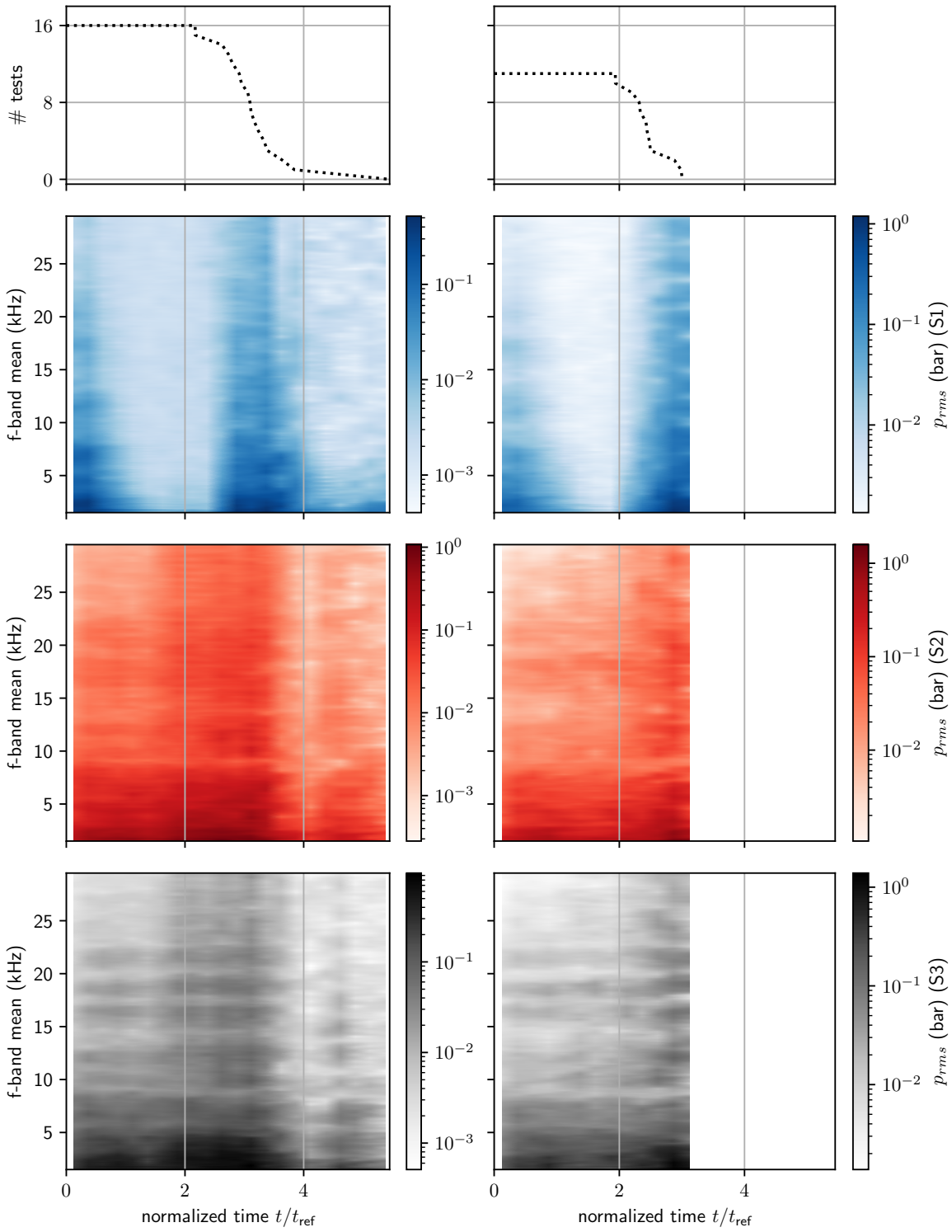

Figure A.21: Water, cluster 2: Frequency dependent noise over time for the third (left column) and fourth (right column) cavitation valley

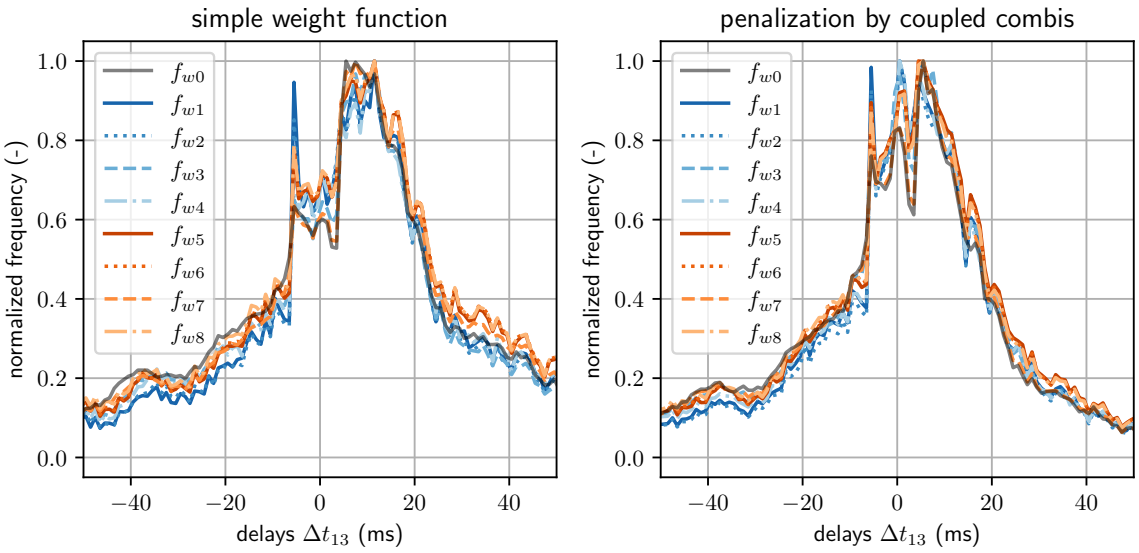

Figure A.22: Sensitivity analysis: weight function (details)

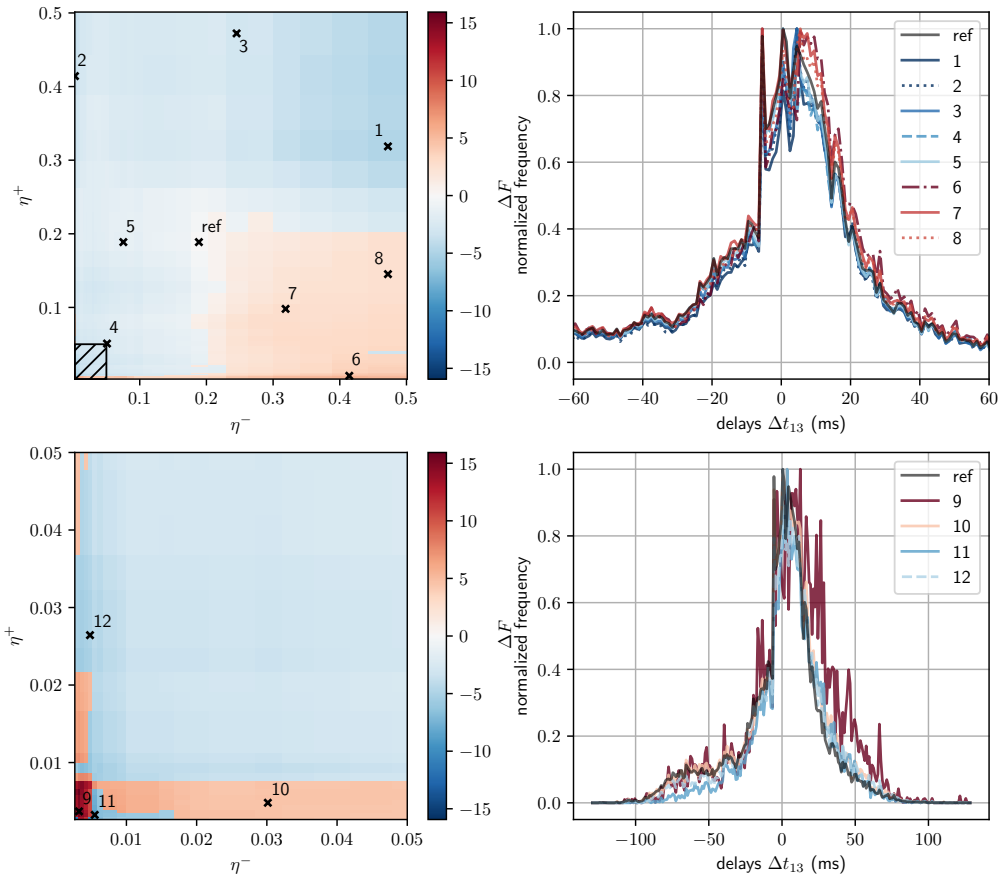

Figure A.23: Sensitivity analysis regarding the speed of sound tolerances η^-, η^+ with focus on small tolerances

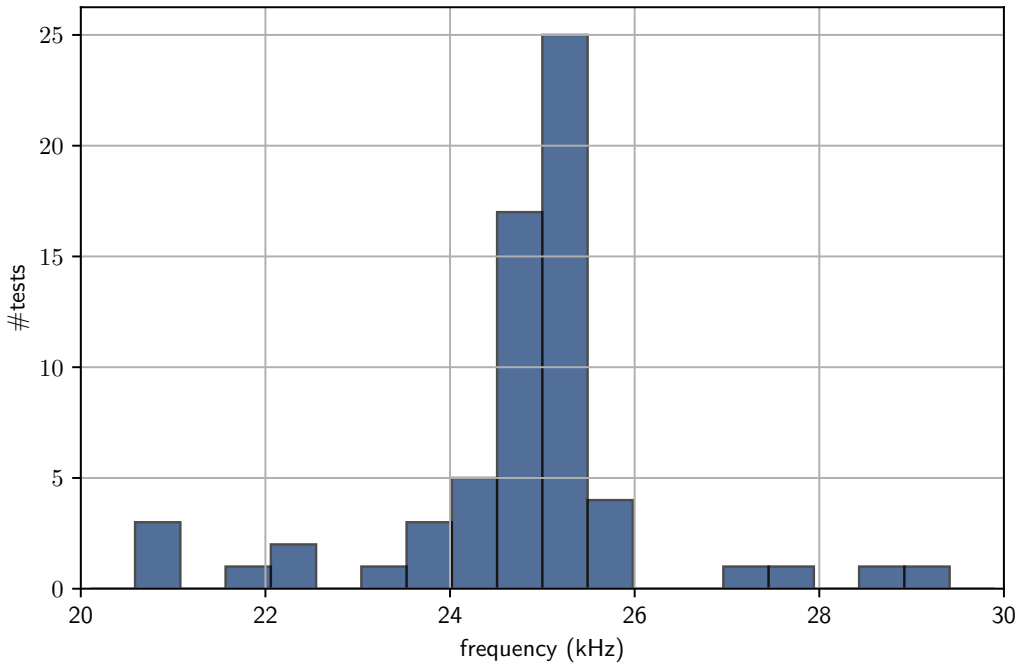

Figure A.24: Distribution of frequency with maximum power within range 20-30 kHz

A.2 Estimation of wave steepening in LN_2

In this thesis, wave steepening was observed in liquid nitrogen. A rough estimation of the influence of the pressure on the speed of sound shall help to assess whether this steepening can be the explained by the compressibility of the liquid nitrogen alone.

Exemplary, representative values are based on the rising edge of the first pressure wave shown in Fig. 5.23. A pressure rise of $\Delta p = 12$ bar is considered. The conditions before the pressure rise are assumed as $T_0 = 75$ K and $p_0 = 0.76$ bar. An adiabatic compression is assumed, leading to a temperature increase of

$$\Delta T = \frac{T_0 \cdot \alpha_0}{\rho_0 \cdot c_{p_0}} \cdot \Delta p \tag{A.1}$$

with the thermal expansion coefficient α_0, the density ρ_0 and the specific heat capacity c_{p_0}. This was derived for example in [1].

In this case, this leads to a temperature T_1 after the pressure rise of approximately 75.3 K. Since now all required conditions (T_0, T_1, p_0, p_1) are known, the speed of sound can be determined at both states. The results are

$$a_0 = 875.28 \text{ m/s}, \tag{A.2}$$

$$a_1 = 881.91 \text{ m/s}. \tag{A.3}$$

Over a length of $\Delta x_{12} = 3.79$ m, this leads to a difference in travel time of approximately 0.03 ms. Given that the rise time of the rising edge of the pressure wave is in the order of magnitude of 4 ms, it appears unlikely that the compressibility of the LN_2 alone causes the steep rising edge observed in S1.

References

[1] K. Knoerzer, R. Buckow, P. Sanguansri, and C. Versteeg. “Adiabatic compression heating coefficients for high-pressure processing of water, propylene-glycol and mixtures – A combined experimental and numerical approach”. In: *Journal of Food Engineering* 96.2 (2010), pp. 229–238.